UNIVERSITY OF CALIFORNIA

Santa Barbara

Transport and Reaction Mechanisms of Dynamic Coatings in Microfluidic Systems

A dissertation submitted in partial satisfaction of the

requirements for the degree Doctor of Philosophy

in Chemistry

by

Austin S. Abrams

Committee in charge:

Professor Sumita Pennathur, Co-Chair

Professor Kevin W. Plaxco, Co-Chair

Dr. David E. Huber

Professor Lior Sepunaru

Professor Mattanjah S. de Vries

December 2022

The dissertation of Austin S. Abrams is approved.

_____

Mattanjah De Vries

_____

Lior Sepunaru

_____

David E. Huber

_____

Kevin W. Plaxco, Co-Chair

_____

Sumita Pennathur, Co-Chair

December 2022

ACKNOWLEDGEMENTS

I acknowledge this dissertation to my grandfather, who passed away one year ago. Since I was eight, I remember your inspiring words to pursue my passions, in school and my other hobbies (piano, saxophone, and swimming). Each time I saw you, you gave me in an enormous bear-hug and asked me about one hundred questions. I am incredibly lucky to have had your support from elementary school through college as I received an amazing liberal arts education; I was surrounded by brilliant teachers and friends, who helped me develop my passions in chemistry and computer science. Even when your memory started to leave you, I remember you had the biggest grin and excited look at my college graduation. Your spirit, full of enthusiasm and determination, is what lives in me today. While you are no longer here, I imagine you sitting at my final defense, listening with curiosity and awe.

I thank my family, without whom my endeavors to finish my PhD would not have been possible. Thank you, Mom, and Dad. You have always supported me and helped me through difficult times during my PhD. While a middle child has its disadvantages, I thank Dani and Ben for their love and motivation as we each pursued our dream careers. I also want to thank Monica for being by my side every day and bringing me such tremendous joy.

Much of what I learned stems from my incredible mentors and peers. Thank you, Sumita, for believing in me and allowing me to pursue my own research interests. Thank you, Dave, for always listening to me and helping me become a better scientist. Thank you, Lingyun, Xavier, Sean, and Alex, for being amazing lab mates and helping me with experiments and many other challenges. Thank you, Bennett, Ian, and Lexi, for devoting your time to become incredible research assistants – some of this work would not have been possible without you.

VITA OF AUSTIN S. ABRAMS
December 2022

EDUCATION

Bachelor of Arts in Chemistry, Pomona College, Claremont, May 2016
Doctor of Philosophy in Chemistry, University of California, Santa Barbara, December 2022

PROFESSIONAL EMPLOYMENT

June–August 2014: Research Intern, Hawker Group, University of California, Santa Barbara

June–August 2015: Research Intern, Meijer Group, University of Technology, Eindhoven

September 2015–April 2016: Thesis Researcher, Van Ryswyk Group, Harvey Mudd College

September 2016–December 2017: Rotating Graduate Researcher, Hawker Group, Read de Alaniz Group, and Bates Group, University of California, Santa Barbara

September 2017–June 2022: Teaching Assistant, Departments of Chemistry, Mechanical Engineering, and Physics, University of California, Santa Barbara

January 2018–December 2022: Graduate Researcher, Pennathur Group, University of California, Santa Barbara

December 2022–Present: Scientist I, Mekonos Incorporated, Berkeley, California

PUBLICATIONS

"Transport and Reaction Mechanisms of Surface Coatings in Microfluidic Systems," Unpublished thesis submitted in partial fulfillment of the requirements for the Doctor of Philosophy degree in Chemistry, University of California, Santa Barbara, 2022. [106 pp.]

"A Cautionary Tale: Electrokinetic Transport of a Cationic Surfactant Induces Stagnant Regimes in Capillary Adsorption and Desorption," Submitted article under review, 2022.

"Real-Time Zeta Potential Analysis of Microchannel Surfaces during Aminosilane Deposition and Exposure Using Current Monitoring," *Analytical Chemistry*, 93 (2021), 16512-16519.

CONFERENCE PROCEEDINGS

"Improving the Coverage and Stability of Microchannel Surface Coatings Using Automated Zeta Potential Analysis," 25th Conference on Miniaturized Systems for Chemistry and Life Sciences (μTAS), Palm Springs, 2021.

"A Continuous Conductivity-Based Platform for Monitoring Chemical Kinetics in Real-Time," IEEE 4th Conference on Micro and Nanotechnology in Medicine, Kauai, 2018.

"Measuring Changes in Nanofluidic Current as a Continuous Multi-Analyte Biosensor for Biological Fluids," 5th Southern California Micro and Nanofluidics Symposium, Arcadia, 2018.

"Measuring Changes in Nanofluidic Current as a Continuous Multi-Analyte Biosensor for Biological Fluids," 19th UC Systemwide Bioengineering Symposium, Riverside, 2018.

"Light as a Tool to Reversibly Activate Cross-link Exchange in Vitrimers," UCSB Materials Research Outreach Program Symposium, Santa Barbara, 2017.

"Conformal Coating of Colloidal Quantum Dots on Plasmonic Photovoltaics," Pomona College Department of Chemistry Senior Thesis Symposium, Claremont, 2016.

AWARDS

2nd Place, Oral Presentation Award, 5th Annual Southern California Micro and Nanofluidics Symposium, Arcadia, 2018

Top Finalist, National Defense Science & Engineering Graduate Fellowship, 2018

Outstanding Service Award, Department of Chemistry, University of California, Santa Barbara, 2022

Chair's Fellowship, Department of Chemistry, University of California, Santa Barbara, 2022

Summer Support Grant for PhD Students, University of California, Santa Barbara, 2022

FIELDS OF STUDY

Major Field: Kinetics of Silane and Surfactant Coatings in Microfluidic Channels

Studies in Polymer Chemistry with Professors Guillermo Bazan and Craig J. Hawker

Studies in Microfluidic Transport with Professor Sumita Pennathur and Dr. David E. Huber

Studies in Electrochemistry with Professors Lior Sepunaru and Kevin Plaxco

ABSTRACT

Transport and Reaction Mechanisms of Surface Coatings in Microfluidic Systems

by

Austin S. Abrams

Molecules that self-assemble to form thin coatings on surfaces are of great interest to many industries (e.g., biomedical, marine, and solar) for imparting hydrophobic, conductive, and/or anti-fouling properties. For example, in capillary electrophoresis (CE), inner surfaces of a capillary are coated to control electroosmotic flow (EOF), prevent adsorption, and increase solubility of proteins; this coating reverses the direction of EOF relative to electrophoresis (EP), thereby enhancing separation efficiency and resolution. The rapid degradation of these coatings, however, causes band broadening and variable migration times as the desorbing species changes the EOF velocity and interferes with the detector. Unfortunately, studies to understand desorption in these conditions show different kinetic behaviors and employ low-resolution analysis techniques. Therefore, techniques with greater temporal resolution and control of solution and transport properties are needed to elucidate degradation mechanisms in CE and other applications.

This work presents a high frequency, *in situ* platform for extracting surface charge (*i.e.,* zeta potential) within a silica microcapillary during surface coating or degradation. A continuous platform was adapted from the current monitoring method, which extracts EOF

velocity by measuring the time for fluid to traverse a channel of known length in an electric field; the traversal endpoint is measuring by a linear change in current and subsequent steady state as a solution of different conductivity fills the channel. Zeta potential is calculated using the Helmholtz–Smoluchowski equation and the EOF velocity. Automated zeta potential analysis (AZA) detects the traversal endpoint using the first-derivative, then alternates the electric field polarity for consecutive measurements.

This novel automated approach for monitoring zeta potential was first applied to study aminosilane coating formation and stability for different monomer types and solution conditions. The density of cationic coatings was inferred by an increase in zeta potential relative to the bare surface value; coating stability was monitored by the relative decay in zeta potential after exposure to conditions without the monomer. First, applying AZA to study aminosilanes, we observed higher densities for trimethoxy vs. monomethoxy silanes and faster coating kinetics for trimethoxy vs. triethoxy silanes. Upon exposure, we observed faster decay for higher-pH solutions and shorter-alkyl-length monomers. Coatings deposited in aqueous vs. anhydrous conditions exhibited a lower density and greater stability, indicating that aqueous conditions promote more lateral crosslinking.

We also applied AZA to study adsorption and desorption of CTAB, a cationic surfactant, in conditions relevant to CE (e.g., capillary diameter, EOF/EP, and pressure). In contrast to previous studies, our kinetics were multiphasic with an intermediate "stagnant regime" at distinct zeta potentials in adsorption or desorption. These stagnant regimes occurred at positive zeta potentials where the EOF was equal and opposite to EP, inducing a near-zero net transport of CTA^+ (EP+EOF). The kinetics depended strongly on the capillary surface-area-to-volume ratio and the EP mobility of CTA^+, which changed with concentration. We

confirmed these trends by recasting the zeta potential kinetics in terms of net CTA^+ transport volume divided by surface area; this normalization collapsed and linearized the responses for a range of diameters. We showed that varying the voltage algorithm and applying pressure could prolong or eliminate the stagnant regime; new AZA algorithms were developed to further control the transport-limited kinetics by maintaining a fixed net transport of CTA^+. With higher resolution and control of transport during coating formation and degradation, this versatile platform enables the discovery of optimal coating chemistries for an array of applications.

TABLE OF CONTENTS

Introduction

The Importance of Surface Modification

The complex chemistry that exists at solid–liquid interfaces is a challenging topic to understand yet plays a critical role across many industries. Advantageous properties of surfaces are commonly realized through modifications which impart chemical functionalities at the surface, such as increased hydrophobicity or tuned interactions with molecules in the bordering solution. For instance, controlling the hydrophobicity of a biosensor surface allows for the desirable attraction of analytes while preventing adsorption of other molecules that interfere with detection.[1] The use of thin films or coatings on metal surfaces (e.g., marine equipment, airplanes, plumbing) can prevent corrosion and improve hydrodynamic or aerodynamic properties.

Surface coatings are not only common to many commercial industries but are also important to innovative research in solar energy, electronics, biomedicine, and bioanalysis. For instance, the selective deposition of covalent-bonding monomers (e.g., silanes, thiols) onto patterned substrates allows for rapid, spin-on deposition of polymers; this specific behavior may be applied to develop nanometer-sized transistors on computer chips with greater speed and precision.[2] Dynamic coatings (e.g., ligands, surfactants) are used to stabilize nanoparticles and quantum dots by preventing the aggregation of these particles; this stability is critical to applications in solar cells[3] and targeted therapeutics[4].

Studies to understand the mechanisms of surface reactions allow surfaces to be used in a variety of applications, such as the analysis of biological molecules (e.g., DNA, proteins).[5–7] As surfaces are readily engineered into optimal geometries for the detection and analysis of

biological analytes, the rates of surface reaction and/or molecular transport in solution are critical information used in the development of robust and versatile bioanalytical platforms.

Surface Modification in Capillary Electrophoresis

Capillary electrophoresis (CE), a prevalent method for analyzing proteins and sequencing DNA, relies on the chemical charge within a glass capillary. Control of this charge has allowed for the sequencing of whole genomes and complex analyses of protein mixtures.[8,9] In protein separations, a sample is injected at one end of the capillary and separated along the capillary length in the presence of an electric field; then, individual proteins are analyzed by a light or mass detector at the opposite end of the capillary (Figure 1). The migration of proteins and DNA in this condition stems from two primary mechanisms of transport: 1) the electrophoretic (EP) movement based on the net charge of individual molecules,[10] and 2) the electroosmotic flow (EOF) of fluid according to the net charge on the capillary surface.[11] Thus, proteins with similar EP mobilities may be better separated by modification of the surface's charge, which changes the direction and magnitude of EOF.

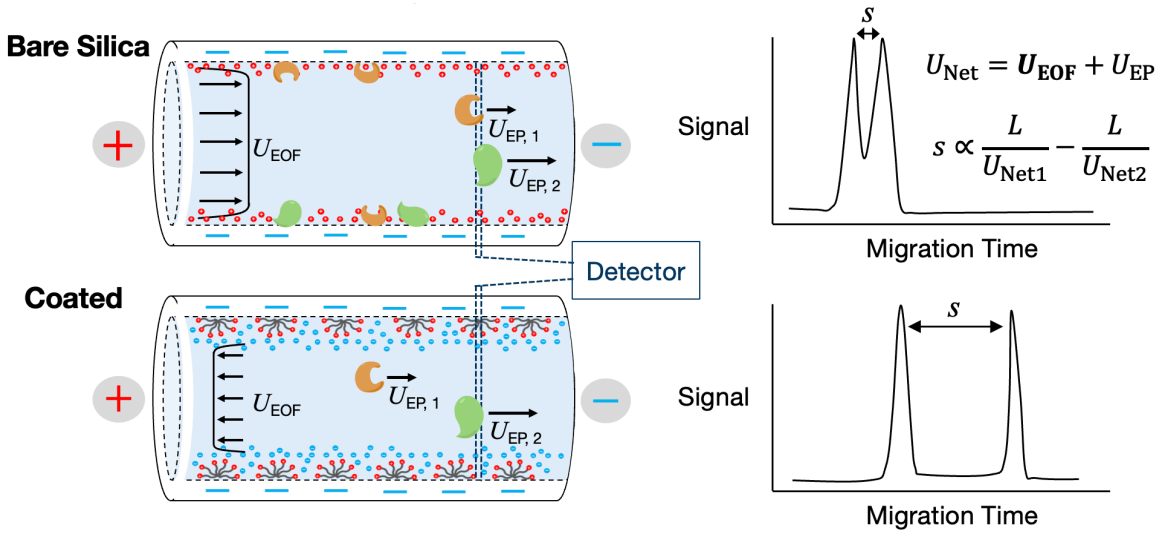

Figure 1. Peak resolution and separation efficiency of bare and cationic-coated silica capillaries in CE. The separation of two proteins depends roughly on the difference in net velocities, or the sum of the electrophoretic and electroosmotic velocities.

The separation of basic proteins using CE is commonly enhanced by modifying the capillary surface with a cationic coating that reverses the direction of EOF (Figure 1). Reversal of EOF often results in a lower net velocity of individual analytes, i.e., the sum of EOF and EP velocities. This inverted EOF can increase the separation between detection peaks as the proteins reach the detector at different times, according to the equation,

$$s \propto \frac{L}{U_{\mathrm{Net},1}} - \frac{L}{U_{\mathrm{Net},2}}$$

where s is the time separation between molecules, L is the capillary length, and $U_{\mathrm{Net},i}$ is the net velocity of each analyte (i). Coating the capillary surface has other advantages beyond changing the EOF velocity, including increasing the solubility of proteins in the run buffer and preventing the irreversible adsorption of proteins to the surface;[8] these effects induce broader peaks and variable migration times in consecutive separations. Therefore, cationic surface coatings may be deposited to increase separation efficiency and repeatability in CE.

Cationic surfactants are one example of coating agents widely employed in CE to improve separation of proteins, DNA, and or other biomolecules as an electric field drives them toward a detector.[7,8,12] The adsorption of surfactants to the inner surfaces of a capillary allows for stable EOF across a wide pH range, enhanced protein solubility, and decreased surface fouling.[13–15] Controlling the magnitude and direction of EOF using cationic coatings has improved the efficiency and repeatability of CE separations.[14,16–19]

Surface Charge and Electrokinetic Transport

The EOF velocity is directly proportional to the net charge of the capillary surface.[11] When a surface is exposed to a solution of dissolved ions, molecular groups on the surface rapidly exchange protons and ions with the solution (Figure 2). For example, silanols on a silica surface accept protons from an aqueous buffer solution in low pH to induce a net-positive surface charge and donate protons in neutral to high pH to induce a net-negative surface charge.[20] For a negatively charged silica capillary, cations will migrate from the bulk and form the electric double layer (EDL). In the presence of an electric field, these EDL ions migrate toward the cathode via electrophoresis and simultaneously drag the solution in the same direction by electroosmosis due to the viscosity of the fluid.[11] Thus, for a bare capillary with a negative surface charge, EOF drives fluid toward the cathode; in CE separations of basic proteins, EP also drives the cationic proteins toward the cathode, resulting in a higher net velocity, as shown previously in Figure 1.

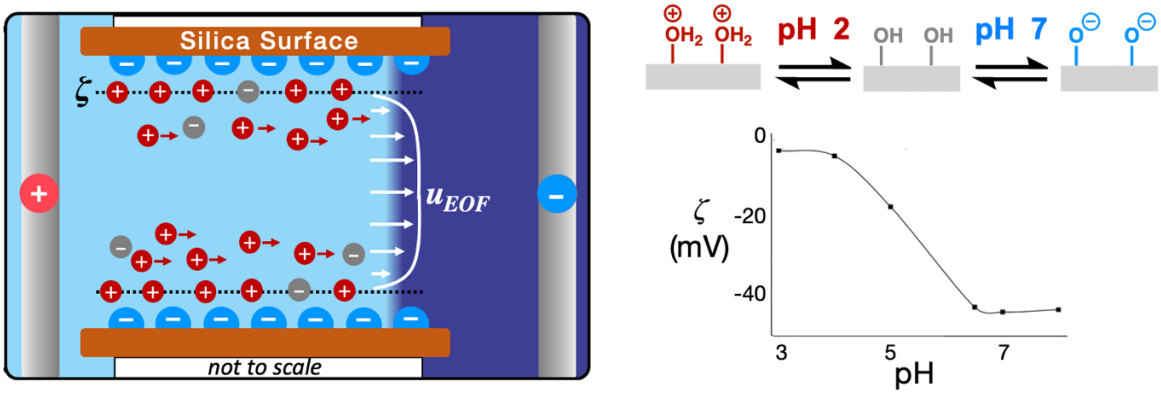

Figure 2. Left: illustration of EOF in a silica capillary. A negative surface with positive EDL ions drives EOF toward the cathodic reservoir. The EOF velocity is directly proportional to zeta potential. Right: dependence of the molecular charge of silica and zeta potential on solution pH, adapted from Corradini and Sprecacenere.[21]

Surfaces that are ideal candidates for microfabrication and electrical measurements (e.g., dielectrics, oxides, metals) are often unsuitable for biosensing due to the variation in surface charge and irreversible adsorption of molecules in biological conditions. These dynamic properties make it challenging to apply such surfaces in continuous analyses, as any change to the surfaces requires the sensor to be recalibrated. To combat this problem, self-assembled monolayers are applied at solid–liquid interfaces to achieve more uniform and/or predictable surface charge, hydrophobicity, and anti-fouling properties.[22] Precise control over these important characteristics has helped prevent undesirable effects such as fouling or bubble formation that can quash the intended application.

The Instability of Surface Coatings

Many molecules self-assemble to form thin coatings on surfaces (e.g., thiols on gold, or silanes on silica), and their chemical structures are easily tuned to promote stability in the intended application environment.[22] For instance, an array of monomer types containing different functional groups are readily applied to these surfaces. For applications requiring long-term stability, such as biosensing and capillary electrophoresis, increasing the carbon length of the coating monomer can promote denser packing and thereby prevent hydrolysis by hydroxide molecules in the solution (Figure 3);[23] however, as the solubility of longer-chain monomers is generally lower than that of shorter-chain monomers, careful selection of the deposition solvent is necessary to achieve high density and stability. The monomer head group(s) and/or tail group(s) can also be modified to induce interactions with the surface, such as electrostatic attraction or covalent bonding. Reactive side groups allow for crosslinking within the coating to improve the hydrolytic stability. Reactive head groups may

be extended (e.g., via polymerization or click-chemistry) to change the thickness, morphology, or functionality of the coating.

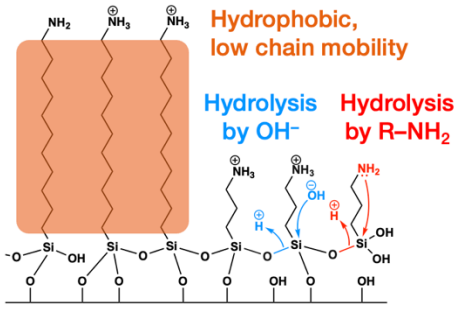

Figure 3. Increasing the carbon-length of aminosilane monomers improves the stability of covalent bonds anchoring the coating to a surface. Increased hydrophobic interactions and denser packing restricts the mobility of the amine-headgroup and the permeability to hydroxide molecules.

Cationic coatings, such as aminosilanes or alkylammonium surfactants, are commonly used in CE in low pH where they have high stabilities against hydrolysis; in neutral to high pH, however, these coatings degrade rapidly, which restricts their application to only separations of mostly acidic proteins.[24,25] For instance, Shulman *et al.* showed that the semi-permanent surfactant, dioctadecylammonium bromide (DODAB), has high stability in pH 3.5 phosphate but deteriorates over several separations in pH 7 or higher (Figure 4).[24] This desorption is believed to occur by a mechanism where hydroxide molecules in solution and surface silanols oxidize the quaternary amine headgroup to a tertiary amine. Studies to more thoroughly examine this degradation, however, show varying kinetic mechanisms in different solution and/or transport conditions[13,26,27] and typically have low temporal resolutions as they use low frequency analysis methods.

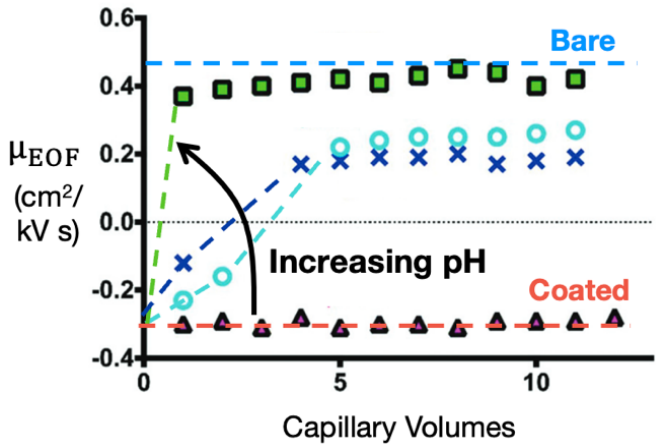

Figure 4. Stability of DODAB-coated capillaries in varying solution pH in an electric field, adapted from ref. 24 with permission from The Royal Society of Chemistry.[24]

As coating stability depends on many factors (e.g., pH, ionic strength, buffer type),[28] comprehensive studies of desorption mechanisms in these conditions are necessary to understand the timescales a coating can be used before requiring regeneration. In CE, coating regeneration is often employed between runs due to the high instability of cationic surfactant coatings in neutral to high pH.[24] Furthermore, the rapid changes in coating density over timescales shorter than a typical CE run (~10 min) have proven difficult to measure. Due to the widespread use of surfactant coatings in CE, more comprehensive studies of coating stability across a range of conditions (e.g., solution, transport and chemical) are necessary to identify optimal coating procedures and applications. By applying a high-resolution technique to monitor coating degradation and elucidate degradation mechanisms in CE conditions, more stable coatings can be developed which improve the repeatability of separations by preventing protein adsorption and reducing band broadening.

Current Methods to Monitor Surfaces Reactions

Self-assembled monolayers are easily deposited on many surface types and geometries (e.g., planar, curved, microchannel). However, our knowledge of adsorption–desorption dynamics is informed by surface analyses that are mostly *ex situ* and limited to planar substrates. Nevertheless, these analyses have identified advantageous conditions for the formation and application of such coatings. For instance, studies of coating formation and stability have been performed using water contact angle (WCA),[23,25,29–33] ellipsometry,[23,25,29–35] X-ray photoelectron spectroscopy,[25,29,33,36–38] Fourier-transform infrared spectroscopy,[31,34,35,37] atomic force microscopy,[23,25,32–34,38] fluorescence imaging,[29,31,39,40] and zeta potential analysis.[1,25,38,41,42]

With the exception of fluorescence imaging and zeta potential analysis via the current monitoring method,[43] these methods are performed *ex situ* and require significant manual interaction, which limit their ability to resolve coating dynamics in conditions where the rates of self-assembly or dissociation are rapid. For example, Giraud et al. used WCA to compare the final coating stabilities of different aminosilane monomers, but were unable to accurately resolve the dissociation kinetics as the measurement samples were extracted at intervals more than an hour apart.[23] Kunc et al. determined the concentration of aminosilanes on silica nanoparticle surfaces more quantitatively using a novel ^{1}H NMR technique.[44] Unfortunately, this *ex situ* technique is limited to deuterated solvents and requires extensive sample preparation and two separate analyses (of NP surfaces and the supernatant liquid) in order to extract dissociation kinetics, resulting in a maximum resolution of one measurement per 8 h. These examples highlight the slow, manual nature of most surface analysis techniques, which

has hindered our understanding of coating and degradation processes occurring over rapid and/or long timescales.

Recent *in situ* analysis techniques demonstrate nondestructive, continuous monitoring of reactions at surfaces, such as streaming current analysis of zeta potential (SZP),[25,45] current monitoring analysis of zeta potential (CM),[43,46] Fourier-transform infrared spectroscopy (FTIR),[47] nuclear magnetic resonance spectroscopy,[44] X-ray photoelectron spectroscopy (XPS),[48] and evanescent wave spectroscopy.[49] Of these in situ techniques, SZP and CM are the only to offer analysis of enclosed microchannel surfaces at sufficient frequencies to resolve fast surface reactions. For example, Okhrimenko et al.[25] studied the kinetics of APS removal from silica surfaces using SZP and achieved a measurement frequency of 1.8 mHz, but their resolution of the reaction was limited by a delay incurred during assembly of the sample holder following surface coating. Almutairi et al.[50] demonstrated continuous zeta potential measurements using CM; however, their use of a constant measurement interval was not suitable for studying reactions with arbitrary or unknown kinetics. These examples highlight a need for fully automated, in situ analysis techniques that can accommodate variable reaction conditions and efficiently analyze coating species and conditions.

What is Needed to Understand Coating Degradation in CE

To understand the rapid degradation of cationic coatings in CE conditions, we need a higher frequency, *in situ* measurement platform that can measure a wide range of solution and transport conditions. Higher measurement frequency allows for improved resolution during these complex degradation processes, while greater versatility allows us to understand the mechanism more thoroughly with respect to key variables in CE. Zeta potential has long been used to quantify molecular charge and charge density on a surface.[1,25,38,42,51–54] As

aminosilanes and cationic surfactants spontaneously assemble onto silica surfaces and thereby change the overall charge,[38,42] *in situ* analysis of zeta potential (a measurable proxy for surface charge) allows us to monitor these reactions.

In this work, we present a continuous, marker-less method for analyzing zeta potential of microchannel surfaces in real-time, which we call Automated Zeta Potential Analysis (AZA). We apply this platform to understand the mechanisms of aminosilane coating density and stability on microcapillary surfaces, which are pertinent characteristics to their application in continuous bioanalytical platforms such as capillary electrophoresis. We further demonstrate our technique for the study cationic surfactants, which adsorb and desorb to silica surfaces more rapidly and undergo complex spatiotemporal changes in transport during these reactions. First, we review the theory behind measuring zeta potential and describe our approach for performing continuous measurements and analysis in real time. Then, we validate our method by measuring zeta potential for a bare silica surface in solutions of varying pH and compare the kinetic timescales and zeta potential values with prior literature.

I. Real-Time Zeta Potential Analysis of Microchannel Surfaces during Aminosilane Deposition and Exposure Using Current Monitoring

This chapter and Appendix A (Sections 1–4) have been reprinted with permission from: Abrams, A. S.; Eden, A.; Zhou, L.; Wang, B.; Huber, D. E.; Pennathur, S. Real-Time Zeta Potential Analysis of Microchannel Surfaces during Aminosilane Deposition and Exposure Using Current Monitoring. ***Anal. Chem.*** **2021, *93* (49), 16512–16519.**

Abstract: Surface coatings are extensively used in capillary electrophoresis to increase separation efficiency and resolution. Stability across a wide pH range is desirable to achieve high repeatability and efficiency; therefore, a comprehensive understanding of coating degradation timescales is needed. We present a novel platform for automated zeta potential analysis based upon current monitoring that delivers improved time resolution over existing methods. Using our platform, we measure zeta potential continuously during aminosilane coating reactions and infer changes in surface composition. We found that the change in zeta potential after coating depended on monomer type and solvent, while its stability was influenced by coating solvent and exposure pH. Our versatile platform provides an elegant approach for evaluating the molecular composition, reactivity, and stability of surfaces in real time.

Introduction

The stability of surface coatings is critical to the development of reproducible separations in capillary electrophoresis with high resolution and efficiency.[17] The design of new coating chemistries has enabled greater control over surface charge distribution and long-term

stability in varying pH and aqueous–organic solvent mixtures.[55] Aminopropylsilanes (APS) are molecules commonly used to functionalize silica and polydimethylsiloxane surfaces, as well as other oxides and organic films. These coatings are employed for a variety of applications, including immobilization of biomolecules on surfaces,[5,56] control of electrophoretic mobility,[16] and stabilization of nanoparticles.[41] Despite their widespread use, aminosilane coatings exhibit poor stability in aqueous conditions, with complete hydrolysis occurring in a few hours.[57–59] Coatings with longer lifetimes are highly desirable, but their development requires a more comprehensive understanding of self-assembly and hydrolysis mechanisms than can be achieved using existing analytical techniques. Therefore, a better understanding of APS dynamics will significantly aid the wide range of applications that require robust coatings.

1. Theory and Design

When a solid surface contacts an ionic solution, the exchange of protons creates charged surface species (e.g., SiO^-, $SiOH_2^+$). This net charge promotes a redistribution of ions to form a charge-screening electric double layer, or EDL (Figure 1b).[45] Zeta potential, defined as the change in potential across the diffuse layer, is a key property of the EDL and governs electroosmotic flow (EOF).

Since zeta potential reflects the average surface charge density, *in situ* zeta potential analysis enables the monitoring of reactions that change a surface's charge, such as the self-assembly of aminosilanes onto silica surfaces.[1,25,38,42,51–53] To exploit this, we adapted the conventional CM approach for continuous, automated analysis of zeta potential. EOF occurs when a tangentially applied electric field causes diffuse-layer ions to migrate by

electrophoresis.[60] Since the diffuse layer is non-neutral in overall charge, this region experiences a net electrical force that causes the viscous solution to flow.

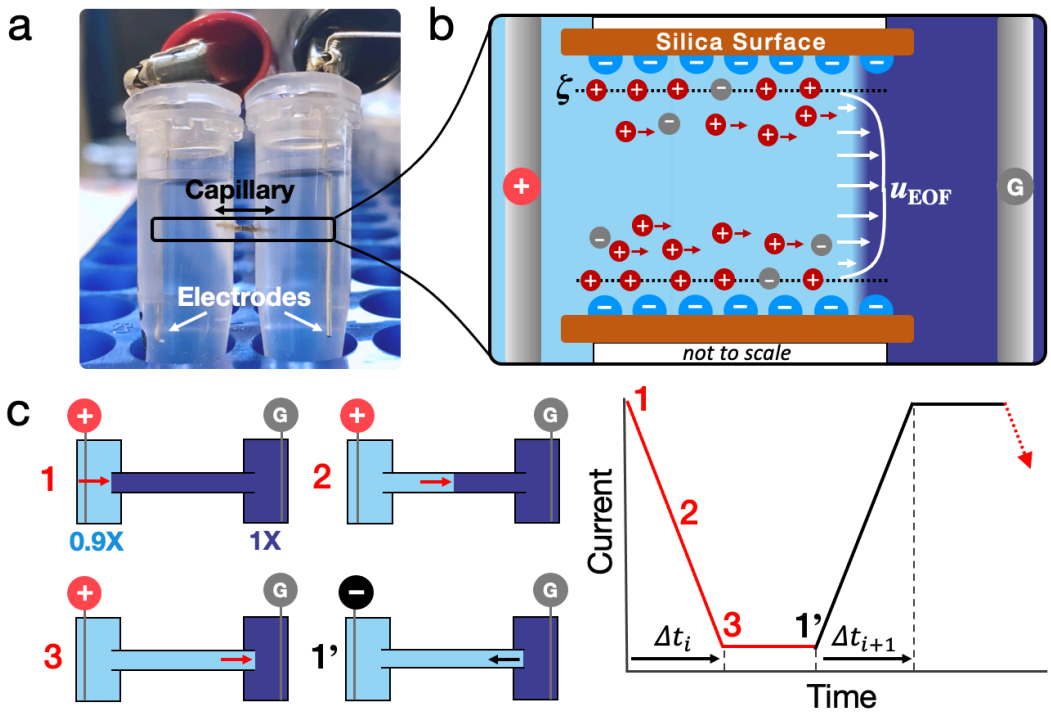

Figure 1. Automated zeta potential analysis (AZA). (a) Image of experimental apparatus. A silica capillary bridges two reservoirs with electrodes used to drive electroosmotic flow (EOF) and monitor current. (b) Schematic of charge distribution in the capillary, which dictates zeta potential (ζ) and EOF velocity (u_{EOF}). A potential is applied between source (+) and ground (G) electrodes to generate EOF. (c) Schematic of AZA measurement cycle showing EOF-driven solution traversals and measured current.

In a microchannel filled with ionic solution above 1 mM, the relatively thin diffuse layer (~1 to 10 nm) ensures that EOF velocity (u_{EOF}) is effectively uniform across the diameter.[45,61,62] In microchannels with homogeneous surface charge density,[63] EOF velocity

can be directly related to zeta potential (ζ) using the Helmholtz–Smoluchowski relationship (eq 1),[11]

$$\zeta = u_{EOF} \frac{\mu}{\epsilon_r \epsilon_0 E_0} \quad (1)$$

where μ is the dynamic viscosity, ϵ_r is the relative permittivity, ϵ_0 is the vacuum permittivity, and E_0 is electric field strength.

In current monitoring, one can infer EOF velocity and zeta potential from changes in measured current as EOF drives different conductivity solutions through a microchannel (Figure 1c).[43,46] Ohm's law relates electric current (I) to conductivity (σ), electric field strength, and cross-sectional area (A_0):

$$I = \sigma E_0 A_0 \quad (2)$$

EOF velocity is found by dividing the channel length (L_0) by the solution traversal time (Δt), indicated by a plateau in measured current after applying the electric field:

$$u_{EOF} = L_0 / \Delta t \quad (3)$$

Finally, zeta potential is determined by inputting the calculated EOF velocity into eq 1.

To analyze zeta potential in real time, we adapted the CM method and designed a microfluidic platform and electrical control system for closed-loop analysis of EOF velocity using traversal time. Our fluidic system (Figure 1a) has two reservoirs connected by a silica microcapillary. The reservoirs contain distinct solution concentrations and electrodes connected to a voltage source and current meter. While it shares many features common to prior CM systems,[43,46,64] our system was tailored to increase measurement frequency by using short capillaries and high electric field strengths. The solution composition of each reservoir was maintained by using a small channel diameter and large, capped reservoirs (see Supporting Information). By implementing this design, we achieved stable measurement of

surface reactions at frequencies up to 0.2 Hz; even higher frequencies may be obtained by applying higher voltages or reducing the capillary length, subject to transport limitations.

We implemented an algorithm with active feedback to determine zeta potential at high frequency using measured EOF traversal time. Our algorithm controls alternating solution traversals across a capillary by applying an electric field between reservoirs (Figure 1c). Initially, we place full strength (1X) solution in the right reservoir, filling the channel by capillary action, and 10% diluted (0.9X) solution in the left reservoir. When a positive voltage is applied at the left reservoir (+), 0.9X solution flows through a channel with a negatively charged surface (Figure 1b) and the measured current decreases. When 0.9X solution arrives at the right reservoir, the current stabilizes. AZA detects the traversal endpoint in real time by identifying when the slope of current vs. time drops below a threshold value, which is dynamically calculated by multiplying the average slope by one-third. AZA uses the traversal time in eq 1,3 to calculate EOF velocity and zeta potential. A 10% difference in solution concentrations was large enough to provide sufficient contrast between steady state current levels, yet small enough to ensure subsequent differences in zeta potentials would have a minimal effect (~2-3%) on the measured traversal time.[63] A subsequent delay is introduced to allow current to stabilize, then the voltage polarity is reversed for a new measurement. However, if the current–time slope is too low (e.g., when zeta potential is close to 0 mV), accurate detection of the endpoint is impeded, and the voltage polarity is instead set to alternate at constant 5 min intervals.

2. Experimental Section

2.1. Chemicals

3-aminopropyldimethylmonomethoxysilane, 99%, 3-aminopropyltriethoxysilane, 99%, and 3-aminopropyltrimethoxysilane, 97%, were obtained from Acros. Anhydrous methanol was acquired from Alfa Aesar. 3-aminopropyltrimethylsilane, 97%, was obtained from Gelest. BIS-TRIS, CAPS, citric acid monohydrate, CHES, monosodium phosphate, trisodium citrate, sodium acetate, and MES were acquired from Sigma. HEPES, lithium chloride, sodium hydroxide, sodium chloride, disodium phosphate, and Tris were purchased from Fisher.

2.2. Solution Preparation

1X solutions were prepared of 150 mM NaCl and 20 mM respective buffer in deionized water (18.0 MΩ-cm) and were filtered through 0.4 μm filters before use. pH was measured using an Orion Star™ pH probe (8115BNUWP) and meter (A214) calibrated daily. By adding 10 M HCl or 10 M NaOH solution, pH was titrated within 0.1 units from the buffer's pK_a value. Conductivity was measured with an Oakton® CON 2700 meter, calibrated daily. For experiments with constant conductivity, 2 M NaCl solution or water was added until conductivity was within ± 0.01 S/m of a 162 mM NaCl solution.

2.3. Assembly of Capillary–Reservoir Devices

Capillary–reservoir assemblies were constructed from 1.2 μm polyimide-coated capillary tubing (Molex), cleaved to 8.0 ± 0.1 mm length, and 1.5 mL capped centrifuge vials (Figure 1a). Each capillary was sonicated in water and dried using pressurized nitrogen, then its length was measured with digital calipers for the calculation of EOF velocity. A capillary

was inserted between two reservoirs with small inlets cut in the sides, where a precise fit was ensured to prevent leakages over long experiments. E6000 adhesive was applied to the capillary inlets and was allowed to cure at room temperature for 24 h. Then, different volumes of water were added to each reservoir for 1 to 7 days to induce pressure-driven flow and clear any silica fragments from the cleaving process. Small holes were punched in the reservoir caps to insert the platinum electrodes (0.5 mm diameter).

2.4. Assembly of Capillary–Reservoir Devices

A Tektronix® Keithley 6517a electrometer was used to apply the DC potential and measure current. All instrument parameters, including the timed voltage cycles, were set and initiated by our custom control algorithm in MATLAB® (see Section 1 and Supporting Information).

2.5. Capillary Conditioning

After device assembly, capillaries were conditioned by filling both reservoirs with 1 M NaOH and applying 30 kV/m for 10 min. EOF was verified by measuring a stable current near the value predicted by Ohm's law (eq 2). Then, reservoirs were filled with water and a 30 kV/m field was applied for 10 min or until the current was below 100 pA. Finally, source and ground reservoirs were respectively filled with 0.9X and 1X TBS solutions (pH 8.3) and AZA was applied at ±30 kV/m for 5 min. To proceed to experiments, each capillary was verified to have an average 1X current and zeta potential within the range shown in Table 1.

2.6. Equilibrium Zeta Potential–pH Experiments of Bare Capillary

The capillary was flushed for at least 15 min to allow equilibration of surface charge in each set of pH-buffered saline solutions (Figure 2c). Then, AZA was applied to measure zeta potential for calculation of mean values and 95% confidence intervals (Table S2).

2.7. Coating Formation and Stability Experiments

At 0 h, APS monomers were added to both reservoirs to achieve a final concentration of 1 mM in 0.9X/1X TBS (20 mM Tris, 150 mM NaCl, pH 8.3) or AMS (50 mM LiCl in anhydrous methanol) solutions. We applied an electric field strength of 30 kV/m in TBS and 120 kV/m in AMS. After 6 h of coating, silane solutions were discarded and replaced with the indicated pH-buffered solution (Table S3). Zeta potential was monitored up to 70 h, then the reservoirs were filled with the same solutions and zeta potential was remeasured.

3. Results and Discussion

3.1. Validation: Zeta Potential of Silica vs. pH

To validate AZA, we measured zeta potential of a silica capillary in different buffer and pH solutions. Since the solution-based protonation reactions of surface silanols reach equilibrium in short timescales (15 s for silica gels),[65] we quantified the temporal resolution of AZA by estimating the time for zeta potential to stabilize after a solution exchange. After exchanging 0.9X and 1X reservoirs with solutions of different buffer type or pH, steady-state currents and zeta potentials stabilized in 1 to 3 min (Figure 2a,b). We attribute this transient period to the rate of advective transport (i.e., EOF velocity) in each condition (Table S1). Generally, zeta potential became more negative with increasing pH, reflecting a greater number of deprotonated silanols (SiO^-) above the pK_a near 6.6 to 8.0.[66]

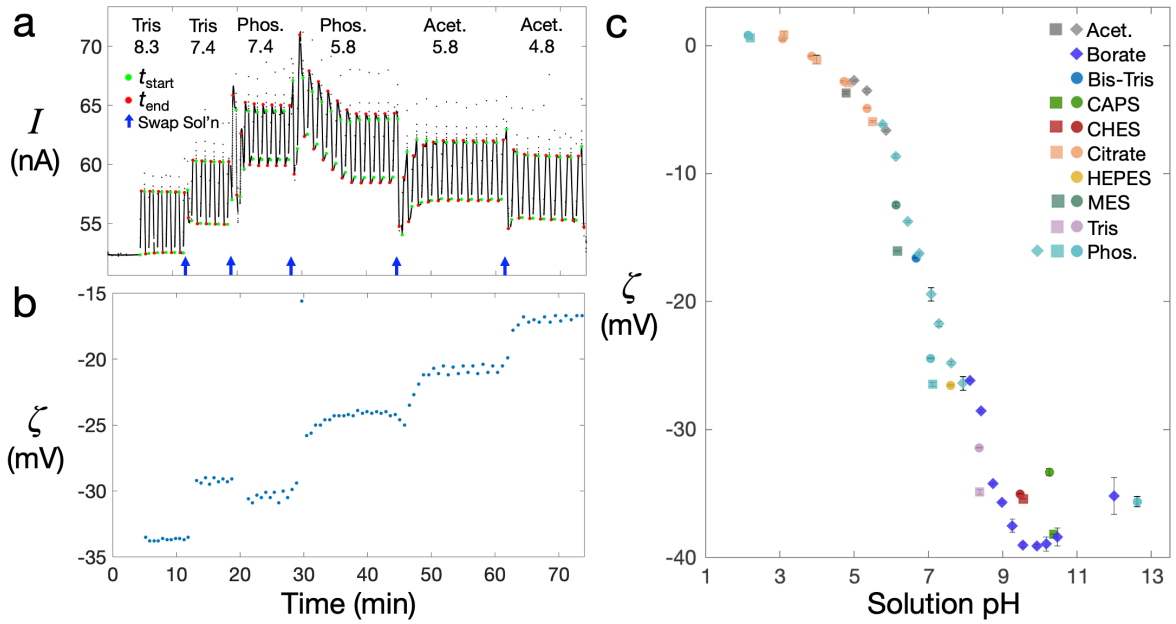

Figure 2. Zeta potential response of the bare capillary exposed to solutions of varying pH or buffer type. (a) Current monitoring cycles and (b) zeta potential calculated using automatically detected EOF traversal times in (a). At indicated times, 0.9X/1X reservoirs were refilled with varying buffer (tris, phosphate, acetate) and/or pH (8.3, 7.4, 5.8, 4.8) solutions composed of 20 mM buffer and 150 mM NaCl. Measured conductivities of 1X solutions were 1.59 to 1.84 S/m. (c) Equilibrium time-averaged zeta potential vs. pH response (data in Table S2). Error bars represent 95% confidence intervals. Capillary size (d x L): 1.2 µm x 8.0 mm (■/●), 1.1 µm x 23.9 mm (◆). Buffer concentration: 20 mM (■/●), 10 mM (◆).

To investigate the precision and accuracy of our zeta potential readings at different pH conditions, we extracted the average equilibrium zeta potential after exposure of a bare capillary to buffered solutions ranging from pH 2.1 to 12.6 (Figure 2c). While our zeta potentials were slightly larger than their corresponding measurements in 0.1 M KCl,[67] the shapes of the responses were nearly identical. We used an array of buffers to span this pH range, where we titrated pH within 0.1 units of each buffer's reported pKa.[68] While changes

in buffer could influence zeta potential beyond that of pH alone (e.g., due to differential adsorption), we observed less than 0.6 mV difference in zeta potential across buffer transitions at similar pH (e.g., acetate pH 5.8 to phosphate pH 5.8, phosphate pH 7.9 to borate pH 8.1; see Table S3).

When the solution pH was outside the stable buffering range ($pK_a \pm \sim 0.5$), we observed behavior that was inconsistent with the changes in ionic strength and buffer valency. In Figure 2a,b, zeta potential magnitude increased with steady-state currents in the transitions from pH 7.4 Tris to phosphate and pH 5.8 phosphate to acetate; we expected a lower zeta potential magnitude with higher ionic strength, as surface charge is screened more effectively. We hypothesize that these discrepancies arose as solution pH drifted toward the respective pK_a value of the buffer.

3.2. Monitoring APTMS Coating Formation and Degradation in Aqueous Conditions

We first applied AZA to study coating formation and stability of 3-aminopropyltrimethoxysilane (APTMS). In Figure 3, we monitor zeta potential growth across 6 h coating formations and subsequent zeta potential decay over 42 h after replacing 0.9X and 1X reservoirs with silane-free solutions of varying pH and buffer (Table S3).

In Figure 3a, we indirectly monitor the rate of APTMS coating formation on bare capillaries after adding 1 mM APTMS to 0.9X/1X reservoirs of pH 8.3 Tris-buffered saline (TBS). Within 35 min, zeta potential increased from roughly –30 to +2 mV. We note that zeta potential was not measured from –2 to +2 mV as the EOF traversal time exceeded the maximum cycle time of 5 min. By 6 h, zeta potential settled at +15.3 ± 1.1 mV for seven capillaries. While prior studies show poor reproducibility of APS films deposited in

solution,[33,69] we observed repeatable kinetics, alluding to a greater control of reactant availability (e.g., concentration, flow rate) at the surface.

In Figure 3b, we investigate the zeta potential response after exposing APTMS-coated capillaries directly to silane-free solutions of varying pH and buffer. Initial zeta potentials generally increased with decreasing solution pH, reflecting a greater number of protonated amines on the surface below the pKa of 10.5. Over time, zeta potential decayed toward the value measured for bare silica (Figure 2c). We verified that the solution composition did not drift over these timescales by exchanging the reservoirs with fresh solutions and remeasuring zeta potential and current at the end of each experiment.

In Figure 3c, we more quantitatively examine the zeta potential–pH response of APTMS coatings over time by replotting a sample of values in Figure 3b against solution pH. We include the bare capillary response from Figure 2c as a baseline for expected long-term behavior. The zeta potential response measured directly after coating (APS 0 h) was similar to previous reports,[25,70–72] where we observed a maximum in zeta potential at pH 2.1 and a mostly linear decay from pH 4.9 to 10.5. We interpolated the isoelectric points of APTMS and bare surfaces at pH 9.1 and 3.4, respectively; this transition was expected as aminosilanes replaced surface silanols and effectively increased the pK_a of the surface.[73,74]

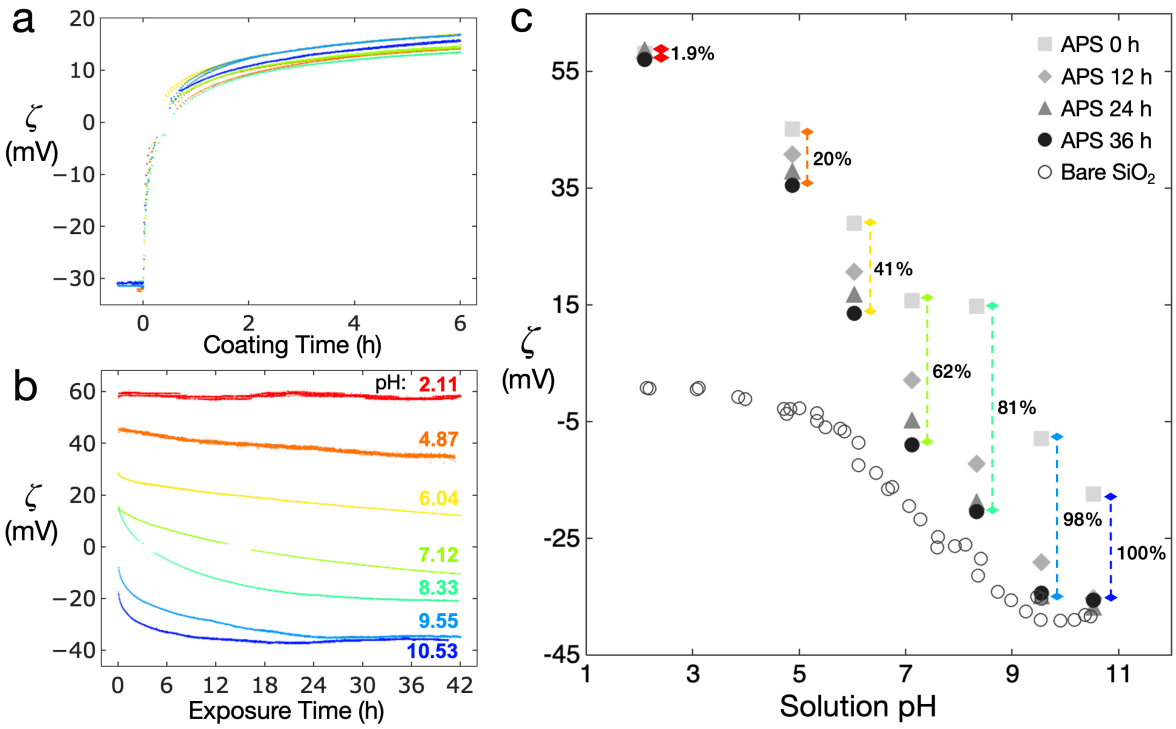

Figure 3. Zeta potential response of (a) 6 h coating formations (1 mM APTMS in pH 8.3 TBS) and (b) subsequent exposure to silane-free solutions of varying pH and buffer type (details in Section 2.7 and Table S3). Colors represent single capillaries through coating formation in (a) and direct exposure in (b). (c) Extracted zeta potential vs. pH and exposure time in (b), with the bare capillary response (Figure 2c) included for reference. Normalized zeta potential decay (%) after 36 h exposure was calculated with eq 4,5.

We calculated normalized zeta potential (ζ_{norm}) and percent decay by the following equations,

$$\zeta_{norm}(t) = \frac{\zeta_d(t) - \zeta_{bare}}{\zeta_{d,0} - \zeta_{bare}} \quad (4)$$

$$\% \text{ decay} = \left(1 - \zeta_{norm}\right) \times 100\% \quad (5)$$

where ζ_{bare} is the mean zeta potential of the bare surface at equilibrium, $\zeta_d(t)$ is the zeta potential of the APTMS-coated surface at a given dissociation time, t, and $\zeta_{d,0}$ is the corresponding zeta potential at the start of each degradation. In pH 2.1 solution, zeta potential experienced less than 2% decay, supporting the notion that acidic conditions reduce the rate of hydrolysis.[59] By fitting the 36 h decay values from pH 4.7 to 8.3, we found a linear decay rate of 17.9% per pH unit (Figure S2). Compared to prior studies, our measurements demonstrate the effect of pH on APS coating stability more quantitatively and across a wider pH range.[25,59]

While the stability of APS films vs. pH has been studied using low-resolution, *ex situ* techniques,[23,29,44] few have extracted the kinetics of APS degradation at high frequency. Okhrimenko *et al*.[25] monitored the rate of zeta potential decay of APTMS-coated silica in pH 5 deionized water, where they employed SZP with an average frequency of 1.8 mHz. At pH 4.9, we monitored zeta potential at a 24-fold higher frequency (44 mHz) and resolved the decay kinetics at pH 10.5, where they were 5-fold faster. We compared the relative rate of zeta potential decay after 21 h by applying the same normalization to both studies (eq 4,5); while we use higher salt concentrations and shorter deposition times, our 21 h decay value was 3-fold smaller. This discrepancy highlights a need for more comprehensive *in situ* studies of coating formation and degradation kinetics to identify key variables affecting final stability.

3.3. Influence of Monomer Type and Solvent on APS Coating and Degradation

We extended AZA to monitor coating formation of three APS monomers in aqueous and anhydrous solvents and compared their subsequent stabilities in TBS. To use AZA in organic solvents, it was necessary to find an appropriate soluble salt to increase the conductivity to

near that of aqueous solution. We added 50 mM LiCl to anhydrous methanol saline (AMS) to generate adequately high currents for analysis of EOF velocity. A similar strategy may be applied to other solvents used commonly in capillary electrophoresis.[55,75]

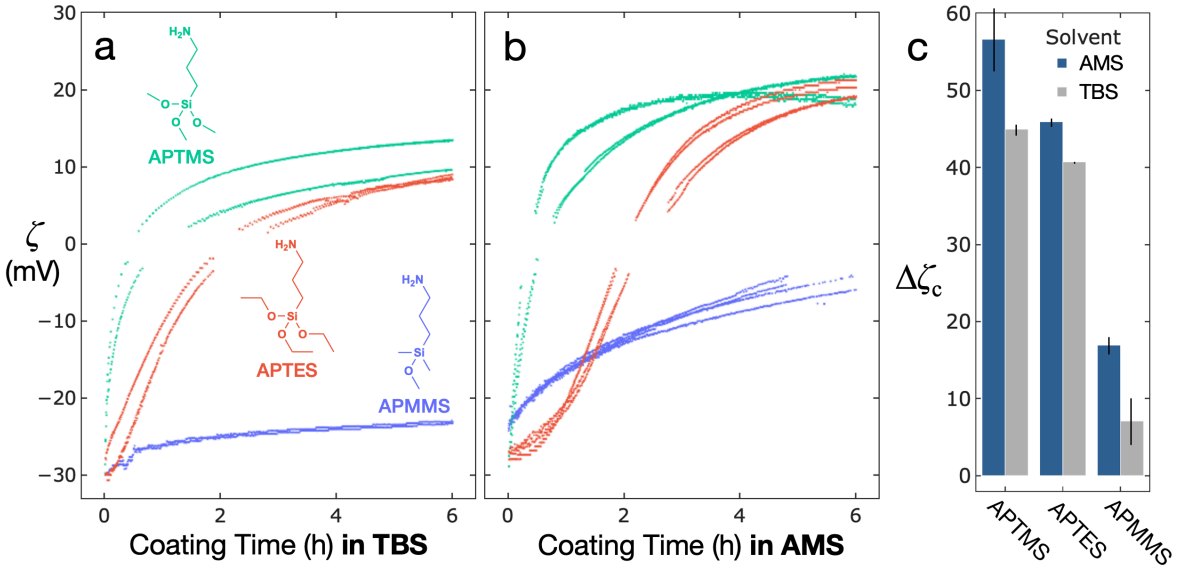

Figure 4. Zeta potential response of 6 h coating formations in aqueous or anhydrous conditions. At 0 h, each APS monomer was added at 1 mM final concentration to 0.9X/1X reservoirs of (a) pH 8.3 TBS at 30 kV/m or (b) AMS (1X: 50 mM LiCl in anhydrous methanol) at 120 kV/m. (c) Average change in zeta potential measured in TBS before and after 6 h coating formations in (a-b). Error bars represent 95% confidence intervals.

3.3.1. Coating in Aqueous and Anhydrous Solvents

To compare the zeta potential growth kinetics of different coating species and solvents, we first considered the differences in advective transport in TBS and AMS. We minimized these disparities in measured EOF velocity and current by using a 4-fold higher electric field

in AMS (Table 1). Figure 4 shows the zeta potential growth kinetics after addition of APTMS, 3-aminopropyltriethoxysilane (APTES), or 3-aminopropyldimethylmonomethoxysilane (APMMS) at 1 mM final concentration to TBS or AMS reservoirs.

In TBS, the APS monomers exhibited distinct and repeatable zeta potential kinetics (Figure 4a). Initial zeta potentials were nearly identical to the bare surface value of –30 mV (Table 1), indicating that the addition of silane had no immediate effect on the net surface charge in TBS. Over the 6 h depositions, zeta potential reached +13.6 ± 1.9 mV, +8.7 ± 0.6 mV, and –23 mV for APTMS, APTES, and APMMS, respectively. By 1 h, APTMS showed the largest change in zeta potential, increasing 80 ± 3% of its total change in zeta potential after 6 h; in contrast, APMMS and APTES increased 62 ± 4% and 43 ± 11%, respectively, of their 6 h changes (Figure S3). The smaller growth of APTES vs. APTMS supports previous findings that the hydrolysis step is slower for ethoxy- vs. methoxy-silanes.[76,77] The little change in zeta potential observed for APMMS after 6 h indicates that a greater number of alkoxy groups may be necessary to increase coverage in this condition. While aminosilanes may also adsorb via interaction of their amine headgroup with surface silanols,[33] we hypothesize this mechanism is not prevalent in our conditions. To confirm, we monitored the deposition of an alkoxy-less APS monomer (3-aminopropyltrimethylsilane) over 16 h in TBS and observed little change in zeta potential, with a response matching that of a bare capillary in silane-free TBS (Figure S4).

Table 1. Parameters and measurements of a bare capillary in 1X solutions at 25 °C

Solutions	TBS	AMS
μ (mPa-s)	0.890	0.585
ϵ_r	78.4	32.7
E_0 (kV/m)	30	120
I_{ss} (nA)[1]	59.9 ± 3.5	37.3 ± 2.1
ζ (mV)	–29.9 ± 1.6	–18.1 ± 3.0
u_{EOF}	0.70 ± 0.04	1.07 ± 0.18

[1]Average steady-state currents of 1X solutions.

In Figure 4b, analogous depositions in AMS displayed similar kinetic differences between monomer types. Initial zeta potential values varied significantly between monomers and were higher in magnitude than the bare surface value of –18 mV (Table 1); this variation suggests the addition of silane monomers induces distinct pH changes in AMS. After 1 h, zeta potentials of APTMS, APTES, and APMMS increased 69 ± 2%, 14 ± 3%, and 38 ± 2%, respectively, of their total 6 h changes in AMS (Figure S3). The gradual increase in slope for APTES from 0 to 1 h again supports the slower hydrolysis of ethoxy- vs. methoxy-silanes, as hydrolysis appears a rate-limiting step in our conditions.[78]

By measuring zeta potential in TBS before and after the 6 h depositions, we compared the total changes in zeta potential in TBS ($\Delta\zeta_c$, Figure 4c). We observed $\Delta\zeta_c$ increased with the number of alkoxy groups and their relative rates of hydrolysis ($\Delta\zeta_c$ of APTMS > APTES > APMMS in both solvents). Coating solvent also played a significant role, as we observed 1.2-, 1.3-, and 1.9-fold increases in $\Delta\zeta_c$ for APTMS, APTES, and APMMS depositions in AMS vs. TBS, respectively. This trend supports the notion that anhydrous solvents produce coatings with a higher density of surface reactive amines.[31]

3.3.2. Stability of Aqueous and Anhydrous Coatings

We evaluated the effects of alkoxy structure and coating solvent on zeta potential stability in a common exposure condition, TBS pH 8.3. In Figure 5, we show the normalized zeta potential (ζ_{norm}) response (eq 4) of APTMS and APTES coatings after deposition in TBS or AMS (Figure 4a,b).

We quantify the stability of APS coatings deposited in AMS or TBS solvent by comparing the time for ζ_{norm} to decay by 50% ($t_{1/2}$). The $t_{1/2}$ values of APTMS and APTES deposited in AMS were respectively 1.8 and 1.4 h, which are 78% and 74% lower than the same monomers deposited in TBS (8.1 and 5.3 h, respectively). This nearly 4-fold difference in stability indicates a difference in coating structure produced in each solvent; subsidiary analysis techniques (e.g., XPS) may reveal structural differences, like the ratio of covalently attached vs. weakly bound monomers.[36] Interestingly, the $t_{1/2}$ values were more similar for monomers deposited in AMS vs. those in TBS (16% vs. 35% variance). This larger separation in TBS suggests the rate of alkoxy hydrolysis had a more significant role on final stability in this condition.

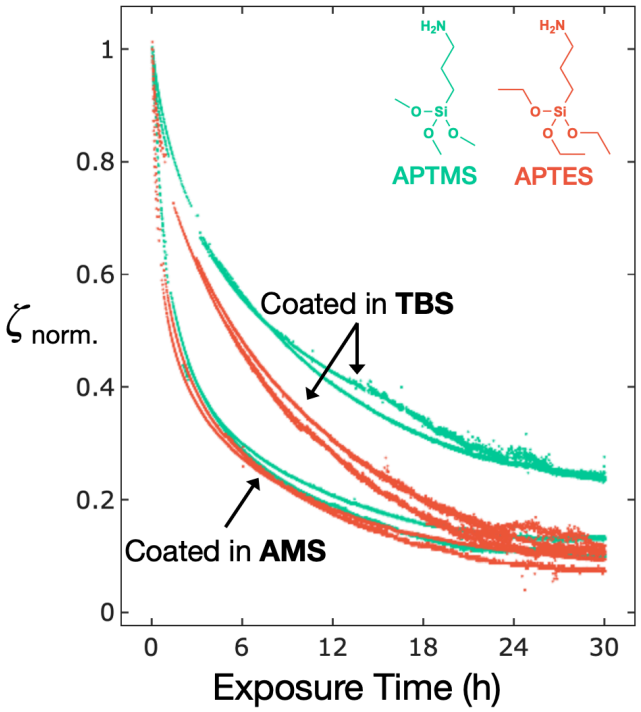

Figure 5. Normalized zeta potential response of TBS- or AMS-deposited coatings (6 h depositions in Figures 4a-b) after exposure to silane-free, pH 8.3 TBS solution. Raw zeta potential responses (Figure S5) were normalized with eq 4.

4. Conclusion

The rapid hydrolysis of APS coatings in aqueous conditions limits their utility in many applications, such as in capillary electrophoretic separations.[17] The development of more robust surface coatings requires *in situ* analysis systems that can monitor coating and degradation processes in a wide array of conditions, with sufficiently high frequency to resolve these reactions.[25,44,47,79] We developed an automated zeta potential analysis (AZA) platform with several ideal characteristics for continuous monitoring of surface reactions, including: fully electronic measurements, an enclosed fluidic design that is scalable and

multiplexable, a tunable flow rate via applied voltage, and flexibility in choice of solvent and coating conditions.

We applied AZA to extract differences in zeta potential growth and decay kinetics of APS monomers deposited in aqueous and anhydrous solutions. We observed large differences in zeta potential stability for coatings exposed to varying pH solutions, where we monitored APS degradation at a 24-fold higher frequency than a similar study using SZP.[25] We observed a 4-fold improvement in zeta potential stability for APS monomers deposited in TBS vs. AMS solvents, suggesting that more studies in other solvents are needed to improve our understanding of degradation mechanisms. These preliminary results substantiate AZA as a robust, fully automated method for analyzing zeta potential at high resolution during surface coating and degradation processes. In future work, we propose to investigate the effects of transport conditions (e.g., flow rate, diameter, silane concentration) on APS coating kinetics and final coverage, which was previously only examined for vapor-phase depositions.[80]

II. Electrokinetic Transport of Cationic Surfactant Induces Stagnant Regimes in Capillary Adsorption and Desorption

Abstract: Cationic surfactant coatings are commonly used in capillary electrophoresis (CE) to control electroosmotic flow (EOF) and thereby improve separation efficiency. However, our understanding of surfactant adsorption and desorption in conditions relevant to CE are limited by the low-frequency techniques used to infer zeta potential from the EOF mobility. We apply the automated zeta potential analysis (AZA) platform to study adsorption and desorption of the cationic surfactant, cetyltrimethylammonium bromide (CTAB), by continuously monitoring zeta potential at frequencies up to 0.12 Hz within a silica microcapillary. In contrast to other studies, we observe slow reaction kinetics at distinct positive zeta potential ranges during CTAB adsorption and desorption. In these ranges, the EOF mobility significantly counteracts the electrophoretic (EP) mobility and hinders the net electrokinetic transport (EOF+EP) of CTA^+; we call these transport-limited periods "stagnant regimes." By varying the capillary diameter and alternating voltage sequence, we show that the capillary surface-area-to-volume ratio and the net transport of CTA^+ strongly influence the reaction kinetics. Through numerical simulations and normalization of experimental data in terms of net-CTA^+-transport-volume-over-surface area, we reveal that the EP mobility of CTA^+ and the surface-area-to-volume ratio of the capillary dictate the reaction kinetics and the zeta potential range over which the stagnant regime occurs. Armed with this knowledge, we constructed an AZA algorithm that maintains a fixed transport volume of CTA^+ as the EOF mobility changes over time, thereby accelerating the stagnant regime and reaction kinetics.

Introduction

The mechanism of surfactant adsorption at solid–liquid interfaces is an interesting topic that remains relevant to many applications such as capillary electrophoresis (CE), corrosion prevention, oil recovery, and colloid stability (e.g., quantum dots, droplets).[12] Numerous studies have investigated the kinetic and thermodynamic properties of surfactant coatings on open, planar interfaces using techniques such as atomic force microscopy,[81,82] optical reflectometry,[83–85] and neutron reflectometry.[86] In these well-understood systems, first-order reaction kinetics and diffusion govern the rate of surfactant adsorption and desorption at the surface.[83–85,87–89] The study of surfactant dynamics in confined CE systems (i.e., a microcapillary under a DC electric field), however, requires closer attention to the transport and volume limitations that are coupled to the reactant concentration and adsorption kinetics (e.g., the surface-area-to-volume ratio, net velocity of the surfactant, capillary length). The relationship of these variables with the kinetics remains unclear, as previous studies in microchannels use different conditions and display varying kinetic mechanisms (exponential vs. linear).[13,26,27] Therefore, studies using a wider range of capillary transport and solution conditions are necessary to develop a thorough understanding of the kinetics in these conditions.

The effect of surfactant transport (e.g., electrokinetic, pressure-based, diffusive) on the observed kinetics of adsorption and desorption are not well understood and are difficult to model.[13,26,28,90] For instance, Yassine and Lucy showed that the EOF stability of a capillary coated with didodecyldimethylammonium bromide (DDAB) depended on the net volume flushed through the capillary, regardless of whether the flow was driven by EOF or pressure.[28] Wang and Lucy monitored the stability of a capillary coated with

cetyltrimethylammonium bromide (CTAB) and observed a linear decay in EOF to near that of glass over 70 min. In similar conditions, Melanson *et al.* observed a higher reversed EOF that remained relatively stable over 40 min.[13] In contrast, Theodoly *et al*. applied pressure-driven flow (PDF) through a CTAB-coated microchannel and observed an exponential decay in zeta potential (directly proportional to the EOF mobility) to the bare glass value in around 10 min.[27] These discrepancies in the EOF decay timescales during CTAB desorption likely stem from the differences in transport (electrokinetic vs. pressure, flow velocity, surface-area-to-volume ratio) and solution composition (pH, ionic strength), demonstrating a need for more comprehensive studies.

For a surfactant in a CE system, the net charge of the surfactant aggregates and the capillary surfaces both contribute to the net velocity. For instance, if an electric field is applied across a capillary containing a cationic surfactant (e.g., CTAB), the surfactant experiences a net transport velocity along the capillary that depends on the EOF and EP mobilities (Figure 1). If the capillary has uniform zeta potential and no pressure gradient, the net velocity of CTA^+ is approximated by the sum of the electroosmotic velocity (U_{EOF}) and the electrophoretic velocity (U_{EP}),

$$U_{\mathrm{Net}} = -\zeta\frac{\epsilon E}{\eta} + \mu_{\mathrm{EP}}E \qquad (1),$$

where ζ is the wall zeta potential, E is the electric field, ϵ is the total permittivity, η is the viscosity, and μ_{EP} is the electrophoretic mobility of CTA^+. As zeta potential increases with CTA^+ surface coverage, one can use zeta potential as a proxy to monitor the reaction, which often controls the surfactant transport in capillaries and microchannels.[13,26,27]

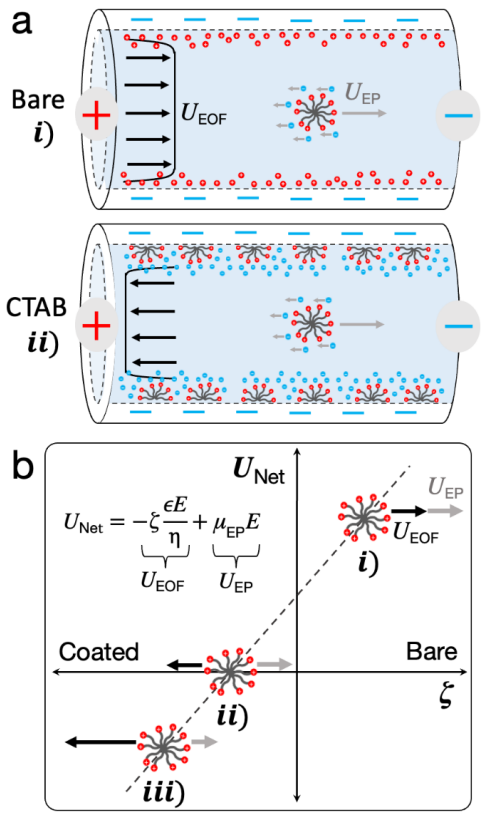

Figure 1. a) Schematic of the electrokinetic transport of CTAB, a cationic surfactant, within a silica microcapillary. Adsorption of CTA^+ inverts the net surface charge (*i-ii*), which causes the electroosmotic flow velocity (U_{EOF}) to oppose the electrophoretic velocity (U_{EP}) of CTA^+. b) Predicted influence of the wall zeta potential (ζ) on the net velocity of CTA^+ (U_{Net}), defined as the sum of U_{EOF} and U_{EP} (eq 1). *i*) For a bare capillary, U_{EOF} and U_{EP} drive CTA^+ toward the cathode. *ii*) As CTA^+ adsorbs to the wall and increases ζ, U_{Net} decreases and is nearly zero at a particular positive ζ, forcing CTA^+ into a stagnant regime governed mostly by diffusion. *iii*) Diffusion and variation in U_{EOF} or U_{EP} allow for slight transport and adsorption of CTA^+, which increases ζ and inverts U_{Net} to drive CTA^+ toward the anode.

In Figure 1, we illustrate the effects of CTA^+ adsorption on the net transport within a capillary. The fixed positive charge of CTA^+ drives its migration toward the cathode under

the applied electric field. This EP mobility changes in magnitude with the aggregation state (e.g., monomers vs. micelles) of CTA^+, which is determined by concentration relative to the cmc.[91] The direction of EOF inside the capillary is dictated by the net surface charge density;[92] for a negative surface (e.g., bare silica, case *i*), EOF moves fluid toward the cathode in an electric field due to the EP migration of cationic space charge in the EDL which screens the negative surface charge. If the surface charge changes from negative to positive (e.g., due to adsorption of CTAB, cases *ii*-*iii*), then EOF will instead drive fluid toward the anode, in the opposite direction as the EP movement of CTA^+, leading to a competition between EOF and EP.

As EOF changes with the surface coverage of CTA^+, the net transport of CTA^+ will also vary throughout the reactions and impact the overall kinetics. For instance, the net electrokinetic transport of CTA^+ will be nearly zero around the positive zeta potential at which the EOF velocity is equal and opposite to the EP velocity (case *ii*). In this low-transport regime, which we call the "stagnant regime", the rate of adsorption will decrease significantly as the reactant within the capillary can only be replenished via diffusion, pressure gradients, or local variations in U_{EOF} or U_{EP}. We expect the stagnant regime will increase in duration with increasing surface-area-to-volume ratio (i.e., decreasing capillary diameter), where adsorption can deplete the reactant concentration faster than electrokinetic transport can replenish it. Moreover, we also predict that hydrophobic interactions of this 19-carbon surfactant will increase the rate of adsorption over desorption and that electrostatic attraction of the positive head group to increase the rate of adsorption at more negative zeta potentials.

In this work, we utilize an automated current-monitoring-based technique for measuring zeta potential known as AZA.[93] We adapted AZA to study CTA^+ adsorption and desorption kinetics in microcapillaries under different transport conditions including diameter, length, voltage alternation pattern and frequency, and applied pressure. Additionally, we constructed a numerical model to compare with our experimental observations.

1. Experimental

1.1. Materials

Hexadecyltrimethylammonium bromide (CTAB) was purchased from Sigma. Monosodium phosphate, disodium phosphate, sodium hydroxide, and sodium chloride were acquired from Fisher. Polyimide-coated fused silica capillaries (365 μm o.d.) were purchased from Molex with inner diameters (*ID*) of 1.2 μm, 4.6 μm, 9.8 μm, or 39.5 μm.

1.2. Solution Preparation

1× PBS (pH 7.1) was prepared by dissolving 150 mM NaCl, 13.33 mM disodium phosphate, and 6.67 mM monosodium phosphate in deionized water (DI) with a measured resistance of 18.0 MΩ-cm. 1× PBS was diluted with 10 vol% DI water to create 0.9× PBS. Solutions were filtered through a 0.4 μm filter before use. pH was measured using an Orion Star™ pH probe (8115BNUWP) and meter (A214), calibrated daily. Conductivity was measured with an Oakton® CON 2700 meter, calibrated daily.

1.3. Capillary–Reservoir Assembly

Capillaries were cleaved to the desired length (8 or 24 mm), measured using digital calipers, then the ends were cleaned with pressurized nitrogen. Capillaries were sealed between PEEK reservoirs using a PDMS O-ring (see Supporting Information). For all zeta

potential experiments, the source and ground reservoirs were filled with 1.5 mL of 0.9×/1× PBS solution. Stir bars and electrodes were added to the reservoirs, then electrical tape was used to cover the reservoirs and screws. The assembly was placed on a stir plate set to 300 rpm.

1.4. Electrical Setup

A Tektronix® Keithley 6517a electrometer was used to apply the constant or alternating DC potential and measure current. All instrument parameters, including the voltage cycles (i.e., the time at a given polarity), were controlled by our MATLAB® algorithm, detailed previously.[93]

1.5. Capillary Conditioning

Reservoirs were sequentially filled with the following solutions using a 10 kV/m electric field for the specified time: 1) 0.1M NaOH for 15 min), 2) DI water for 5 min, then 3) 1× PBS for 5 min. The measured currents were compared to the Ohmic current ($I = \sigma EA$, σ: solution conductivity, A: cross-sectional area of capillary). If the current was more than 10% lower than the predicted value, indicating a possible blockage, then the electric field was applied for additional time until the current increased, or the capillary was discarded and replaced with a new one. If the current was more than 10% higher than the predicted value, indicating a possible leakage, then the capillary–reservoirs were disassembled, dried, and reassembled using a new O-ring. For the 39.5 μm-diameter capillaries, solution could be flushed through the capillary by positioning the tip of a 1 mL pipette around the inlet.

1.6. Zeta Potential Analysis Algorithms

The following algorithms were used to transport CTA^+ through the capillary and/or monitor zeta potential.

1.6.1. AZA

This method, used to analyze zeta potential at high frequencies, was detailed previously.[93] The specific parameters used in this work are as follows. The algorithm alternates the polarity of the electric field (30 kV/m) after: a) detecting a fluid traversal endpoint (with a plateau delay time of 5 s), or b) reaching the max cycle time of 60 sec. An endpoint is found if the slope of current vs. time (moving average across 3 points) drops below the threshold slope, equal to one-third times the slope 2 s prior. After detecting an endpoint, zeta potential is calculated and placed halfway between the start and end time. If the slope changes sign in a given cycle, a 0-mV zeta potential is marked at the time of inflection (Figure S2).

1.6.2. AZA–DC (8 mm lengths)

AZA is applied for 2 min (or until a cycle is complete), then a positive polarity field is applied for 3 min; this process repeats in perpetuity.

1.6.3. AZA–DC (24 mm lengths)

Since traversal time is proportional to capillary length for a given electric field strength, the time parameters used in AZA–DC for 8 mm lengths (~2 min of AZA, 3 min of DC, 5 sec plateau time, 60 sec max cycle time) are multiplied by 3.

1.6.4. AC 45s

The voltage polarity is continuously alternated at 45 s intervals.

1.6.5. AZA ± PDF

500 μL of solution is removed from the source reservoir (resulting in a 2 mm height difference between reservoirs) to induce a pressure of approximately 19.6 Pa. This pressure was confirmed by measuring around a 10-mV difference in zeta potential values between consecutive cycles using AZA.

1.6.6. AZA 1CV/3CV

AZA is applied with a 3 min max cycle time and variable plateau time determined at each endpoint to maintain the net column volumes (CVs) of CTA^+ per cycle. The plateau time uses the net velocity (EOF + EP) and capillary length. EP velocity is calculated using a mobility equivalent to +30 mV or +15 mV in adsorption or desorption.

1.7. CTAB Adsorption–Desorption Experiments

The source and ground reservoirs were filled with 0.9×/1× PBS, and zeta potential was measured using AZA–DC for 60 min. After zeta potential was relatively stable (±2 mV over 10 min), a 10-min average zeta potential was calculated and compared to the typical range around –30 ± 3 mV. This average zeta potential of the bare capillary was used as the initial value (t = 0 s) in adsorption experiments. In adsorption, a volume of CTAB solution (20 mM in 1× PBS) was added to achieve a final concentration of 0.26 mM CTAB in each reservoir, and the respective voltage pattern and stirring were initiated. At the end of adsorption, the voltage pattern was terminated and the reservoirs were emptied and dried. In desorption, reservoirs were filled with 0.9×/1× PBS without CTAB, and the voltage pattern and stirring were initiated. At the end of desorption, the pH levels of both reservoirs were measured to confirm the pH did not change significantly (7.1 ± 0.2) over the course of the experiment.

Then, the reservoirs were replaced with new solutions, and the same voltage pattern was initiated to obtain a final, 10-min average zeta potential reading.

1.8. Numerical Simulations

Using COMSOL Multiphysics®, we constructed a numerical model that includes electromigration, diffusion, advection, and surface reactions of relevant species in our system. We coupled the advective transport of these species to the local surface concentration of CTA^+, which adsorbs to the surface from the bulk solution through a reversible first-order reaction and thereby determines the wall zeta potential. For more details on the numerical methodology, see Supporting Information.

1.9. Calculation of Net CTA^+ CVs per Cycle

The net transport of CTA^+ was calculated by summing the EOF and EP transport in: $\mathrm{CTA^+\ CVs/Cycle} = \frac{t_{\mathrm{cycle}}}{L}\left(\left|-\frac{\epsilon E}{2\eta}\zeta + \mu_{\mathrm{EP}}E\right|\right)$ where t_{cycle} is voltage cycle time, L is capillary length, E = 30 kV/m, ϵ = 78.4 ϵ_0, η = 8.9 × 10^{-4} Pa-s, and μ_{EP} = 0.234 cm^2/kV·s in adsorption or 0.169 cm^2/kV·s in desorption. For AZA, t_{cycle} was the smaller quantity of either the fluid traversal time $\left(t_{\mathrm{fluid}} = \frac{\eta \mathrm{L}}{\epsilon E \zeta}\right)$ plus the plateau time (5 s) or the max cycle time (60 s). For AZA ± PDF, the CVs per cycle was calculated by averaging the transport in each flow direction, which was calculated by adding or subtracting 5 mV from ζ, which affects both the EOF velocity and AZA cycle time. For AC 30s–DC, the time-weighted-average cycle time was used, equivalent to 120 s.

2. Results and Discussion

2.1. Multiphasic Adsorption and Desorption of CTAB in CE Conditions

In Figure 2, we present a characteristic result of multiphasic behavior during CTAB adsorption and desorption in our capillary electrokinetic conditions. While the constant DC electric field used in CE is not compatible with AZA, which uses an alternating electric field, we employ a combined approach wherein we successively switch between periods of AZA and DC in a 2-to-3 time ratio (AZA–DC, Section 1.6). In Figure 2, we show the zeta potential kinetics measured for two capillaries during CTAB adsorption and desorption (Section 1.7).

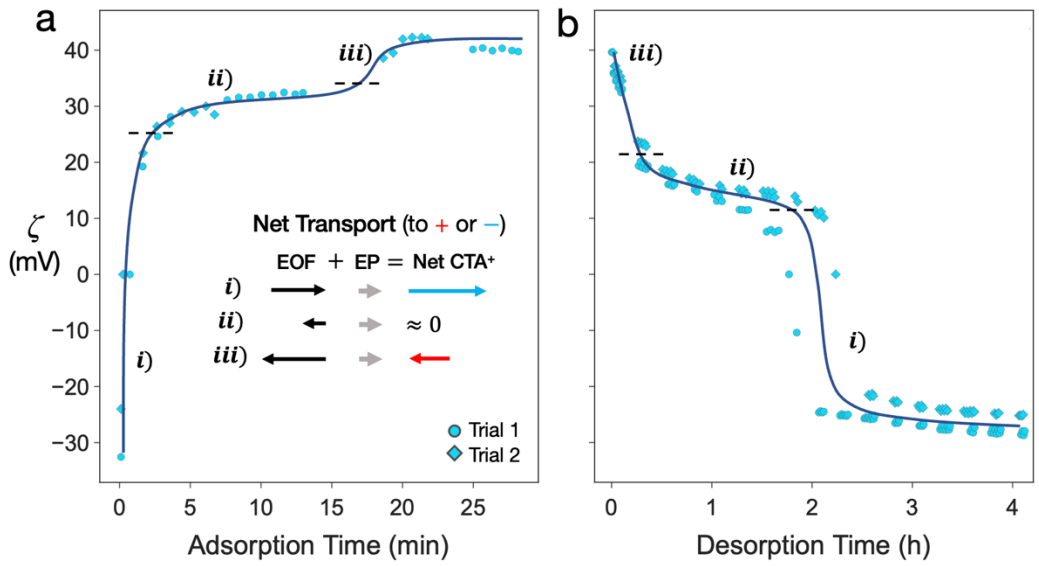

Figure 2. Zeta potential kinetics in 0.9×/1× PBS during 0.26 mM CTAB (a) adsorption and (b) desorption. Phases (*i*)–(*iii*) indicate the predicted net transport of CTA^+. *ID*: 39.5 µm; *L* = 24 mm; *E* = ±30 kV/m; Algorithm: AZA–DC. Solid lines are included to guide the eye.

In adsorption (Figure 2a), the wall zeta potential initially climbed rapidly from the bare value of –32 mV to around +25 mV, where the rate of increase slowed significantly. We attribute the rapid increase in (*i*) to relatively fast transport and adsorption of CTA^+; for negative zeta potentials, EOF and EP both drive CTA^+ toward the anode, causing the net transport rate of CTA^+ to exceed that of the fluid. Further, the negatively charged, hydrophobic surface favors adsorption of CTA^+. Based on the first-order kinetics at planar surfaces,[27] the rates of the forward (adsorption) and reverse (desorption) reactions depend on the difference in CTA^+ concentration from surface-to-bulk, which is largest at the start of the reaction. In the second phase of adsorption (*ii*), from about +25-35 mV, we attribute the significant decrease in slope to reduced transport within the stagnant regime (Figure 1). The zeta potential range of (*ii*) was centered around the EP mobility of CTAB in water, 0.24 $cm^2/kV \cdot s$ (equivalent to +31.75 mV zeta potential).[91,94] We assert that diffusion and heterogeneities in concentration, which affect the EP mobility of CTA^+ (Figure S3a),[91] ultimately enabled the reaction to break out of this transport-limited regime. In the final phase of adsorption (*iii*), the growth rate accelerated as the transport rate recovered, and zeta potential reached a steady state around +40 mV. The final plateau shows that the adsorption rate decreases significantly as the surface concentration approaches the equilibrium value, balancing the dynamic adsorption and desorption processes.

In desorption, we observed similar behavior with three distinct regimes, but with two key differences. First, we observed a 6-fold longer time to approach the final equilibrium than in adsorption, which we attribute to the hydrophobic forces that stabilize CTA^+ on the silica surface.[27,95,96] Second, the zeta potential range of the stagnant regime (*ii*) occurred at roughly half that observed in adsorption (approximately +8-17 mV vs. +25-35 mV); we attribute this

difference to the concentration and thus, aggregation state of CTAB—that is, micelles or monomers. In adsorption, we expect the concentration of 0.26 mM exceeded the cmc of approximately 0.15 mM in our conditions (Figure S3a and Lucy and Underhill[97]); therefore, we anticipate that CTAB predominantly existed in the form of micelles which directly adsorbed to the surface. In desorption, with 0 mM CTAB in the supplying reservoirs, surface-bound micelles could have detached and reassembled into monomers, which have a lower mobility than micelles.[89] In contrast to our results, other studies show monophasic decays and varying timescales of CTA^+ desorption from silica microchannel or capillary surfaces (Figure S4).[13,26,27] We believe these different behaviors are due to the specific transport condition used in each study (e.g., CTAB concentration, channel length, net CTA^+ velocity due to electric field or pressure). For slower reactions or faster transport conditions, the kinetics could elucidate the reaction mechanism and/or the structure of the coating (e.g., bilayer degradation in two phases).[28,96] In our previous study of aminosilane coating dynamics in capillaries, the reactions were significantly slower than transport; thus, we observed kinetic differences between monomer types and fluid conditions which supported the mechanisms of silane activation and covalent bond formation or hydrolysis.[93]

2.2. Influence of the Capillary Surface Area-to-Volume Ratio

The high surface-area-to-volume ratios in microchannels and capillaries can amplify concentration changes in the bulk during surface reactions. In Figures 3a-b, we demonstrate this effect by measuring the zeta potential response during CTAB adsorption and desorption in 8 mm-long capillaries of varying diameter while applying AZA–DC. In Figures 3c-d, we show simulated responses of the varying diameter capillaries under a DC bias (Section 1.8).

While AZA–DC was difficult to simulate due to the complexity of the cycling algorithm and slower kinetics (i.e., long computation timescales), the DC simulations show the predicted responses in CE conditions that are not measurable using AZA.

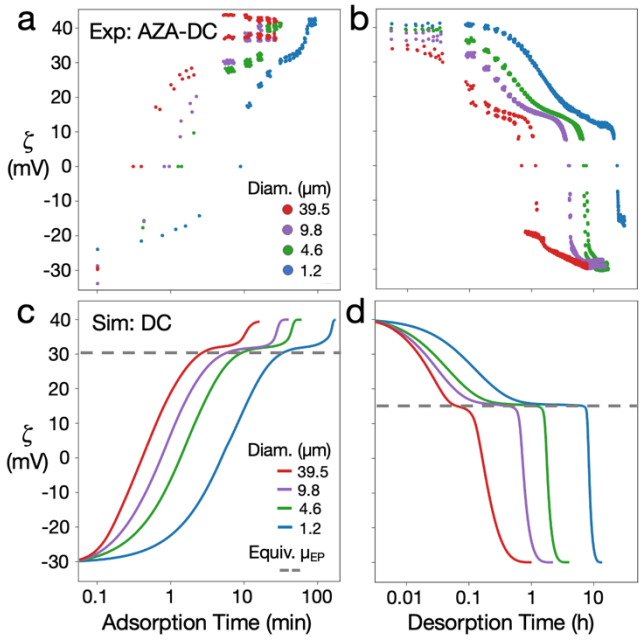

Figure 3. Effect of capillary diameter on zeta potential kinetics in 0.9×/1× PBS during 0.26 mM CTAB (a) adsorption and (b) desorption. L = 8 mm; E = ±30 kV/m; Algorithm: AZA–DC. (c–d) Simulated adsorption and desorption kinetics under a DC bias (Section 1.8).

For the measured responses in varying diameters (Figures 3a-b), we focus our discussion on the stagnant regime and overall reaction times. First, we observed that the zeta potential ranges of the stagnant regime during adsorption and desorption were almost identical to those in Figure 2. Second, we found that the overall reaction times and durations of the stagnant regime increased with decreasing diameter. We suspect that the surface reactions significantly altered the bulk CTA^+ concentration along the capillary in smaller diameters

with larger surface-area-to-volume ratios. These bulk depletion or saturation events during adsorption and desorption, respectively, hindered the reaction kinetics and generated boundary layers (i.e., CTA^+ concentration gradients from the capillary inlets to the center) due to the oscillating transport and fast reaction kinetics relative to transport (Figure S6). Within these boundary layers, the concentration of CTA^+ can differ appreciably from that in the reservoirs; therefore, reaching final equilibrium requires the boundary layers to be replenished through increased transport along the capillary. Since the boundary layers are exacerbated when the net transport is reduced, the smaller capillaries showed a longer time to break out of the stagnant regime. We study the effect of controlling the net CTA^+ transport per voltage cycle in Section 2.3.

We further investigated the effects of capillary diameter using numerical simulation and by recasting the zeta potential kinetics in terms of net CTA^+ transport volume normalized by surface area. While the simulations used a DC bias, the overall shape and trends of the zeta potential responses exhibited excellent qualitative agreement with the AZA–DC experiments (Figures 3c-d). The simulated adsorption kinetics were slower than the experimental results whereas the desorption kinetics were faster; this trend shows the hydrophobic stability of the CTAB coating, which was not included in our simulations. After normalizing the measured zeta potential responses by the net EP+EOF transport and the capillary surface-area-to-volume, the varying diameter curves collapsed and became linear during the stagnant regime (Figure S5). The linear relationship with net transport further demonstrates that the multiphasic kinetics and differences between the diameters are due to the confinement and transport conditions.

2.3. Net CTA^+ Transport: Effects of Alternating EOF/EP and Pressure

We further examined the effect of CTA^+ boundary layers, which prolonged the stagnant regime in smaller diameter capillaries, by varying the alternating electrokinetic and/or pressure-driven transport during CTAB adsorption and desorption in Figure 4. In general, we observed significant differences in the duration of the stagnant regime and final equilibrium time across the varying transport conditions. As we increased the voltage alternation frequency, we observed slower kinetics, which we attribute to a smaller oscillatory transport amplitude of CTA^+ along the capillary. We also saw different zeta potential values at the onset and breakout of the stagnant regime, which we examine in more detail in Figure 5 by calculating the net transport per voltage cycle vs. zeta potential for the different processes. In Figure 4a, we show adsorption in 4.6 μm diameter capillaries where the high surface-area-to-volume enhanced the contrast between different transport conditions. In Figures 4b-c, we show desorption in 39.5 μm diameter capillaries where the larger cross-sectional area allowed us to investigate the effect of pressure using a small head-height difference between the reservoir solutions.

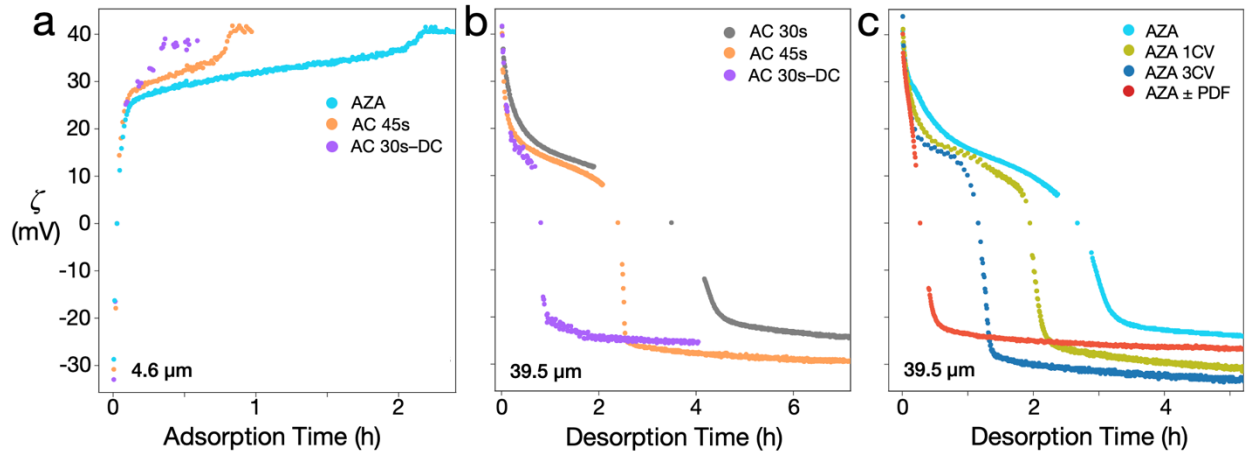

Figure 4. Effect of AZA algorithm and pressure on zeta potential kinetics in 0.9×/1× PBS during 0.26 mM CTAB (a) adsorption and (b,c) desorption. *ID*: (a) 4.6 µm or (b-c) 39.5 µm. *L* = 8 mm, *E* = ±30 kV/m.

In Figures 4a and 4b, we show that the duration of the stagnant regime and the overall kinetics are proportional to the voltage alternation frequency. As we decreased the cycle time from 120 s (i.e., time-weighted-average for AC 30s–DC) to 45 s (AC 45s), the time to approach the final equilibriums in adsorption (i.e., +37 mV) and desorption (i.e., –20 mV) increased 2.5-fold and 2.8-fold, respectively; these magnitudes of increase are consistent with the 2.7-fold shorter average cycle times in AC 45s. Similarly, as we increased the cycle time 1.5-fold in desorption (AC 30s to AC 45s), the time to approach the final equilibrium decreased 1.8-fold. We also observed that the final equilibrium was 2.7-fold slower in AZA vs. AC 45s, which is likely due to the shorter cycle times within the stagnant regime. The order and relative kinetic spacing between these voltage patterns were confirmed by our simulations (Figure S7), which also included responses in DC and pressure-driven conditions.

In Figure 4c, we compare the desorption kinetics for AZA with two conditions where we maintained the net transport CVs of CTA^+ per voltage cycle (AZA 1CV or 3CV) and one where we added a head-induced pressure flow equivalent to 5 mV zeta potential (AZA ± PDF, see Section 1.6). Compared to AZA, AZA 1CV showed a 1.7-fold faster time to approach the stagnant regime (i.e., +17 mV) and 1.5-fold faster time to approach the final equilibrium. Compared to AZA 1CV, AZA 3CV exhibited a 2-fold faster time to approach the stagnant regime and a 1.6-fold faster time to approach the final equilibrium. Finally, AZA ± PDF showed a rapid decay in zeta potential with no stagnant regime, similar to the aforementioned study by Theodoly et al.[13] This behavior demonstrates that applying a relatively small pressure difference (< 20 Pa or 2 mm between reservoirs) completely eliminates the stagnant regime. Overall, these comparisons demonstrate that augmenting the net transport before and/or during the stagnant regime can shorten the stagnant regime and thereby accelerate the overall kinetics.

In Figure 5, we examine the predicted net CTA^+ transport for the conditions shown in Figure 4 to explain the observed differences in the onset and breakout magnitudes and the durations of the stagnant regimes. We expect that as zeta potential approached the EP mobility, equivalent to approximately +30 mV in adsorption and +15 mV in desorption, the relative kinetics were governed by the number of net CTA^+ column volumes (CVs) per cycle. In general, we provide evidence that the stagnant regime appeared at zeta potentials where the net transport of CTA^+ was below 1 CV per cycle.

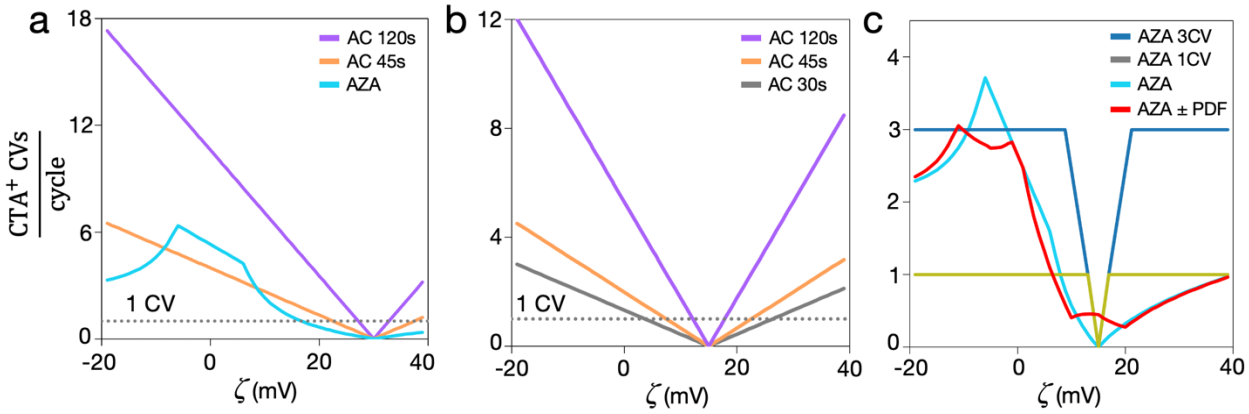

Figure 5. Influence of AZA algorithm and pressure on the estimated net column volumes (CVs) of CTA^+ per voltage cycle. The conditions in (a–c) directly correspond to those in Figure 4. The average responses shown for AC 120s (i.e., time-weighted average of AC 30s–DC) and AZA ± PDF incorporate the possible cycle times and net velocities in either flow direction at a given zeta potential (Section 1.9). For AZA 3CV and AZA 1CV (c), the decrease around the stagnant regime is due to a max cycle time of 3 min; for AZA (a,c), the linear response around 0 mV is due to a max cycle time of 60 s.

We interpret the net transport curves in Figure 5 to explain kinetic observations in Figure 4. For AZA in Figure 4a, the zeta potential range of the stagnant regime was much broader than the other voltage patterns; this wider range is because the net transport per cycle decays exponentially rather than linearly from +8 to 30 mV (Figure 5a), prolonging the range in which the net transport is below 1 CV per cycle. The zeta potential at the onset of the stagnant regime in Figure 4 was usually when the net transport was below 1 CV per cycle, which occurs around +25 mV for AZA, +28 mV for AC 45s, or near +30 mV for AC–DC. This trend further supports the influence of boundary layers impeding the reaction kinetics; as the oscillatory penetration depth of CTA^+ drops below 1 CV, the reactant is no longer replenished along the entire capillary length and the reaction rate decreases considerably,

especially near the middle of the capillary (Figure S6). For the transport-controlled cases, AZA 1CV and AZA 3CV, the enhanced initial and final reaction kinetics compared to AZA were likely due to the greater CTA^+ transport from +8-40 mV (Figure 5c). Additionally, AZA 3CV showed a narrower zeta potential range for the stagnant regime, and the breakout was around 5 mV higher than that of AZA 1CV or AZA. Since the EP mobility of CTA^+ increases with the concentration range we expect for desorption (Figure S3a), the narrower zeta potential range and higher breakout magnitude for AZA 3CV likely stem from the larger penetration depth and more uniform concentration of CTA^+ along the capillary. Overall, the occurrence of the stagnant regime at zeta potentials where the net transport is less than 1 CV per cycle further demonstrates the importance the net surfactant transport and concentration boundary layers on the kinetics in CE conditions.

3. Conclusions

Several studies report different desorption behaviors for surfactant coatings in confined microchannels compared to the first-order kinetics typically observed at planar, open interfaces.[13,26,27,96] These differences likely originate from the transport limitations in electrokinetic microfluidics; however, more comprehensive studies are needed to fully elucidate the effects of transport in CE-relevant conditions. In this work, we use the high frequency platform, AZA, to extract zeta potential kinetics during CTAB adsorption and desorption in a silica microcapillary while precisely controlling the transport phenomena (e.g., EP and EOF, pressure). A previous study shows monophasic EOF decay kinetics during CTAB desorption that are proportional to the total flushed capillary volumes of fluid;[28] by contrast, using AZA, we observed novel multiphasic kinetics characterized by an

intermediate quasi-steady state which we term the "stagnant regime." As the nature of these kinetics could easily be confused for higher order chemistry (e.g., cooperative bilayer desorption), we investigated the influence of key transport effects such as the surface-area-to-volume ratio (i.e., capillary diameter), voltage waveform, and pressure in greater detail.

We showed that the stagnant regime was induced by a reduction in the net transport of CTA^+ when the EOF mobility (i.e., zeta potential) directly opposed the EP mobility of CTA^+ at certain positive surface zeta potentials. We observed that the timescales of the stagnant regime and final equilibrium were proportional to the capillary diameter and net CTA^+ transport; further, the net transport was governed by the AZA measurement algorithm and the progression of the reaction. Our experimental and numerical results evidenced considerable variation in the local concentration of CTA^+ along the capillary length during the periods of restricted transport, which affected the EP mobility and thus the zeta potential magnitude of the stagnant regime. These heterogeneities in concentration and mobility were exacerbated when the net CTA^+ transport fell below 1 column volume per voltage cycle, thereby hindering the replenishment of axial boundary layers and reducing the reaction rate. This effect was more significant as both the surface-area-to-volume ratio and the voltage alternation frequency increased.

In summary, cationic surfactants are more efficiently deposited and removed when the net transport of surfactant is sufficiently high. The use of a directional pressure gradient can greatly increase the overall reaction kinetics by enhancing transport during the stagnant regime under electrokinetic conditions. For smaller diameter capillaries, which often require complex instrumentation to apply pressure-driven flow, one can leverage DC or hybrid AC–DC transport to accelerate the kinetics; on the contrary, if more stable EOF is desired, high

frequency AC or AZA are effective at prolonging the stagnant regime and thus, the reaction kinetics. This detailed study highlights the important factors influencing the dynamics of cationic surfactant coatings in electrokinetic and/or pressure-driven microfluidics. We believe similar transport-oriented approaches will significantly aid in the optimization of coating conditions and EOF stability for improved separation efficiency and resolution in CE.

III. Catalyzed Degradation of Semi-Permanent Capillary Coatings

Introduction

Semi-permanent coatings (e.g., double-chained surfactants or DCS, successive multiple ionic layers or SMIL) are more commonly used in CE than dynamic coatings for a greater EOF stability, allowing a higher number of consecutive runs without regenerating the coating or storing the coating species in the run buffer.[8,98–100] However, recent studies show the rapid degradation of such coatings in aqueous conditions of pH 7 and higher.[24] The addition of the anionic surfactant, SDS, was also shown effective at removing pre-adsorbed DCS layers if using a concentration above the cmc.[101] Some studies characterized the equilibrium aggregation of DCS in various solution and surface conditions,[28,86,102–104] however, the kinetics of these dynamic processes (e.g., phase transitions, adsorption-desorption) were not studied due to low temporal resolutions of the applied measurement techniques. Since neutral and alkaline conditions are used in CE separations of basic proteins, understanding the unclear mechanisms of these instabilities would allow a broader application of such coatings.

We present AZA for extracting the kinetic mechanisms of DCS coating degradation. First, we monitored the EOF stability of surfactant coatings that varied in chain length after exposure to similar conditions of a previous study;[24] our initial comparisons showed a wide variation in the coated zeta potential and decay kinetics for the different monomers. Next, we aimed to increase the final reversed EOF magnitude (i.e., coating density) by varying the coating solution for increased solubility. To better elucidate the high instability of DCS coatings in neutral and basic pH,[24] we investigated the influence of the buffer type (i.e., valency) on the measured EOF stability at the same or different pH. We also monitored the

removal of DCS coatings by SDS, similar to the previous qualitative study,[101] however, we provide higher temporal resolution at different SDS concentrations.

1. Methods

1.1. Materials

Didodecyldimethylammonium bromide, 98%, (DDAB) was purchased from Alfa Aeser. Dihexadecyldimethylammonium bromide, 97%, (DHDAB), dioctadecyldimethylammonium bromide, 98%, (DODAB), sodium acetate anhydrous, (4-(2-hydroxyethyl)-1-piperazineethanesulfonic acid) (HEPES), and sodium phosphate monobasic monohydrate were acquired from MilliporeSigma. Tris(hydroxymethyl)aminomethane (Tris), sodium chloride, and sodium phosphate dibasic heptahydrate were purchased from Fisher Scientific. Fused silica polyimide coated capillary tubing (50 μm i.d., 365 μm o.d.) was purchased from MicroSolv Technology Corporation.

1.2. Solution Preparation

Solutions were prepared using MilliQ deionized (DI) water (18.0 MΩ) and filtered using 0.4 μm filters before use. pH was measured using an OrionStar pH probe (Chapter II) and titrated via addition of 36% HCl or 6M NaOH. Conductivity was measured using an Oakton meter (Chapter II) and titrated via addition of 6M NaCl or DI water. The following solutions were prepared: 13 mM sodium phosphate (pH 7.29, σ: 1.956 mS/cm, 2:1 dibasic/monobasic), 22.4 mM sodium phosphate (pH 3.44, σ: 1.924 mS/cm, monobasic), 23.2 mM sodium acetate (pH 5.46, σ: 1.89 mS/cm), 14.7 mM Tris + sodium chloride (pH 7.25, σ: 1.92 mS/cm), 15.5 mM HEPES + sodium chloride (pH 7.33, σ: 1.94 mS/cm).

1.3. Coating Formation and Exposure

Capillaries were cleaved to 8 mm length (Chapter II) and modified with surfactants using the procedure outlined by Shulman et al.,[24] with the following exceptions. As we used a capillary–reservoir assembly (Appendix B) which was open to air and not amenable to the high-pressure rinsing steps (NaOH, water, 0.1mM surfactant rinses), these steps were replaced with a head-induced pressure flow (1 mL in anodic reservoir, 2 mL in cathodic reservoir, ~4 mm head-height difference) and applying a +10 kV/m electric field. After coating for 15 min, the capillaries were exposed to 0.9X/1X concentrations of the indicated buffer solution in the respective anodic/cathodic reservoirs, with an alternating electric field of ±62.5 kV/m (10 min alternating polarity intervals). Our modified procedure based on that of Shulman et al,[24] allowing the extraction of zeta potential every 10 min; however, the capillary was not rinsed between EOF measurements.

2. Results and Discussion

2.1. Stability of Double-Chained Surfactants of Varying Chain Length

We first applied AZA to monitor the stability of double-chained surfactants of varying alkyl length (C_{12}–DDAB, C_{16}–DHDAB, and C_{18}–DODAB) in buffered conditions similar to those in Shulman et al.[24] In Figure 1, preconditioned capillaries were coated with 0.1 mM surfactant in DI water then exposed to pH 3.5 phosphate solution (Sections 1.2-1.3).

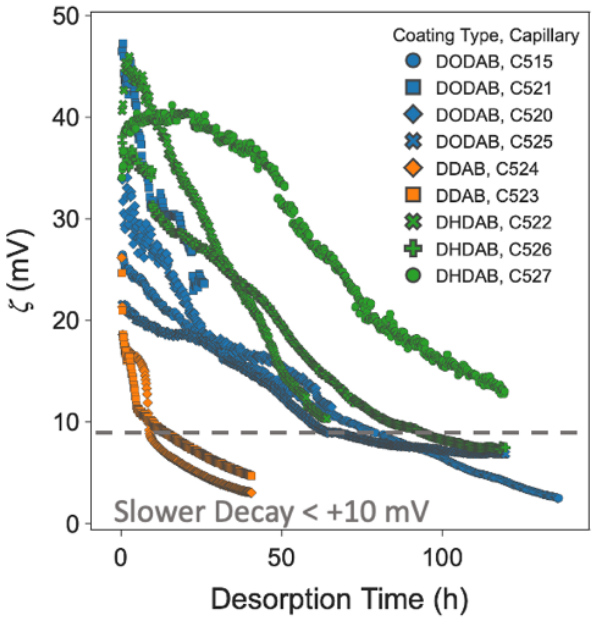

Figure 1. Zeta potential stability of capillaries coated with surfactants of varying alkyl length (0.1 mM in DI) and exposed to pH 3.5 phosphate buffer. *ID*: 50.0 µm, *L*: 8.0 mm, *σ*: 1.92 mS/cm, *E*: ± 62.5 kV/m (10 min).

The density and uniformity of the surfactant coatings were inferred from the first zeta potential values after 10 min. In pH 3.5 phosphate solution, the initial zeta potential reading (at 10 min) varied between replicate coating experiments for each surfactant in DI water. This initial zeta potential varied from +22-48 mV for DODAB, the surfactant which had the longest alkyl chain, while the shorter-chain surfactant coatings had more repeatable zeta potentials (+34-41 mV for DHDAB, +25-27 mV for DDAB). This higher variance observed for DODAB may be due to a lower solubility in water, which could induce a more non-uniform concentration affecting the density and homogeneity of the final coating. As DHDAB and DDAB are less hydrophobic, their higher solubility in water should allow for a more uniform concentration during coating formation.

Coating stability was inferred by the relative decay in zeta potential over time in the alternating electric field and pH 3.5 conditions. While zeta potential was initially higher for DHDAB vs. DODAB, the relative slopes of decay were roughly the same and a significant reduction in slope was observed around +10 mV zeta potential (64-75 h). The overall similar decay rates show the coating stabilities are similar, while the slower final decay indicates that small quantities of surfactant on the surface difficult to remove. In contrast to the longer chain surfactants, DDAB exhibited a faster decay rate and approached a +10 mV zeta potential value in less than 7 h. This lower stability is likely due to the shorter alkyl length and lower hydrophobicity inducing a higher critical surface aggregation concentration (csac).

2.2. Stability of DODAB in Varying Buffer and/or pH

While the stability of DODAB has been shown to depend heavily on solution pH in phosphate solutions, the mechanism for the rapid decay under neutral and alkaline conditions is unknown.[24] In high pH, quaternary amine have been shown to undergo oxidation to form a tertiary amine, and this reaction can be accelerated in the presence of silica.[98] As the rapid reaction kinetics were poorly resolved in CE conditions and only one buffer type was tested,[24] we use AZA to extract higher temporal resolutions in a wider range of exposure conditions.

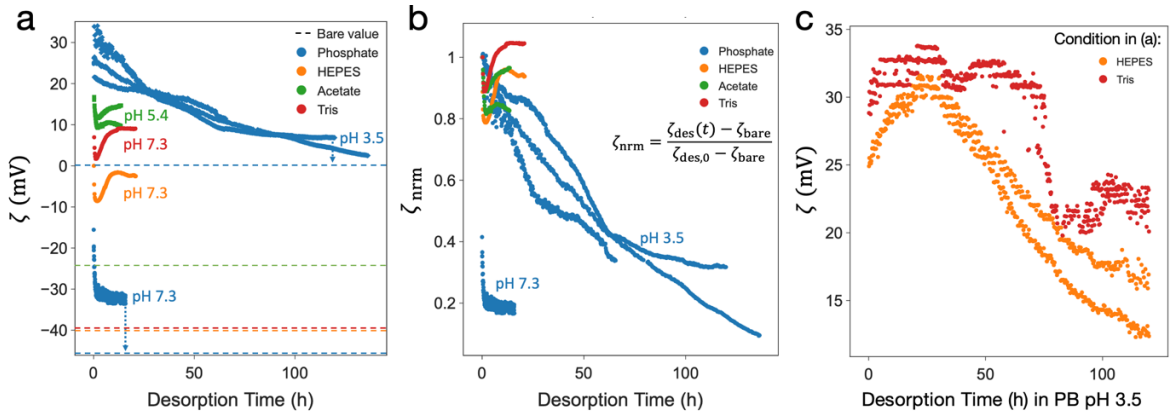

Figure 2. a) Zeta potential stability of capillaries coated with DODAB (0.1 mM in DI) then directly exposed to solutions of different buffer and/or pH. b) Zeta potential kinetics from a) normalized using the initial ($\zeta_{des,0}$) and bare (ζ_{bare}) zeta potential values. c) Exposure of pre-exposed capillaries in a) to phosphate pH 3.5 solution. *ID*: 50.0 µm, *L*: 8.0 mm, σ: 1.89-1.96 mS/cm, *E*: ± 62.5 kV/m (10 min).

In Figure 2, we study DODAB in conditions similar to Shulman et al.[24] and also other buffers and pH to determine if the instability observed in neutral pH was due to the pH or the buffer valency. Since phosphate the negative charge of phosphate increases with pH, we hypothesized that the higher phosphate valencies (-2 to -3) could catalyze the desorption of DODAB through electrostatic attraction. For the phosphate exposures mimicking the previous study, we used AZA to extract significantly higher temporal resolution over much longer timescales, up to 5 days for pH 3.5 (Figure 2a). Overall the rapid decay kinetics in phosphate pH 7.3 were similar to the reported by Shulman.[24] The final zeta potential, however, was around 15 mV higher than that of the bare capillary, indicating that incomplete removal of the DODAB coating after 19 h. In pH 3.5, the zeta potential decayed to around +2 mV after around 120 h, suggesting complete removal after a much longer timespan.

We also monitored DODAB stability in buffers of varying pH (and possible charge states) to test if the rapid decay observed for pH 7.3 phosphate also occurred for other buffers: Acetate pH 5.4 (-1 to 0), Tris (0 to +1), and HEPES (-1 to 0). By measuring the average equilibrium zeta potential of the bare capillary, we could normalize the zeta potential kinetics to this expected value after complete removal (Figure 2b). While the initial zeta potential differed widely between these buffers, likely due to interaction of the buffer and the DODAB-coated surface, we observed little to no zeta potential decay over 19 h. We attribute the initial fall-and-rise in zeta potential to the exchange of electric double layer ions after exchanging the coating solution for the buffer. To confirm the stability of the coating after exposure to HEPES or Tris buffer, we subsequently exposed the capillaries to pH 3.5 phosphate and monitored zeta potential over 5 days (Figure 2c). In this final exposure condition, the initial zeta potentials were similar to the highest value measured in pH 3.5 phosphate, indicating that no degradation had occurred in the previous 19 h exposures. Over this time, zeta potential followed similar decay kinetics to those in Figure 2a.

2.3. Stability of DODAB in Varying SDS concentrations

DODAB has been shown to degrade via SDS, a negatively charged surfactant, if the concentration is above the critical micellar concentration (cmc).[101] In Figure 3, we studied the effect of SDS on the stability of DODAB extracted using AZA. As phosphate is also a negatively charged additive, the kinetics in Figure 2 can be compared to these SDS results to determine the mechanisms of DODAB removal in the presence of anionic additives.

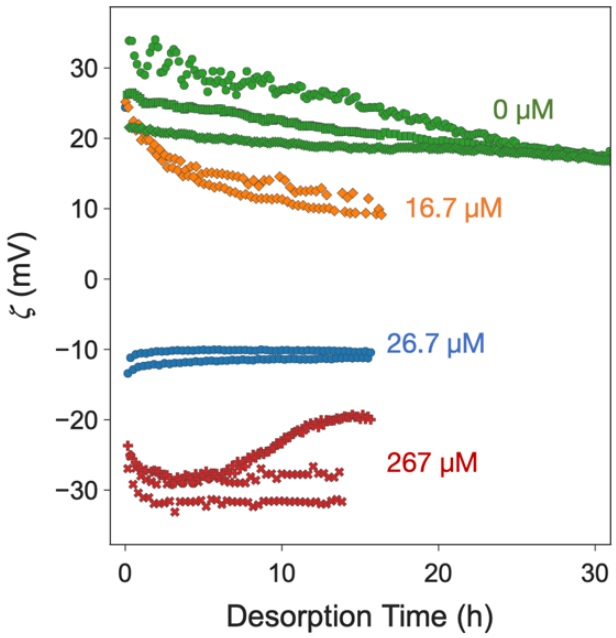

Figure 3. Zeta potential stability of capillaries coated with DODAB (0.1 mM in DI) and exposed to varying SDS concentration in phosphate pH 3.5 solution.

In Figure 3, we added SDS in varying concentration to pH 3.5 phosphate solution and monitored zeta potential decay to infer coating desorption via the SDS micellization above the cmc. Overall, we observed the zeta potential decay increased with increasing SDS concentration, which supports the previous conclusions of Allen et al.[101] In 16.7 µM SDS, we observed that zeta potential initially was the same as that in the control solution (0 µM), and zeta potential gradually decayed from +25 mV to +10 mV over 18 h. The decay behavior appeared first-order exponential, in contrast to the control solution which showed a flatter, linear slope. As the concentration of SDS was increased to 26.7 µM, we observed an immediate jump in zeta potential to -10 mV, which was stable over the 16 h experiment. As we increased the SDS concentration 10-fold (267 µM), zeta potential jumped directly to -23 to -27 mV and gradually declined to around -30 mV in less than 2 h. The highly negative zeta

potential in pH 3.5 phosphate, where the bare capillary value is around 0 mV, shows that SDS forms a negatively charged coating on the capillary surface. After 16 h in 26.7 μM SDS, the solutions were exchanged for pH 3.5 phosphate (no SDS) and zeta potential was measured to be +3 to 3.5 mV, which confirms the nearly complete removal of DODAB in this condition. The lower magnitude, -10 mV zeta potential in 26.7 μM SDS supports a lower density SDS coating at this concentration, which is likely below the cmc.

3. Conclusions

In this preliminary study, we investigated solution factors affecting the stability of DODAB in pH 3.5 to pH 7.3 solutions; previous studies have shown rapid degradation of DODAB in pH 7.3 phosphate buffer and suggest this is due to a silica-catalyzed, alkyl-chain oxidation reaction of unknown mechanism.[24] We used similar conditions to this previous study and observed similar degradation timescales using AZA. Further, we examine other buffers at similar pH, and observed no loss in zeta potential after 16-19 h. These buffer comparisons indicate the rapid degradation of DODAB above pH 7 is due to increasing negative charge phosphate with pH, rather than due to the increasing concentration of hydroxide with pH. We showed complete desorption of DODAB using a different negatively charged additive, SDS, which has been shown to micellize the coating if used above the cmc. Through these different experiments, we propose a different mechanism of DODAB removal by the by phosphate with a -1 to -2 charge around pH 7.2. While more experiments are necessary to confirm this hypothesis, these initial conclusions contradict those of the similar study by Shulman et al.

IV. Conclusion

To investigate the elusive mechanisms of coating degradation in CE conditions, we developed AZA, an automated, high frequency platform for measuring zeta potential in a silica capillary. We demonstrated high spatial and temporal resolution for monitoring fast chemical reactions on inner capillary surfaces by extracting accurate zeta potential responses in different pH solutions. We improved the capillary–reservoir design to maintain the reservoir solution pH and composition over long monitoring timescales in the alternating electric field. After validating the technique and fluidic platform, we applied AZA to monitor coating formation and degradation of aminosilane monomers in aqueous and anhydrous deposition and exposure conditions. We found that the deposition kinetics and final coverage were related to the monomer structure and solvent, while the final stability in aqueous solution was related to the deposition solvent, exposure pH, and alkyl length of the monomer.

To investigate surfactant adsorption and desorption kinetics in different transport conditions, we adapted AZA to provide precise control of the net transport of CTAB, a cationic surfactant, through the capillary as we varied the capillary dimensions, applied electric field, and pressure conditions. We found that the coating stability in aqueous buffer depended on the capillary surface-area-to-volume and the EP mobility of CTA^+, which varied with the concentration of CTAB. Interestingly, we observed intermediate stagnant regimes at zeta potentials where the EOF and EP mobilities directly opposed, induced by the increase or decrease in zeta potential during adsorption or desorption. By varying the alternating electric field frequency and applying pressure-driven flow, we demonstrated control over the duration of the stagnant regime and therefore, the final equilibrium timescale in CE conditions. The novel multiphasic responses observed using AZA were novel, as

previous kinetic studies likely did not monitor the complete reaction and only studied a narrow range of transport and solution conditions. We developed more complex AZA algorithms that modulated the net transport of CTA^+ based on the known EP mobility and the time-dependent EOF mobility during adsorption and desorption. We envision that through the further development of AZA, a wider range of surfactants may be studied in detail to improve coating stability and thus, separation efficiencies and resolution in CE.

References

1. Crisalli, P.; McCallum, C.; Pennathur, S. Label Free Detection of Nucleic Acids by Modulating Nanochannel Surfaces. *Chem. Commun.* **2015**, *51* (12), 2335–2338. DOI: 10.1039/C4CC09599E.
2. Zhang, Y.; D'Ambra, C. A.; Katsumata, R.; Burns, R. L.; Somervell, M. H.; Segalman, R. A.; Hawker, C. J.; Bates, C. M. Rapid and Selective Deposition of Patterned Thin Films on Heterogeneous Substrates via Spin Coating. *ACS Appl. Mater. Interfaces* **2019**, *11* (23), 21177–21183. DOI: 10.1021/acsami.9b05190.
3. Kramer, I. J.; Sargent, E. H. Colloidal Quantum Dot Photovoltaics: A Path Forward. *ACS Nano* **2011**, *5* (11), 8506–8514. DOI: 10.1021/nn203438u.
4. Davis, M. E.; Chen, Z.; Shin, D. M. Nanoparticle Therapeutics: An Emerging Treatment Modality for Cancer. *Nat Rev Drug Discov* **2008**, *7* (9), 771–782. DOI: 10.1038/nrd2614.
5. Shircliff, R. A.; Stradins, P.; Moutinho, H.; Fennell, J.; Ghirardi, M. L.; Cowley, S. W.; Branz, H. M.; Martin, I. T. Angle-Resolved XPS Analysis and Characterization of Monolayer and Multilayer Silane Films for DNA Coupling to Silica. *Langmuir* **2013**, *29* (12), 4057–4067. DOI: 10.1021/la304719y.
6. Nakazumi, T.; Hara, Y. Separation of Small DNAs by Gel Electrophoresis in a Fused Silica Capillary Coated with a Negatively Charged Copolymer. *Separations* **2017**, *4* (3), 28. DOI: 10.3390/separations4030028.
7. Hajba, L.; Guttman, A. Recent Advances in Column Coatings for Capillary Electrophoresis of Proteins. *TrAC Trends in Analytical Chemistry* **2017**, *90*, 38–44. DOI: 10.1016/j.trac.2017.02.013.
8. Lucy, C. A.; MacDonald, A. M.; Gulcev, M. D. Non-Covalent Capillary Coatings for Protein Separations in Capillary Electrophoresis. *J. Chromatogr. A* **2008**, *1184* (1–2), 81–105. DOI: 10.1016/j.chroma.2007.10.114.
9. Durney, B. C.; Crihfield, C. L.; Holland, L. A. Capillary Electrophoresis Applied to DNA: Determining and Harnessing Sequence and Structure to Advance Bioanalyses (2009–2014). *Anal Bioanal Chem* **2015**, *407* (23), 6923–6938. DOI: 10.1007/s00216-015-8703-5.
10. Uzgiris, E. E. Laser Doppler Methods in Electrophoresis. *Progress in Surface Science* **1981**, *10* (1), 53–164. DOI: 10.1016/0079-6816(81)90006-X.
11. Lyklema, J. Electrokinetics after Smoluchowski. *Colloids Surf. A Physicochem. Eng. Asp.* **2003**, *222* (1), 5–14. DOI: 10.1016/S0927-7757(03)00217-6.
12. Paria, S.; Khilar, K. C. A Review on Experimental Studies of Surfactant Adsorption at the Hydrophilic Solid–Water Interface. *Adv. Colloid Interface Sci.* **2004**, *110* (3), 75–95. DOI: 10.1016/j.cis.2004.03.001.
13. Melanson, J. E.; Baryla, N. E.; Lucy, C. A. Double-Chained Surfactants for Semipermanent Wall Coatings in Capillary Electrophoresis. *Anal. Chem.* **2000**, *72* (17), 4110–4114. DOI: 10.1021/ac000335z.
14. Melanson, J. E.; Baryla, N. E.; Lucy, C. A. Dynamic Capillary Coatings for Electroosmotic Flow Control in Capillary Electrophoresis. *TrAC Trends in Analytical Chemistry* **2001**, *20* (6–7), 365–374. DOI: 10.1016/S0165-9936(01)00067-X.
15. Mohabbati, S.; Westerlund, D. Improved Properties of the Non-Covalent Coating with N,N-Didodecyl-N, N-Dimethylammonium Bromide for the Separation of Basic Proteins

by Capillary Electrophoresis with Acidic Buffers in 25µm Capillaries. *J. Chromatogr. A* **2006**, *1121* (1), 32–39. DOI: 10.1016/j.chroma.2006.03.125.
16. Batz, N. G.; Mellors, J. S.; Alarie, J. P.; Ramsey, J. M. Chemical Vapor Deposition of Aminopropyl Silanes in Microfluidic Channels for Highly Efficient Microchip Capillary Electrophoresis-Electrospray Ionization-Mass Spectrometry. *Anal. Chem.* **2014**, *86* (7), 3493–3500. DOI: 10.1021/ac404106u.
17. Huhn, C.; Ramautar, R.; Wuhrer, M.; Somsen, G. W. Relevance and Use of Capillary Coatings in Capillary Electrophoresis–Mass Spectrometry. *Anal. Bioanal. Chem.* **2010**, *396* (1), 297–314. DOI: 10.1007/s00216-009-3193-y.
18. Figeys, D.; Zhang, Y.; Aebersold, R. Optimization of Solid Phase Microextraction - Capillary Zone Electrophoresis - Mass Spectrometry for High Sensitivity Protein Identification. *ELECTROPHORESIS* **1998**, *19* (13), 2338–2347. DOI: 10.1002/elps.1150191314.
19. Bateman, K. P.; White, R. L.; Thibault, P. Disposable Emitters for On-Line Capillary Zone Electrophoresis/Nanoelectrospray Mass Spectrometry. *Rapid Communications in Mass Spectrometry* **1997**, *11* (3), 307–315. DOI: 10.1002/(SICI)1097-0231(19970215)11:3<307::AID-RCM850>3.0.CO;2-M.
20. Leung, K.; Nielsen, I. M. B.; Criscenti, L. J. Elucidating the Bimodal Acid-Base Behavior of the Water-Silica Interface from First Principles. *Journal of the American Chemical Society* **2009**, *131* (51), 18358–18365. DOI: 10.1021/ja906190t.
21. Corradini, D.; Sprecacenere, L. Dependence of the Electroosmotic Flow in Bare Fused-Silica Capillaries from PH, Ionic Strength and Composition of Electrolyte Solutions Tailored for Protein Capillary Zone Electrophoresis. *Chromatographia* **2003**, *58* (9), 587–596. DOI: 10.1365/s10337-003-0098-3.
22. Pujari, S. P.; Scheres, L.; Marcelis, A. T. M.; Zuilhof, H. Covalent Surface Modification of Oxide Surfaces. *Angew. Chem. Int. Ed.* **2014**, *53* (25), 6322–6356. DOI: 10.1002/anie.201306709.
23. Giraud, L.; Nadarajah, R.; Matar, Y.; Bazin, G.; Sun, J.; Zhu, X. X.; Giasson, S. Amino-Functionalized Monolayers Covalently Grafted to Silica-Based Substrates as a Robust Primer Anchorage in Aqueous Media. *Appl. Surf. Sci.* **2016**, *370*, 476–485. DOI: 10.1016/j.apsusc.2016.02.141.
24. Shulman, L.; Pei, L.; Bahnasy, M. F.; Lucy, C. A. High PH Instability of Quaternary Ammonium Surfactant Coatings in Capillary Electrophoresis. *Analyst* **2017**, *142* (12), 2145–2151. DOI: 10.1039/C7AN00330G.
25. Okhrimenko, D. V.; Budi, A.; Ceccato, M.; Cárdenas, M.; Johansson, D. B.; Lybye, D.; Bechgaard, K.; Andersson, M. P.; Stipp, S. L. S. Hydrolytic Stability of 3-Aminopropylsilane Coupling Agent on Silica and Silicate Surfaces at Elevated Temperatures. *ACS Appl. Mater. Interfaces* **2017**, *9* (9), 8344–8353. DOI: 10.1021/acsami.6b14343.
26. Wang, C.; Lucy, C. A. Mixed Cationic/Anionic Surfactants for Semipermanent Wall Coatings in Capillary Electrophoresis. *Electrophoresis* **2004**, *25* (6), 825–832. DOI: 10.1002/elps.200305760.
27. Theodoly, O.; Cascão-Pereira, L.; Bergeron, V.; Radke, C. J. A Combined Streaming-Potential Optical Reflectometer for Studying Adsorption at the Water/Solid Surface. *Langmuir* **2005**, *21* (22), 10127–10139. DOI: 10.1021/la050685m.

28. Yassine, M. M.; Lucy, C. A. Factors Affecting the Temporal Stability of Semipermanent Bilayer Coatings in Capillary Electrophoresis Prepared Using Double-Chained Surfactants. *Anal. Chem.* **2004**, *76* (11), 2983–2990. DOI: 10.1021/ac035372f.
29. Zhang, F.; Sautter, K.; Larsen, A. M.; Findley, D. A.; Davis, R. C.; Samha, H.; Linford, M. R. Chemical Vapor Deposition of Three Aminosilanes on Silicon Dioxide: Surface Characterization, Stability, Effects of Silane Concentration, and Cyanine Dye Adsorption. *Langmuir* **2010**, *26* (18), 14648–14654. DOI: 10.1021/la102447y.
30. Yadav, A. R.; Sriram, R.; Carter, J. A.; Miller, B. L. Comparative Study of Solution–Phase and Vapor–Phase Deposition of Aminosilanes on Silicon Dioxide Surfaces. *Mater. Sci. Eng. C* **2014**, *35*, 283–290. DOI: 10.1016/j.msec.2013.11.017.
31. Kim, J.; Seidler, P.; Wan, L. S.; Fill, C. Formation, Structure, and Reactivity of Amino-Terminated Organic Films on Silicon Substrates. *J. Colloid Interface Sci.* **2009**, *329* (1), 114–119. DOI: 10.1016/j.jcis.2008.09.031.
32. Asenath Smith, E.; Chen, W. How To Prevent the Loss of Surface Functionality Derived from Aminosilanes. *Langmuir* **2008**, *24* (21), 12405–12409. DOI: 10.1021/la802234x.
33. Zhu, M.; Lerum, M. Z.; Chen, W. How to Prepare Reproducible, Homogeneous, and Hydrolytically Stable Aminosilane-Derived Layers on Silica. *Langmuir* **2012**, *28* (1), 416–423. DOI: 10.1021/la203638g.
34. Pasternack, R. M.; Rivillon Amy, S.; Chabal, Y. J. Attachment of 3-(Aminopropyl)Triethoxysilane on Silicon Oxide Surfaces: Dependence on Solution Temperature. *Langmuir* **2008**, *24* (22), 12963–12971. DOI: 10.1021/la8024827.
35. Seitz, O.; Fernandes, P. G.; Tian, R.; Karnik, N.; Wen, H.-C.; Stiegler, H.; Chapman, R. A.; Vogel, E. M.; Chabal, Y. J. Control and Stability of Self-Assembled Monolayers under Biosensing Conditions. *J. Mater. Chem.* **2011**, *21* (12), 4384–4392. DOI: 10.1039/C1JM10132C.
36. Shircliff, R. A.; Martin, I. T.; Pankow, J. W.; Fennell, J.; Stradins, P.; Ghirardi, M. L.; Cowley, S. W.; Branz, H. M. High-Resolution X-Ray Photoelectron Spectroscopy of Mixed Silane Monolayers for DNA Attachment. *ACS Appl. Mater. Interfaces* **2011**, *3* (9), 3285–3292. DOI: 10.1021/am200604q.
37. Zhang, F.; Srinivasan, M. P. Self-Assembled Molecular Films of Aminosilanes and Their Immobilization Capacities. *Langmuir* **2004**, *20* (6), 2309–2314. DOI: 10.1021/la0354638.
38. Metwalli, E.; Haines, D.; Becker, O.; Conzone, S.; Pantano, C. G. Surface Characterizations of Mono-, Di-, and Tri-Aminosilane Treated Glass Substrates. *J. Colloid Interface Sci.* **2006**, *298* (2), 825–831. DOI: 10.1016/j.jcis.2006.03.045.
39. Wayment, J. R.; Harris, J. M. Controlling Binding Site Densities on Glass Surfaces. *Anal. Chem.* **2006**, *78* (22), 7841–7849. DOI: 10.1021/ac061392g.
40. Olmos, D.; González-Benito, J.; Aznar, A. J.; Baselga, J. Hydrolytic Damage Study of the Silane Coupling Region in Coated Silica Microfibres: PH and Coating Type Effects. *J. Mater. Process. Tech.* **2003**, *143–144*, 82–86. DOI: 10.1016/S0924-0136(03)00325-X.
41. Jana, N. R.; Earhart, C.; Ying, J. Y. Synthesis of Water-Soluble and Functionalized Nanoparticles by Silica Coating. *Chem. Mater.* **2007**, *19* (21), 5074–5082. DOI: 10.1021/cm071368z.
42. Shyue, J.-J.; De Guire, M. R.; Nakanishi, T.; Masuda, Y.; Koumoto, K.; Sukenik, C. N. Acid−Base Properties and Zeta Potentials of Self-Assembled Monolayers Obtained via in Situ Transformations. *Langmuir* **2004**, *20* (20), 8693–8698. DOI: 10.1021/la049247q.

43. Huang, Xiaohua.; Gordon, M. J.; Zare, R. N. Current-Monitoring Method for Measuring the Electroosmotic Flow Rate in Capillary Zone Electrophoresis. *Anal. Chem.* **1988**, *60* (17), 1837–1838. DOI: 10.1021/ac00168a040.
44. Kunc, F.; Balhara, V.; Brinkmann, A.; Sun, Y.; Leek, D. M.; Johnston, L. J. Quantification and Stability Determination of Surface Amine Groups on Silica Nanoparticles Using Solution NMR. *Anal. Chem.* **2018**, *90* (22), 13322–13330. DOI: 10.1021/acs.analchem.8b02803.
45. Hunter, R. J. *Zeta Potential in Colloid Science: Principles and Applications*; Academic Press Limited, 1981. DOI: 10.1016/B978-0-12-361961-7.50007-9.
46. Sze, A.; Erickson, D.; Ren, L.; Li, D. Zeta-Potential Measurement Using the Smoluchowski Equation and the Slope of the Current–Time Relationship in Electroosmotic Flow. *J. Colloid Interface Sci.* **2003**, *261* (2), 402–410. DOI: 10.1016/S0021-9797(03)00142-5.
47. Zhai, Q.; Zhou, C.; Zhao, S.; Peng, C.; Han, Y. Kinetic Study of Alkoxysilane Hydrolysis under Acidic Conditions by Fourier Transform Near Infrared Spectroscopy Combined with Partial Least-Squares Model. *Ind. Eng. Chem. Res.* **2014**, *53* (35), 13598–13609. DOI: 10.1021/ie5012195.
48. Kannan, B.; Higgins, D. A.; Collinson, M. M. Aminoalkoxysilane Reactivity in Surface Amine Gradients Prepared by Controlled-Rate Infusion. *Langmuir* **2012**, *28* (46), 16091–16098. DOI: 10.1021/la303580c.
49. Qin, S.; Xiong, Y.; Li, J.; Wan, H.; Fang, S.; Duan, M.; Li, R.; Liao, D. Real-Time Adsorption and Photodegradation Investigation of Dye Removal on g-C_3N_4 Surface by Attenuated Total Reflectance Induced Evanescent Spectroscopy. *J. Phys. Chem. C* **2021**, *125* (7), 4027–4040. DOI: 10.1021/acs.jpcc.0c11482.
50. Almutairi, Z. A.; Glawdel, T.; Ren, C. L.; Johnson, D. A. A Y-Channel Design for Improving Zeta Potential and Surface Conductivity Measurements Using the Current Monitoring Method. *Microfluid. Nanofluidics* **2009**, *6* (2), 241–251. DOI: 10.1007/s10404-008-0320-6.
51. Andersen, M. B.; Frey, J.; Pennathur, S.; Bruus, H. Surface-Dependent Chemical Equilibrium Constants and Capacitances for Bare and 3-Cyanopropyldimethylchlorosilane Coated Silica Nanochannels. *J. Colloid Interface Sci.* **2011**, *353* (1), 301–310. DOI: 10.1016/j.jcis.2010.09.025.
52. Chou, K.-H.; McCallum, C.; Gillespie, D.; Pennathur, S. An Experimental Approach to Systematically Probe Charge Inversion in Nanofluidic Channels. *Nano Lett.* **2018**, *18* (2), 1191–1195. DOI: 10.1021/acs.nanolett.7b04736.
53. Kirby, B. J.; Hasselbrink, E. F. Zeta potential of microfluidic substrates: 1. Theory, experimental techniques, and effects on separations. *Electrophoresis* **2004**, *25* (2), 187–202. DOI: 10.1002/elps.200305754.
54. Kirby, B. J.; Wheeler, A. R.; Zare, R. N.; Fruetel, J. A.; Shepodd, T. J. Programmable Modification of Cell Adhesion and Zeta Potential in Silica Microchips. *Lab Chip* **2003**, *3* (1), 5–10. DOI: 10.1039/B210621N.
55. Valko, I. E.; Siren, H.; Riekkola, M.-L. Characteristics of Electroosmotic Flow in Capillary Electrophoresis in Water and in Organic Solvents without Added Ionic Species. *J. Microcolumn Separations* **1999**, *11* (3), 199–208. DOI: 10.1002/(SICI)1520-667X(1999)11:3<199::AID-MCS5>3.0.CO;2-D.

56. Williams, S.; Venkateswaran, N.; O'Donnell, T. D. B.; Crisalli, P.; Helmy, S.; Napoli, M. T.; Pennathur, S. Assessing Stability, Durability, and Protein Adsorption Behavior of Hydrophilic Silane Coatings in Glass Microchannels. *J. Anal. Bioanal. Tech.* **2016**, *7* (3), 318–325. DOI: 10.4172/2155-9872.1000318.
57. Schrader, M. E.; Block, A. Tracer Study of Kinetics and Mechanism of Hydrolytically Induced Interfacial Failure. *J. Polym. Sci. Pol. Sym.* **1971**, *34* (1), 281–291. DOI: 10.1002/polc.5070340126.
58. Salmon, L.; Thominette, F.; Pays, M. F.; Verdu, J. Hydrolytic Degradation of Model Networks Simulating the Interfacial Layers in Silanecoupled Epoxy/Glass Composites. *Compos. Sci. Technol.* **1997**, *57* (8), 1119–1127. DOI: 10.1016/S0266-3538(97)00038-9.
59. Etienne, M.; Walcarius, A. Analytical Investigation of the Chemical Reactivity and Stability of Aminopropyl-Grafted Silica in Aqueous Medium. *Talanta* **2003**, *59* (6), 1173–1188. DOI: 10.1016/S0039-9140(03)00024-9.
60. Jüttner, F.; von Smoluchowski, M. Handbuch Der Elektrizität Und Des Magnetismus. *Z. Elektrochem. angew. phys. Chem.* **1921**, *27* (23-24), 582–583. DOI: 10.1002/bbpc.19210272310.
61. Santiago, J. G. Electroosmotic Flows in Microchannels with Finite Inertial and Pressure Forces. *Anal. Chem.* **2001**, *73* (10), 2353–2365. DOI: 10.1021/ac0101398.
62. Paul, P. H.; Garguilo, M. G.; Rakestraw, D. J. Imaging of Pressure- and Electrokinetically Driven Flows through Open Capillaries. *Anal. Chem.* **1998**, *70* (13), 2459–2467. DOI: 10.1021/ac9709662.
63. Tang, S.-W.; Chang, C.-H.; Wei, H.-H. Roles of Solution Conductivity Mismatch in Transient Current and Fluid Transport in Electrolyte Displacement by Electro-Osmotic Flow. *Microfluid. Nanofluid* **2011**, *10* (2), 337–353. DOI: 10.1007/s10404-010-0672-6.
64. Arulanandam, S.; Li, D. Determining ζ Potential and Surface Conductance by Monitoring the Current in Electro-Osmotic Flow. 8. DOI: 10.1006/jcis.2000.6783.
65. Walcarius, A.; Etienne, M.; Bessière, J. Rate of Access to the Binding Sites in Organically Modified Silicates. 1. Amorphous Silica Gels Grafted with Amine or Thiol Groups. *Chem. Mater.* **2002**, *14* (6), 2757–2766. DOI: 10.1021/cm021117k.
66. Hughes, C.; Yeh, L.-H.; Qian, S. Field Effect Modulation of Surface Charge Property and Electroosmotic Flow in a Nanochannel: Stern Layer Effect. *J. Phys. Chem. C* **2013**, *117* (18), 9322–9331. DOI: 10.1021/jp402018u.
67. Scales, P. J.; Grieser, F.; Healy, T. W.; White, L. R.; Chan, D. Y. C. Electrokinetics of the Silica-Solution Interface: A Flat Plate Streaming Potential Study. *Langmuir* **1992**, *8* (3), 965–974. DOI: 10.1021/la00039a037.
68. *CRC Handbook of Chemistry and Physics*, 101st Edition (Internet Version 2020).; Rumble, J. R., Ed.; CRC Press/Taylor & Francis: Boca Raton, FL.
69. Moon, J. H.; Shin, J. W.; Kim, S. Y.; Park, J. W. Formation of Uniform Aminosilane Thin Layers: An Imine Formation To Measure Relative Surface Density of the Amine Group. *Langmuir* **1996**, *12* (20), 4621–4624. DOI: 10.1021/la9604339.
70. Rostami, M.; Mohseni, M.; Ranjbar, Z. Investigating the Effect of PH on the Surface Chemistry of an Amino Silane Treated Nano Silica. *Pigment. Resin Technol.* **2011**, *40* (6), 363–373. DOI: 10.1108/03699421111180509.
71. Jesionowski, T. Influence of Aminosilane Surface Modification and Dyes Adsorption on Zeta Potential of Spherical Silica Particles Formed in Emulsion System. *Colloids Surf. A*

Physicochem. Eng. Asp. **2003**, *222* (1–3), 87–94. DOI: 10.1016/S0927-7757(03)00237-1.
72. Elimelech, M.; Nagai, M.; Ko, C.-H.; Ryan, J. N. Relative Insignificance of Mineral Grain Zeta Potential to Colloid Transport in Geochemically Heterogeneous Porous Media. *Environ. Sci. Technol.* **2000**, *34* (11), 2143–2148. DOI: 10.1021/es9910309.
73. Watson, H.; Norström, A.; Torrkulla, Å.; Rosenholm, J. Aqueous Amino Silane Modification of E-Glass Surfaces. *J. Colloid Interface Sci.* **2001**, *238* (1), 136–146. DOI: 10.1006/jcis.2001.7506.
74. Goodwin, J. W.; Harbron, R. S.; Reynolds, P. A. Functionalization of Colloidal Silica and Silica Surfaces via Silylation Reactions. *Colloid Polym. Sci.* **1990**, *268* (8), 766–777. DOI: 10.1007/BF01411109.
75. Schwer, Christine.; Kenndler, Ernst. Electrophoresis in Fused-Silica Capillaries: The Influence of Organic Solvents on the Electroosmotic Velocity and the .Zeta. Potential. *Anal. Chem.* **1991**, *63* (17), 1801–1807. DOI: 10.1021/ac00017a026.
76. Arkles, B.; Steinmetz, J. R.; Zazyczny, J.; Mehta, P. Factors Contributing to the Stability of Alkoxysilanes in Aqueous Solution. *J. Adhes. Sci. Technol.* **1992**, *6* (1), 193–206. DOI: 10.1163/156856192X00133.
77. Bernards, T. N. M.; van Bommel, M. J.; Boonstra, A. H. Hydrolysis-Condensation Processes of the Tetra-Alkoxysilanes TPOS, TEOS and TMOS in Some Alcoholic Solvents. *J. Non Cryst. Solids.* **1991**, *134* (1), 1–13. DOI: 10.1016/0022-3093(91)90005-Q.
78. Brochier Salon, M.-C.; Bayle, P.-A.; Abdelmouleh, M.; Boufi, S.; Belgacem, M. N. Kinetics of Hydrolysis and Self Condensation Reactions of Silanes by NMR Spectroscopy. *Colloids Surf. A Physicochem. Eng. Asp.* **2008**, *312* (2–3), 83–91. DOI: 10.1016/j.colsurfa.2007.06.028.
79. Issa, A.; Luyt, A. Kinetics of Alkoxysilanes and Organoalkoxysilanes Polymerization: A Review. *Polymers* **2019**, *11* (3), 537. DOI: 10.3390/polym11030537.
80. Motevalian, S. P.; Aro, S. C.; Cheng, H. Y.; Day, T. D.; van Duin, A. C. T.; Badding, J. V.; Borhan, A. Kinetics of Silane Decomposition in High-Pressure Confined Chemical Vapor Deposition of Hydrogenated Amorphous Silicon. *Ind. Eng. Chem. Res.* **2017**, *56* (51), 14995–15000. DOI: 10.1021/acs.iecr.7b03515.
81. Liu, J.-F.; Ducker, W. A. Surface-Induced Phase Behavior of Alkyltrimethylammonium Bromide Surfactants Adsorbed to Mica, Silica, and Graphite. *J. Phys. Chem. B* **1999**, *103* (40), 8558–8567. DOI: 10.1021/jp991685w.
82. Saino, R.; Akamatsu, M.; Sakai, K.; Sakai, H. Morphology of Surfactant Mixtures at Solid/Liquid Interfaces: High-Speed AFM Observation. *Colloids Surf. A: Physicochem. Eng. Asp.* **2021**, *616*, 126297. DOI: 10.1016/j.colsurfa.2021.126297.
83. Tiberg, F.; Joensson, B.; Tang, J.; Lindman, B. Ellipsometry Studies of the Self-Assembly of Nonionic Surfactants at the Silica-Water Interface: Equilibrium Aspects. *Langmuir* **1994**, *10* (7), 2294–2300. DOI: 10.1021/la00019a045.
84. Pagac, E. S.; Prieve, D. C.; Tilton, R. D. Kinetics and Mechanism of Cationic Surfactant Adsorption and Coadsorption with Cationic Polyelectrolytes at the Silica−Water Interface. *Langmuir* **1998**, *14* (9), 2333–2342. DOI: 10.1021/la971308f.
85. Velegol, S. B.; Fleming, B. D.; Biggs, S.; Wanless, E. J.; Tilton, R. D. Counterion Effects on Hexadecyltrimethylammonium Surfactant Adsorption and Self-Assembly on Silica. *Langmuir* **2000**, *16* (6), 2548–2556. DOI: 10.1021/la9910935.

86. Griffin, L. R.; Browning, K. L.; Truscott, C. L.; Clifton, L. A.; Webster, J.; Clarke, S. M. A Comparison of Didodecyldimethylammonium Bromide Adsorbed at Mica/Water and Silica/Water Interfaces Using Neutron Reflection. *J. Colloid Interface Sci.* **2016**, *478*, 365–373. DOI: 10.1016/j.jcis.2016.06.015.
87. Biswas, S. C.; Chattoraj, D. K. Kinetics of Adsorption of Cationic Surfactants at Silica-Water Interface. *J. Colloid Interface Sci.* **1998**, *205* (1), 12–20. DOI: 10.1006/jcis.1998.5574.
88. Eskilsson, K.; Yaminsky, V. V. Deposition of Monolayers by Retraction from Solution: Ellipsometric Study of Cetyltrimethylammonium Bromide Adsorption at Silica−Air and Silica−Water Interfaces. *Langmuir* **1998**, *14* (9), 2444–2450. DOI: 10.1021/la971066j.
89. Atkin, R.; Craig, V. S. J.; Biggs, S. Adsorption Kinetics and Structural Arrangements of Cationic Surfactants on Silica Surfaces. *Langmuir* **2000**, *16* (24), 9374–9380. DOI: 10.1021/la0001272.
90. Tsagkaropoulou, G.; Allen, F. J.; Clarke, S. M.; Camp, P. J. Self-Assembly and Adsorption of Cetyltrimethylammonium Bromide and Didodecyldimethylammonium Bromide Surfactants at the Mica–Water Interface. *Soft Matter* **2019**, *15* (41), 8402–8411. DOI: 10.1039/C9SM01464K.
91. Cieśla, J.; Koczańska, M.; Narkiewicz-Michałek, J.; Szymula, M.; Bieganowski, A. The Physicochemical Properties of CTAB Solutions in the Presence of α-Tocopherol. *J. Mol. Liq.* **2016**, *222*, 463–470. DOI: 10.1016/j.molliq.2016.07.058.
92. Bello, M. S.; Capelli, L.; Righetti, P. G. Dependence of the Electroosmotic Mobility on the Applied Electric Field and Its Reproducibility in Capillary Electrophoresis. *J Chromatogr A* **1994**, *684* (2), 311–322. DOI: 10.1016/0021-9673(94)00545-1.
93. Abrams, A. S.; Eden, A.; Zhou, L.; Wang, B.; Huber, D. E.; Pennathur, S. Real-Time Zeta Potential Analysis of Microchannel Surfaces during Aminosilane Deposition and Exposure Using Current Monitoring. *Anal. Chem.* **2021**, *93* (49), 16512–16519. DOI: 10.1021/acs.analchem.1c03628.
94. Chang, H. Tsung.; Yeung, E. S. Self-Regulating Dynamic Control of Electroosmotic Flow in Capillary Electrophoresis. *Anal. Chem.* **1993**, *65* (5), 650–652. DOI: 10.1021/ac00053a028.
95. Fleming, B. D.; Biggs, S.; Wanless, E. J. Slow Organization of Cationic Surfactant Adsorbed to Silica from Solutions Far below the CMC. *J. Phys. Chem. B* **2001**, *105* (39), 9537–9540. DOI: 10.1021/jp011503+.
96. Tiberg, F. Physical Characterization of Non-Ionic Surfactant Layers Adsorbed at Hydrophilic and Hydrophobic Solid Surfaces by Time-Resolved Ellipsometry. *Faraday Trans.* **1996**, *92* (4), 531. DOI: 10.1039/ft9969200531.
97. Lucy, C. A.; Underhill, R. S. Characterization of the Cationic Surfactant Induced Reversal of Electroosmotic Flow in Capillary Electrophoresis. *Anal. Chem.* **1996**, *68* (2), 300–305. DOI: 10.1021/ac950632h.
98. Pei, L.; Lucy, C. A. Insight into the Stability of Poly(Diallydimethylammoniumchloride) and Polybrene Poly Cationic Coatings in Capillary Electrophoresis. *Journal of Chromatography A* **2014**, *1365*, 226–233. DOI: 10.1016/j.chroma.2014.09.013.
99. Carmona-Ribeiro, A. M.; Carmona-Ribeiro, A. M. *The Versatile Dioctadecyldimethylammonium Bromide*; IntechOpen, 2017. DOI: 10.5772/68020.
100. Pattky, M.; Huhn, C. Advantages and Limitations of a New Cationic Coating Inducing a Slow Electroosmotic Flow for CE-MS Peptide Analysis: A Comparative Study with

Commercial Coatings. *Anal Bioanal Chem* **2013**, *405* (1), 225–237. DOI: 10.1007/s00216-012-6459-8.
101. Allen, F. J.; Truscott, C. L.; Welbourn, R. J. L.; Clarke, S. M. Influence of Surfactants on a Pre-Adsorbed Cationic Layer: Removal and Modification. *J. Colloid Interface Sci.* **2021**, *588*, 427–435. DOI: 10.1016/j.jcis.2020.12.047.
102. Gonçalves, R. A.; Lam, Y.-M.; Lindman, B. Double-Chain Cationic Surfactants: Swelling, Structure, Phase Transitions and Additive Effects. *Molecules* **2021**, *26* (13), 3946. DOI: 10.3390/molecules26133946.
103. Yassine, M. M.; Lucy, C. A. Enhanced Stability Self-Assembled Coatings for Protein Separations by Capillary Zone Electrophoresis through the Use of Long-Chained Surfactants. *Anal. Chem.* **2005**, *77* (2), 620–625. DOI: 10.1021/ac048909d.
104. Benatti, C. R.; Feitosa, E.; Fernandez, R. M.; Lamy-Freund, M. T. Structural and Thermal Characterization of Dioctadecyldimethylammonium Bromide Dispersions by Spin Labels. *Chemistry and Physics of Lipids* **2001**, *111* (2), 93–104. DOI: 10.1016/S0009-3084(01)00134-7.
105. Tang, G. Y.; Yang, C.; Chai, J. C.; Gong, H. Q. Joule Heating Effect on Electroosmotic Flow and Mass Species Transport in a Microcapillary. *International Journal of Heat and Mass Transfer* **2004**, *47* (2), 215–227. DOI: 10.1016/j.ijheatmasstransfer.2003.07.006.
106. Yates, D. E.; Levine, S.; Healy, T. W. Site-Binding Model of the Electrical Double Layer at the Oxide/Water Interface. *J. Chem. Soc., Faraday Trans. 1* **1974**, *70* (0), 1807. DOI: 10.1039/f19747001807.
107. Booth, F. The Dielectric Constant of Water and the Saturation Effect. *The Journal of Chemical Physics* **1951**, *19* (4), 391–394. DOI: 10.1063/1.1748233.
108. Frankel, G. S.; Vienna, J. D.; Lian, J.; Scully, J. R.; Gin, S.; Ryan, J. V.; Wang, J.; Kim, S. H.; Windl, W.; Du, J. A Comparative Review of the Aqueous Corrosion of Glasses, Crystalline Ceramics, and Metals. *npj Mater Degrad* **2018**, *2* (1), 15. DOI: 10.1038/s41529-018-0037-2.
109. Miller, J. F. Determination of Protein Charge in Aqueous Solution Using Electrophoretic Light Scattering: A Critical Investigation of the Theoretical Fundamentals and Experimental Methodologies. *Langmuir* **2020**, *36* (29), 8641–8654. DOI: 10.1021/acs.langmuir.0c01694.
110. McBride, R. J.; Miller, J. F.; Blanazs, A.; Hähnle, H.-J.; Armes, S. P. Synthesis of High Molecular Weight Water-Soluble Polymers as Low-Viscosity Latex Particles by RAFT Aqueous Dispersion Polymerization in Highly Salty Media. *Macromolecules* **2022**, *55* (17), 7380–7391. DOI: 10.1021/acs.macromol.2c01071.
111. Miller, J. F.; Schätzel, K.; Vincent, B. The Determination of Very Small Electrophoretic Mobilities in Polar and Nonpolar Colloidal Dispersions Using Phase Analysis Light Scattering. *J. Colloid Interface Sci.* **1991**, *143* (2), 532–554. DOI: 10.1016/0021-9797(91)90286-H.
112. Feltham, A. M.; Spiro, M. Platinized Platinum Electrodes. *Chem. Rev.* **1971**, *71* (2), 177–193. DOI: 10.1021/cr60270a002.

Appendix A. Supporting Information for "Real-Time Zeta Potential Analysis of Microchannel Surfaces during Aminosilane Deposition and Exposure Using Current Monitoring"

The MATLAB® algorithm for Automated Zeta Potential Analysis may be accessed free of charge at: https://github.com/austinabrams/aza/.

1. System Design

The study of surface reactions imposes more stringent requirements than are needed for single-shot measurements in equilibrium conditions. Fluid conditions within the reservoirs must be relatively stable over the length of the reaction (e.g., hours to days), and native surfaces are required for each instance. We use high-volume reservoirs (relative to the capillary) that were capped to maintain the solution composition and minimize transport-induced mixing over long operating periods.

We chose a channel diameter of 1.2 μm to minimize Joule heating[105] and pressure-driven flow resulting from unintentional differences in fluid levels between reservoirs. We employed an 8 mm channel length to increase measurement frequency while reducing the relative influence of diffusion compared to advective transport under the applied electric field and concentration gradient. Our channel design has the advantages that it is constructed from commercially available capillary tubing and requires minimal fabrication; this design allows channels to be prepared in bulk and at low cost.

2. Temporal Resolution of Buffer Exchanges

To assess the temporal response of automated zeta potential analysis (AZA) compared to the known reaction time of around 15 s for pH-based surface protonation of silica gels,[65] we performed additional buffer and pH exchange experiments (Figure S1). Unlike conventional analysis of a substrate immersed in a large beaker of solution, AZA requires solution to be displaced through the capillary before surface reactions can occur. We found that the time to reach stable zeta potential (ζ) values after a pH or buffer exchange was related to the time to displace solution from the capillary, as the traversal time is inversely proportional to the applied electric field strength and EOF velocity. This stabilization time was 38–72 s for buffer exchange experiments where E_0 = 30 kV/m, while at 60 kV/m this time was reduced to 23–27 s (Table S1). Even with a delay time of 72 s at 30 kV/m, AZA has sufficient temporal resolution to extract the kinetics of many reactions which occur at slower rates than surface protonation.

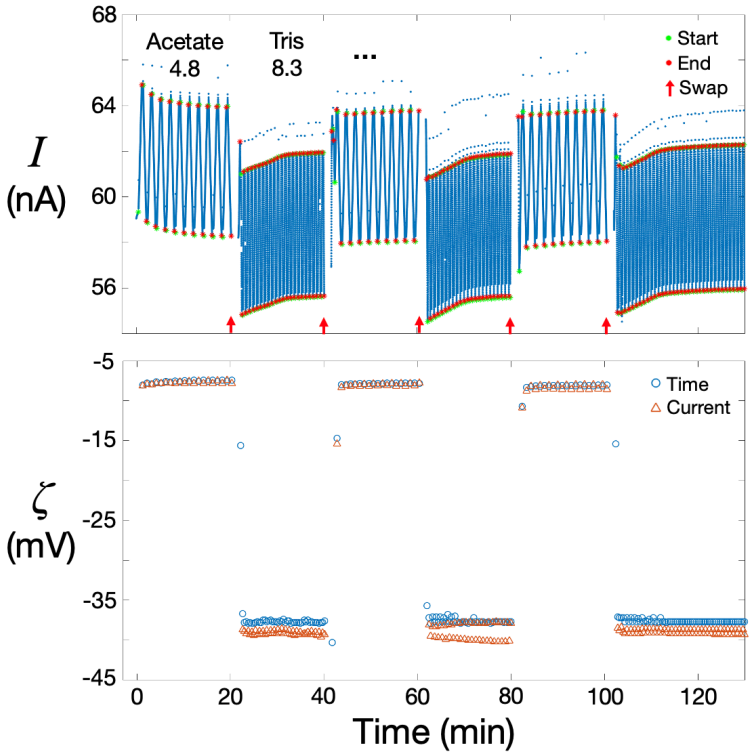

Figure S1. Current monitoring cycles and calculated zeta potential response as an unconditioned capillary was exposed to pH 4.8 acetate or pH 8.3 Tris buffered saline solutions. Measured conductivities were 1.69 and 1.63 S/m, respectively. 1× solutions consisted of 20 mM buffer and 150 mM NaCl. Zeta potentials were calculated using traversal time (eq 3) or the slope method.[46]

Table S1. Time for Zeta Potential Readings to Stabilize after In Situ Buffer Exchanges

Electric Field Strength (kV/m)	Buffers in Exchange (A to B)	Observed Stabilization Time (s)[1]	Standard Deviation (s)
60	MES to Tris	23	± 3
60	Tris to MES	27	± 1
30	MES to Tris	38	± 1
30	Tris to MES	72	± 4
30	Acetate to Phosphate	38	± 2

30	Phosphate to Tris	35	± 2
30	Tris to Acetate	86	± 2

[1]Average time until the deviation was less than 2 mV consecutive zeta potential readings.

3. Zeta Potential vs pH of Bare And APTMS-Coated Capillaries

Table S2. Time-Averaged Equilibrium Zeta Potentials of Bare Capillary in Varying pH

pH	ζ (mV)[1]	Confidence Interval, 95% (± mV)	Sample Size[2]	Buffer	Electric Field Strength (kV/m)	Conductivity (S/m)	Day[3]
2.19	0.6	0.1	6	Phosphate	123	1.63	1
7.11	-26.5	0.1	37	Phosphate	30	1.63	1
3.11	0.8	0.2	6	Citrate	120	1.63	1
8.38	-34.9	0.1	19	Tris	30	1.63	1
4.77	-3.7	0.1	5	Acetate	30	1.63	1
9.55	-35.4	0.1	20	CHES	30	1.63	1
6.16	-16.0	0.1	10	MES	30	1.63	1
10.37	-38.2	0.1	9	CAPS	30	1.63	1
4.84	-2.9	0.1	4	Citrate	30	1.63	2
5.50	-5.9	0.1	10	Citrate	30	1.63	2
3.99	-1.1	0.2	9	Citrate	90	1.63	2
2.14	0.8	0.1	7	Phosphate	30	1.63	1
3.07	0.5	0.1	3	Citrate	30	1.63	1
3.85	-0.8	0.1	4	Citrate	30	1.63	1
4.72	-2.8	0.1	8	Citrate	30	1.63	1
5.34	-4.9	0.1	257	Citrate	30	1.63	1
6.12	-12.4	0.4	24	MES	30	1.63	2
7.05	-24.4	0.5	746	Phosphate	30	1.63	2
8.36	-31.4	0.3	284	Tris	30	1.63	3
6.67	-16.6	0.1	17	Bis-Tris	30	1.63	3
7.59	-26.5	0.1	8	HEPES	30	1.63	3
9.47	-35.0	0.7	2189	CHES	30	1.63	3
10.25	-33.3	0.6	21	CAPS	30	1.63	3
12.62	-35.6	0.7	11	Phosphate	30	1.63	3
5.00	-2.7	0.1	8	Acetate	20.9	1.63	1
5.34	-3.4	0.1	7	Acetate	20.9	1.64	1
5.85	-5.8	0.1	6	Acetate	20.9	1.66	1

5.77	-6.3	0.1	5	Phosphate	20.9	1.61	2
6.12	-8.6	0.5	4	Phosphate	20.9	1.62	2
6.45	-13.0	0.2	17	Phosphate	20.9	1.64	2
6.75	-15.8	0.1	6	Phosphate	20.9	1.65	2
7.07	-18.5	0.5	5	Phosphate	20.9	1.66	2
7.28	-20.2	0.7	5	Phosphate	20.9	1.67	2
7.61	-23.0	1.4	3	Phosphate	20.9	1.68	2
7.93	-24.9	0.5	6	Phosphate	20.9	1.70	2
8.12	-26.0	0.2	2	Borate	20.9	1.55	2
8.41	-28.3	0.3	4	Borate	20.9	1.57	2
8.73	-33.7	0.1	4	Borate	20.9	1.60	4
8.98	-35.2	0.1	6	Borate	20.9	1.63	5
9.27	-37.3	0.1	9	Borate	20.9	1.65	5
9.54	-39.0	0.2	7	Borate	20.9	1.67	5
9.91	-39.3	0.1	10	Borate	20.9	1.70	5
10.17	-38.8	0.4	3	Borate	20.9	1.72	5
10.47	-38.3	0.5	3	Borate	20.9	1.75	6
12.00	-34.9	0.2	18	Phosphate	20.9	1.95	7

[1] Time-averaged zeta potential after reaching equilibrium (< 2 mV deviation between readings).
[2] Number of zeta potentials used to calculate time-averaged value.
[3] Individual titration series from Figure 2c (1: ■, 2: ●, 3: ◆) are listed chronologically and separated by horizontal lines. Capillary size (d × L): 1.2 µm × 8.0 mm (■/●), 1.1 µm × 23.9 mm (◆). Buffer concentration: 20 mM (■/●), 10 mM (◆).

Table S3. Solution measurements of APTMS capillary exposures to varying pH

pH	Buffer	ζ_{bare}	$\zeta_{0\ h}$	$\zeta_{36\ h}$	$\sigma_{0.9\times}$	$\sigma_{1\times}$
2.10	Phosphate	4.4	58.4	57.1	1.44	1.60
4.86	Acetate	-5.3	44.3	35.6	1.55	1.69
6.04	Phosphate	-12.4	28.7	13.6	1.43	1.58
7.12	Phosphate	-24.4	15.7	-9.0	1.43	1.58
8.33	Tris	-30.4	14.7	-20.5	1.49	1.63
9.55	CHES	-35.5	-7.9	-34.4	1.44	1.59
10.53	CAPS	-37.5	-18.1	-35.6	1.46	1.60

3. Zeta Potential vs Time of APS Coating Formations and Exposures

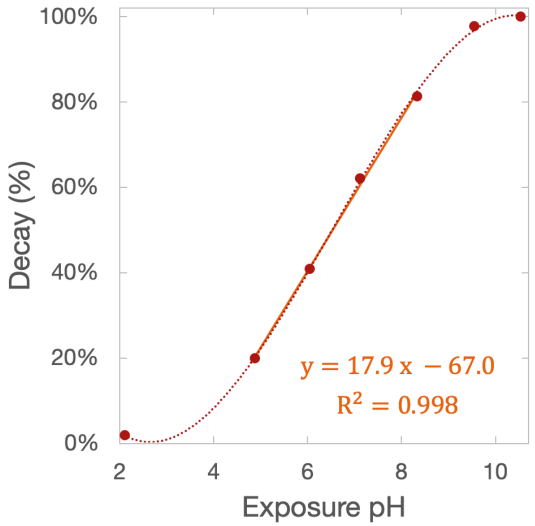

Figure S2. Normalized zeta potential decay after 36 h exposure of APTMS-coated capillaries to varying pH solutions (Table S3). A linear fit shows the decay rate from pH 4.9 to 8.3.

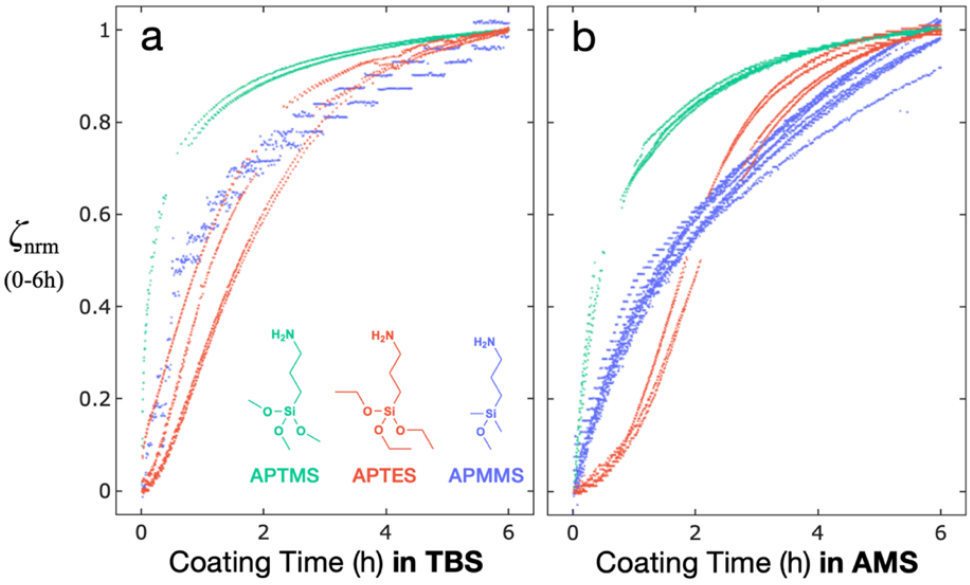

Figure S3. Normalized zeta potential response of 1 mM coating formations in (a) TBS or (b) AMS, calculated by dividing the change in zeta potential from 0 to time, *t*, by the change from 0 to 6 h.

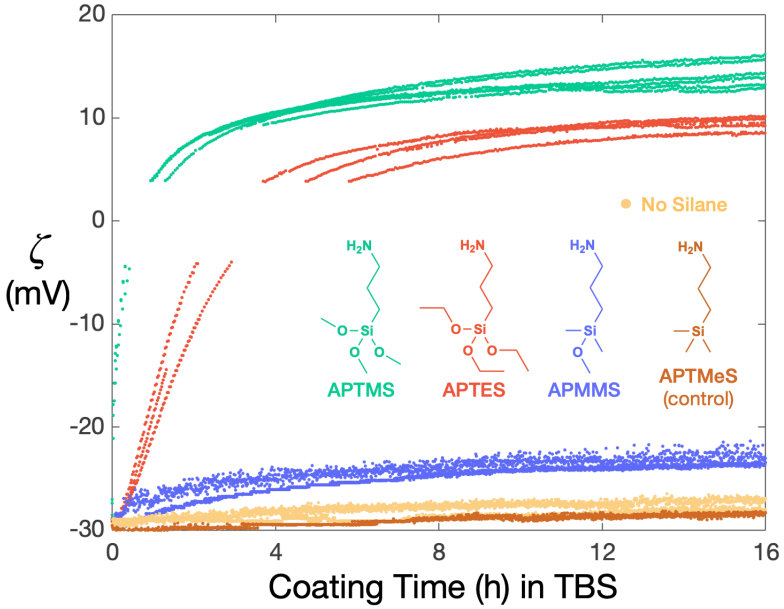

Figure S4. Zeta potential response over 16 h coating formations, with 3-aminopropyltrimethylsilane and silane-free TBS controls. At 0 h, APS was added to TBS reservoirs at 1 mM concentration.

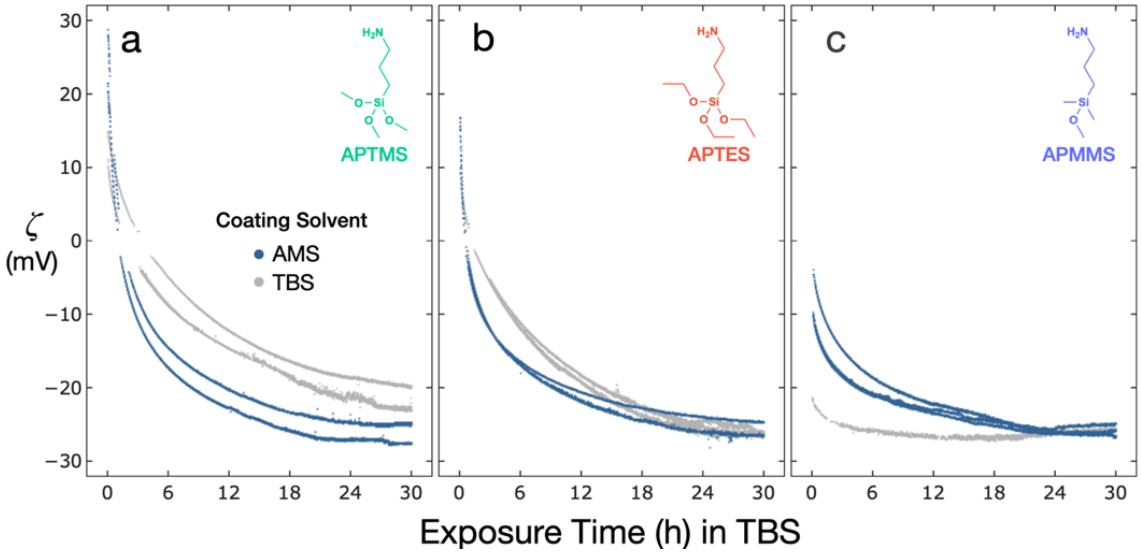

Figure S5. Raw zeta potential response of APS coatings exposed to silane-free, pH 8.3 TBS. Coatings were formed over 6 hm with 1 mM respective monomer in TBS or AMS reservoirs.

4. Inferring Amine Coverage from Zeta Potential Measurements

4.1. Theoretical Model: Design and Limitations

To understand the relationship between zeta potential measured during APS coating formation or dissociation and the relative densities of amine and silanol groups on the surface, we developed a model using COMSOL Multiphysics® (see Supporting Info). We numerically solved for the distribution of ions and electrostatic potential at a cross-section within the capillary and included the charge-regulated equilibrium reactions, corresponding to the protonation and deprotonation of silanols and surface-bound aminosilanes, as a unifying boundary condition for surface charge density. We calibrated our model by fitting four physicochemical parameters (pK_a values of silanol protonation and deprotonation, total surface site density, and Stern layer capacitance) to our experimental pH titration results for a bare silica capillary from pH 2.1 to 8.3 (Figure 2c). All fitted parameters (Table S4) were confirmed to be within the ranges reported in the literature [66].

By assuming a 1:1 molar ratio (*i.e.*, each surface-bound aminosilane consumes one surface silanol; other ratios in Figure S5), we estimated the theoretical influence of aminosilane density on measured zeta potential in different pH conditions (Figure S6a). In accordance with expectations, the simulated zeta potentials increased with decreasing solution pH and with increasing amine coverage. Two regions appeared in which zeta potential was highly sensitive to small differences in APS coverage. First, the increase in ζ around 0% to 8% coverage was most prominent at pH $\leq$ 4.87, as the density of protonated aminosilanes ($Si-R-NH_3^+$) and neutral silanols (SiOH) increases with decreasing pH below their respective pK_a values. Second, a sharp increase in ζ between roughly 40% and 60% coverage is visible at all pH as the total number of surface-bound aminosilanes exceeded that

of silanols; this effect was most significant at high pH ≥ 4.87, where a considerable number of silanols are deprotonated (SiO^-) and surface-bound aminosilanes are predominantly neutral ($Si-R-NH_2$). The intricacies of this relationship are useful in interpreting our results and elucidating the pH-dependent charge response and coverage of aminosilane coatings.

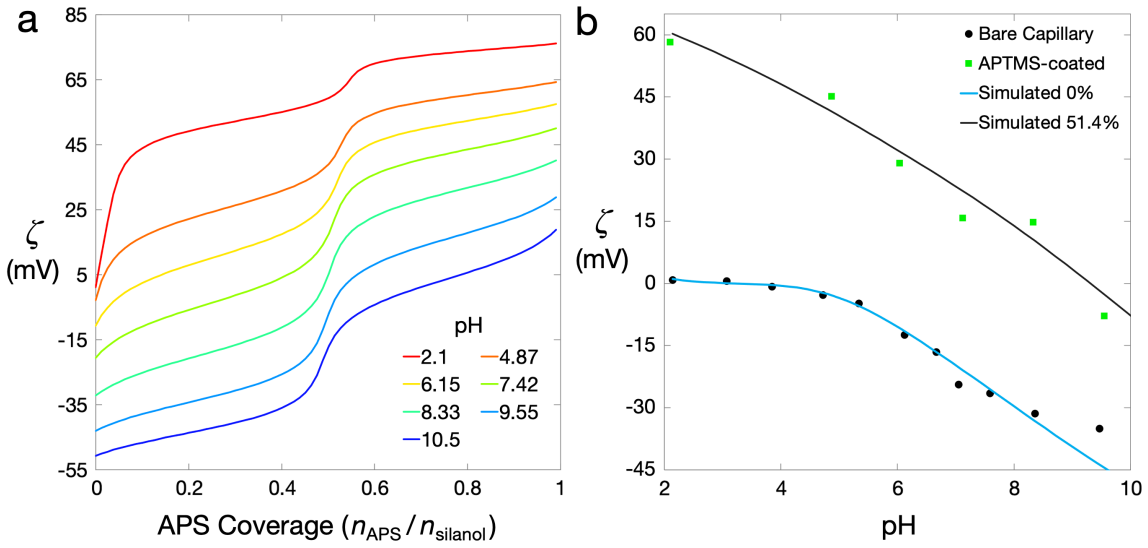

Figure S6. (a) Simulated zeta potential *vs.* APS coverage in varying pH levels of 160 mM NaCl solution, assuming a 1:1 APS-to-silanol consumption ratio (see Supporting Info). (b) Simulated ζ–pH response for bare and APTMS-coated capillary surfaces. The bare capillary response from pH 2.1 to 8.3 was used to fit four physicochemical parameters in the model (see Table S4).

In Figure S6b, we examine the differences between simulated and experimental zeta potential *versus* pH response for bare and APTMS-coated silica surfaces. For the bare surface (*i.e.*, 0% coverage), the simulated values were mostly consistent with the experimental results (Figure 3c); that is, ζ was relatively constant at low pH and declined roughly linearly above pH 4.87. Above pH 9.5, however, the simulation deviated significantly from experimental behavior; while previous experiments show a negative plateau around pH 8.5 and above, [53]

the model predicted zeta potential to continue to decrease with increasing pH. The experimental plateau in ζ at high pH (and thus, high surface charge density) may result from increased adsorption of Na^+ ions to the surface,[106] excessive dielectric saturation of solvent molecules in the compact Stern layer,[107] or dissolution of silica in extreme alkaline conditions.[108] After testing our model against zeta potential values measured for APTMS-treated capillaries at the start of dissociation in varying pH conditions (Figure 3c), we found our simulation at 51.4% amine coverage agreed well with the experimental response. Overall, the strong concordance between our model and experimental zeta potential behavior for bare and APS-coated surfaces in acidic to neutral-pH affirms its utility for estimating amine density in these conditions.

4.2. Converted APS Coating and Dissociation Kinetics

By coupling this theoretical model with our AZA platform, we were able to estimate coverage kinetics at high-resolution during APS coating formation and degradation reactions. Using our 1:1 coverage model at pH 8.3, we converted ζ response during APS coating formations (Figure 4a) to predicted amine coverage (% NH_2), shown in Figure S7a; this is of particular importance because it allows us to use an indirect surface measurement (*i.e.*, zeta potential) to estimate the true number of amines at the surface. In Figure S7a, we observed faster coating kinetics than the zeta potential measurements from Figure 3a would suggest, followed by a sharp reduction in the coverage rate at around 0.5 h for APTMS and 2 to 2.5 h for APTES. For APMMS, the sluggish coating kinetics were consistent with the results shown in Figure 4a. The slope of these curves suggests that the rate of hydrolysis and surface attachment is fastest for APTMS, while that of APTES is over 4-fold slower; this result agrees with the expected difference in hydrolysis rates shown for methoxy *versus* ethoxy

silanes [77]. These coverage curves also demonstrate that trifunctional silanes can reach over three times the coverage density as monofunctional silanes in a similar 6 h deposition timescale.

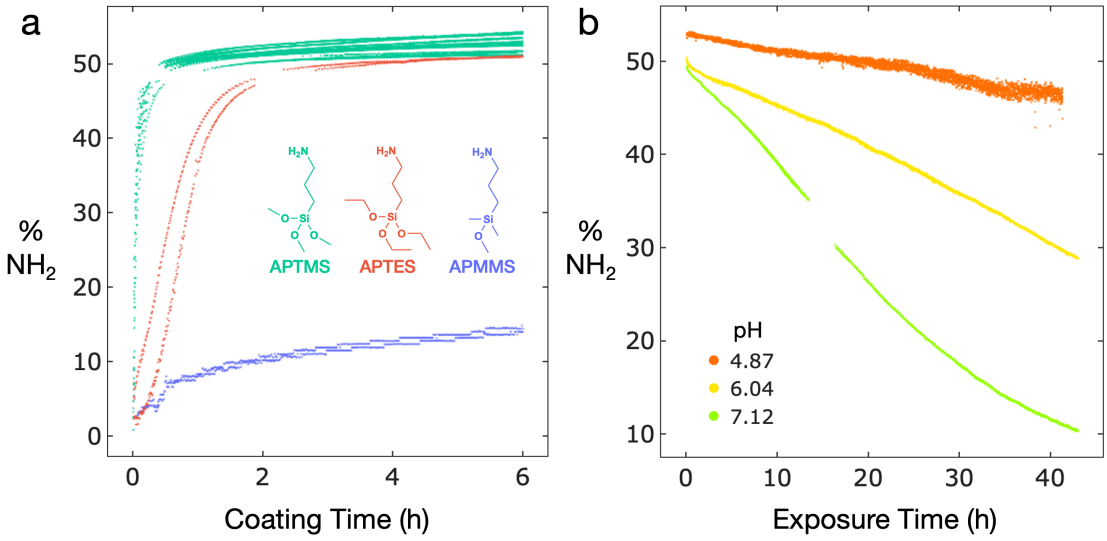

Figure S7. (a) Converted amine coverage (% NH_2) of 6 h coating formations after adding 1 mM respective APS monomers to 0.9X/1X TBS, pH 8.3 reservoirs. (b) Converted amine coverage after exposure of 6h-APTMS-coated capillaries to silane-free solutions of varying pH.

In Figure S7b, we examined the effect of pH on the dissociation kinetics of APTMS coatings. In contrast to the exponential-like zeta potential decay behavior in Figure 3b, the converted amine coverage plot shows more linear decay kinetics at rates which increase monotonically with pH. For the exposure at pH 7.12, the dissociation rate gradually declined when the amine coverage was below 20%, indicating the reaction may be nearing completion. The time to decay to 30% coverage increased from 16.6 h to 40.6 h for pH 7.12

and pH 6.04 dissociations, respectively, indicating a roughly 2.5-fold increase in aqueous stability for a decrease in exposure pH by one unit.

While the stabilities of APTMS, APTES, and APMMS coatings were previously discussed using normalized zeta potential kinetics (Figure 5), conversion to amine density provides a more direct measure of their dissociation kinetics. When translated from zeta potential to percent coverage, the difference in initial coating densities between trifunctional APTMS and monofunctional APMMS was roughly 25%, which we attribute to the previously mentioned differences in siloxy structure and their ensuing rates of surface condensation. Further, by analyzing the time for amine coverage to drop below 30%, we observed that the coating stability of both APTMS and APTES coatings were roughly 2.5-fold that of monofunctional APMMS, which supports our hypothesis that the formation of lateral crosslinking bonds may increase aqueous stability. We also briefly examined another aminosilane monomer, 11-aminoundecyltriethoxysilane (AUTES), which has a higher resistance to hydrolysis than APS [23,35]. While the amine density of AUTES was initially similar to that of APTES and APTMS (Figure S6), it was significantly higher after 30 h of TBS exposure (~45% vs. ~10%). Extrapolating, we estimate that AUTES would reach 30% density after 140.8 h, which is 25.6-fold longer than APTMS and APTES. This result suggests that longer alkyl-chain silanes may be good candidates for coatings used in extended timescale applications.

Our model for amine coverage provides useful insight into studying the reaction mechanisms governing aminosilane coating formation and degradation kinetics. However, a few underlying assumptions in the model limit its use for studying more complex aminosilane coating structures in which the crosslinking density or pK_a are more difficult to

predict. Moreover, since the silanol consumption ratio can vary from 1:1 to 3:1 for trifunctional silanes (Figure S5), these conversions may only be truly valid for monofunctional silanes (*i.e.*, APMMS), which are restricted to a 1:1 surface attachment mechanism and can subsequently form only monolayers at the surface.

5. Converted APS Coating and Dissociation Kinetics

By monitoring the evolution of zeta potential during coating degradation for a variety of monomer types, we identified conditions for improving stability of aminosilane coatings in pH 8.3 tris-buffered saline (TBS). We found that alkyl chain length and crosslinking agents had a positive effect on coating stability in pH 8.3 TBS (Figure S8a). Longer alkyl-chain monomer types (AUTES vs. APTES) experienced slower zeta potential decay rates in TBS, as normalized zeta potential after 60 h of exposure (ζ_{norm}) was 5.7-fold higher (Figure S8b). The addition of an amine-crosslinking agent, BDDE, during deposition of AEAPTMS also significantly improved stability, as ζ_{norm} was 3.4-times higher.

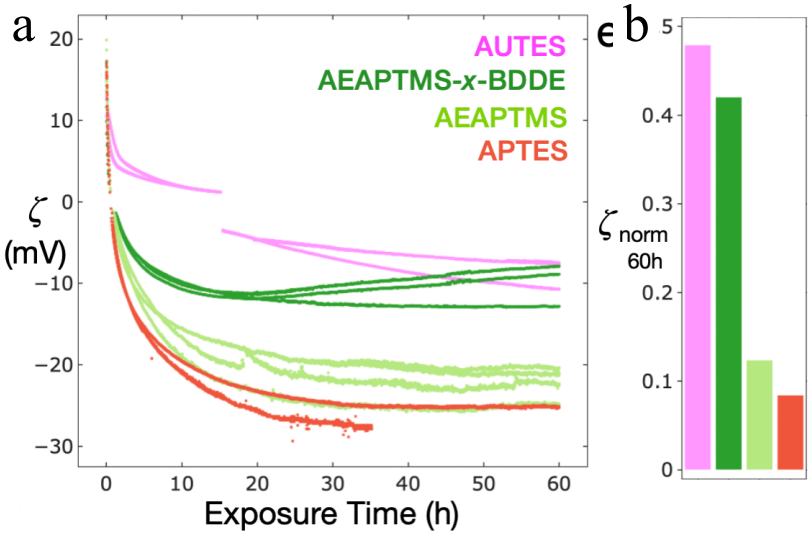

Figure S8. (a) Zeta potential response after coating exposure to pH 8.3 TBS solution at 30 kV/m. Coatings were formed by adding 1 mM silane and 1 mM BDDE crosslinker (see legend) to AMS reservoirs for 6 h at 120 kV/m. (b) Normalized zeta potential (ζ_{norm}) after 60 h of exposure by dividing $\Delta\zeta$ (bare vs. 60h-exposed surface in TBS) by $\Delta\zeta$ (bare vs. 6h-coated surface in TBS).

6. Effects of Buffer Type and Joule Heating during Experiments

The array of buffers used may have different charge-screening and/or adsorption properties, and therefore, the zeta potential response of various buffer solutions (Figure 2c) cannot be attributed to pH only. To minimize these effects, we maintained buffer concentrations below 20 mM, which is less than 12% the total ionic strength. To further study the effect of buffer type on measured zeta potential response, we have performed additional zeta potential titration experiments, with several buffers used in the same pH range (Figure S9). Here, we observed little differences in measured zeta potential as the buffer type was changed between acetate, phosphate, and borate. The continuous zeta potential response observed across the different buffers supports that pH is the *dominant* influence on zeta potential in these experiments.

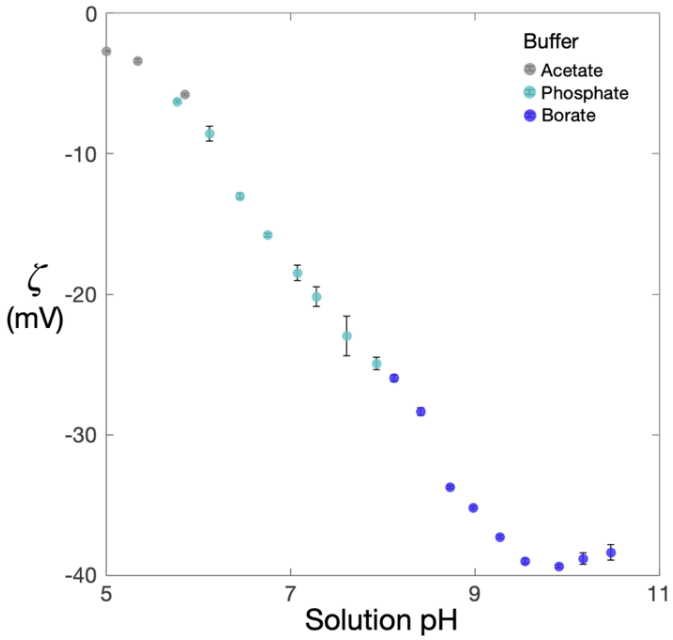

Figure S9. Equilibrium zeta potential vs. solution pH. Each solution consisted of 150 mM NaCl and 10 mM buffer (shown in legend). Each mean zeta potential was calculated using at least 3 measurements after 9 min of flow. Error bars represent 95% confidence intervals of the mean. Other parameters include an electric field strength of 20.9 kV/m; capillary i.d. of 1.1 µm; capillary length of 23.9 mm, and measured solution conductivities between 1.55 and 1.75 S/m.

Another possible confounding effect for our zeta potential measurements is a change in buffer temperature resulting from the silanization reaction or Joule heating caused by the electric current. For example, a temperature increase leads to a decrease in viscosity, which impacts the zeta potential calculation through equation 1. Additionally, a decreasing viscosity leads to an increasing electric current, which could confound detection of the expected current plateau after each buffer traversal. To address this concern, we performed additional analysis and developed a finite element heat transfer model of our system (Figure S10) that indicate that the temperature rise under our conditions is < 0.1 °C, and therefore negligible.

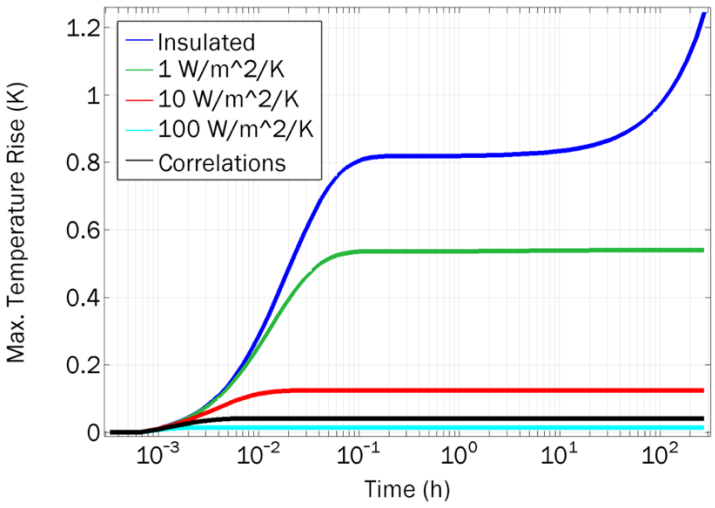

Figure S10. Maximum temperature observed within the capillary during simulated current monitoring experiments, as a function of the free-convection boundary condition applied to the capillary exterior. The blue curve describes a nearly insulated system, where the temperature increases by less than 1 K over 100 h. The black curve mimics real-world conditions by applying natural convection correlations for the capillary exterior and reservoir boundaries. Conditions used in the simulation: glass capillary inner diameter of 1.2 µm, outer diameter of 365 µm, length of 25 mm, solution conductivity of 1.47 S/m, electric field strength of 30 kV/m.

7. Change in Reservoir Concentration at Capillary Outlet during Experiments

The alternating flow mechanism of AZA likely induces a change in reservoir concentration near the capillary inlet/outlet. We studied this effect in greater detail to show the salt concentration in the reservoirs directly adjacent to the microcapillary remains essentially undisturbed. We have prepared three separate analyses: an analytical diffusion-only analysis (in analogy with microelectrodes in electrochemistry), an analytical analysis that includes advection and diffusion, and a detailed numerical analysis with advection, diffusion, and electromigration. For the approximate analysis, we note that the small outlet of

our 1.2 μm capillaries can be roughly thought of as nearly "point-like," with a hemispherical concentration boundary layer for species entering and exiting the capillary (analogous to the flux of species and resulting diffusion layer around a microelectrode). Making the coarse assumption of no fluid flow in the reservoirs themselves (due to mass conservation, the velocity decays rather quickly moving away from the outlet), we can use the equation for a microelectrode (below) to arrive at a diffusion boundary layer thickness estimate (δ) of 2-3 μm for 30 s cycles.

The diffusion layer thickness (δ) surrounding a microelectrode is, from Peter Tomčík, *Sensors* 2013:

$$\delta = \frac{W_\mathrm{e}}{\frac{1}{\sqrt{\pi\Theta}} + 0.97 - 1.10\exp\left(\frac{-9.90}{\ln(12.37\Theta)}\right)}$$

where $\Theta = Dt/W_\mathrm{e}^2$, D is the diffusion coefficient, t is run time, and W_e is the width of the microelectrode or microcapillary. In our system, we assume $D = 1.61 \times 10^{-9}$ m^2/sec, the ambipolar diffusion coefficient of a water–NaCl solution (Harned & Hildreth, 1951). For 30 sec EOF cycles and a capillary diameter of 1.2 μm, we calculate $\delta = 2.60$ μm.

The above estimation is for a purely diffusive boundary layer; however, advection can extend this boundary layer over the length scale of the velocity decay in the reservoirs. This decaying velocity profile can be approximated by equating the mass flux at the capillary outlet of radius R with that through a hemispherical surface a distance r from the outlet to arrive at a "radially" decaying velocity,

$$u_r(r) \approx U_\mathrm{capillary}\,\frac{R^2}{R^2 + 2r^2}.$$

The local advection flux $u_r c$ can then be equated to the local radial diffusion flux, $-D\frac{dc}{dr}$, to yield a separable equation with the following solution,

$$\frac{dc}{dr} = -\frac{U_{\text{capillary}}\, c}{D}\,\frac{R^2}{R^2 + 2r^2}$$

$$c(r) = A \exp\left(-\frac{U_{\text{capillary}}\, R}{D\sqrt{2}} \tan^{-1}\left(\frac{r\sqrt{2}}{R}\right)\right),$$

where A is an integration-constant-related prefactor. We plot the decaying exponential term in this equation for $U_{\text{capillary}} = 700$ µm/s (i.e., 30 kV/m and zeta potential ≅ –33 mV), the shape of which indicates the extent of the transitioning concentration profile (Figure S11); the transition zone between the capillary concentration and the reservoir concentration appears to be largely confined to within approximately 10 µm of the outlet. Moreover, within this ~10 µm hemispherical boundary layer, the volume-averaged concentration was estimated to be only 2.6% different than the reservoir concentration (i.e., by integrating $2\pi \int r^2\, c(r)\, dr$ and dividing by the hemispherical volume).

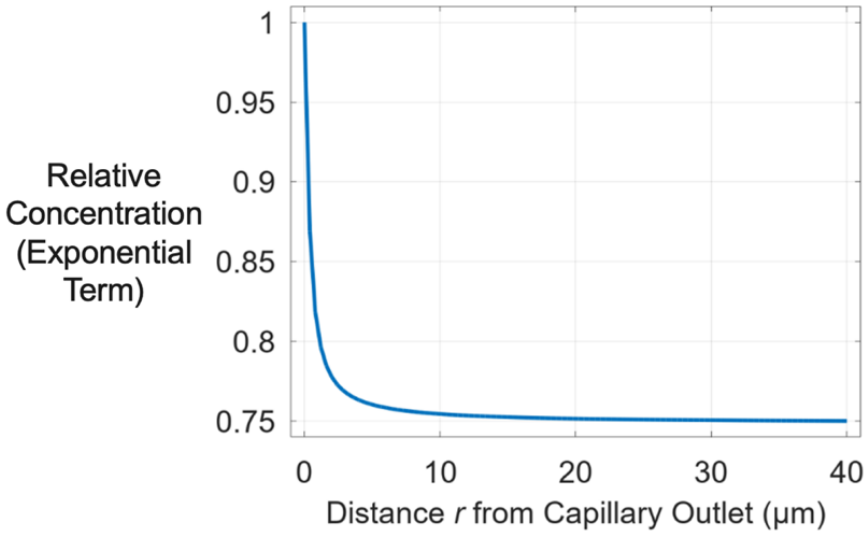

Figure S11. The decaying exponential term from a convection-diffusion-balanced hemispherical concentration boundary layer profile suggests the boundary layer extends ~10 µm.

To validate these analytical estimates, we performed a full 2D axisymmetric multiphysics simulation including advection, diffusion, and electromigration (Figure S12) and confirmed that 1) the concentration remains undisturbed beyond 10-20 µm away from the capillary outlet, and 2) the solution in this ~10 µm region is continuously refreshed due to a) the small amount of this "intermediate" solution relative to the total amount entering the capillary over the course of a subsequent traversal and b) the high Peclet number for axial transport through the channel ($Pe_L \geq 100$ for $|\zeta| \geq 1$ mV). We also provide experimental evidence that the effect of these boundary layers on our measurements is minimal, as we observe sharp plateaus in the current–time response (Figure 2a) at the end of each traversal.

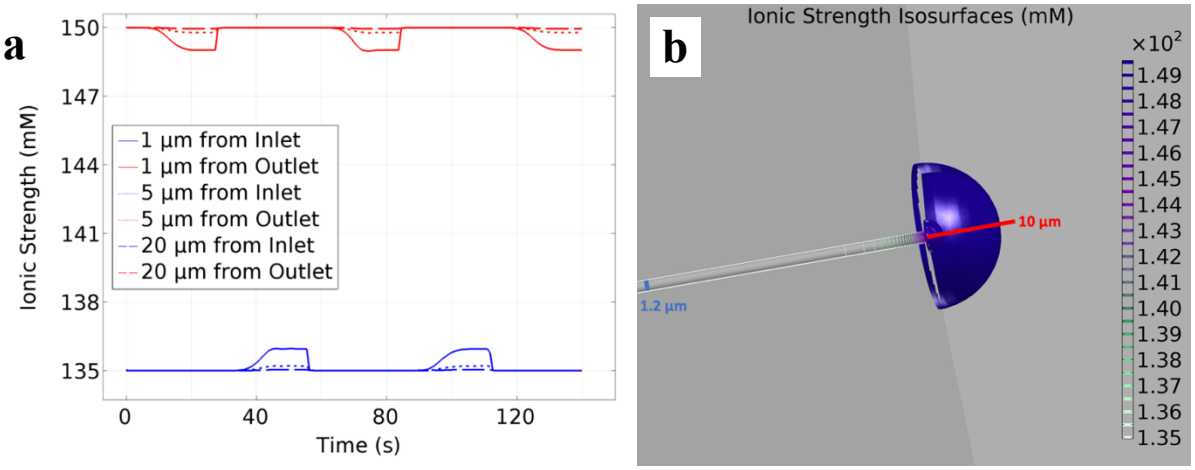

Figure S12. (a) Ionic strength (I.S.) at various distances from the capillary inlet (adjacent to 0.9X reservoir) or outlet (adjacent to 1X reservoir) simulated with COMSOL®. Parameters: 1X I.S.: 150 mM, pH: 7.4, E_0: ±30 kV/m at 28 s cycles, capillary dimensions (length × i.d.): 8 mm × 1.2 µm. Zeta potential distribution was calculated using the local surface chemistry and a "triple layer" model for charge screening.[67] (b) Simulated I.S. distribution near the capillary outlet after 135 mM solution displaces 150 mM solution from the capillary for 28 s.

8. Effect of Back Pressure Induced at Solution Conductivity Interface

There will be an induced back pressure at the interface of the displacing solution due to the difference in zeta potential and conductivity between our two solutions. To quantitatively estimate the effect of the 10% concentration difference on our measurements, we employ the same analysis as that presented by Tang *et al.*[63] Treating the two distinct solution zones as resistors in series, we apply mass conservation and Ohm's law to express the current as a function of the electric fields, conductivities, and interface position. Using the hydrodynamic equations (Hagen-Poiseuille and Helmholtz-Smoluchowski), assuming zero pressure difference across the capillary and no diffusion or dispersion, we determine the induced pressures in terms of the conductivity ratio and zeta potential ratio of the two solutions, as well as the interface position. From the resulting flow distributions, we then determine the area-averaged velocity as the interface moves through the capillary (Equation 16 in Tang *et al.* 2011, reproduced below),

$$\frac{dX}{dt} = \frac{1 + \left(\frac{\zeta_1}{\zeta_2} * \frac{\sigma_2}{\sigma_1} - 1\right) X}{1 + \left(\frac{\sigma_2}{\sigma_1} - 1\right) X} \qquad \text{(eq 16, fully substituted form)},$$

where $X = \frac{x}{L}$ is the non-dimensional length displaced by Solution 1, ζ_1/ζ_2 is the zeta potential ratio and σ_2/σ_1 is the conductivity ratio of the respective solution regions in the channel.[63]

To estimate the zeta potential ratio for our conditions, we use the surface chemistry and triple layer model of Scales and Healy[67] to obtain theoretical titration curves of zeta potential vs. pH for 150 mM NaCl and 135 mM NaCl (Figure S13). These curves indicate around a 5% expected difference in zeta potentials between the 0.9X and 1X solutions.

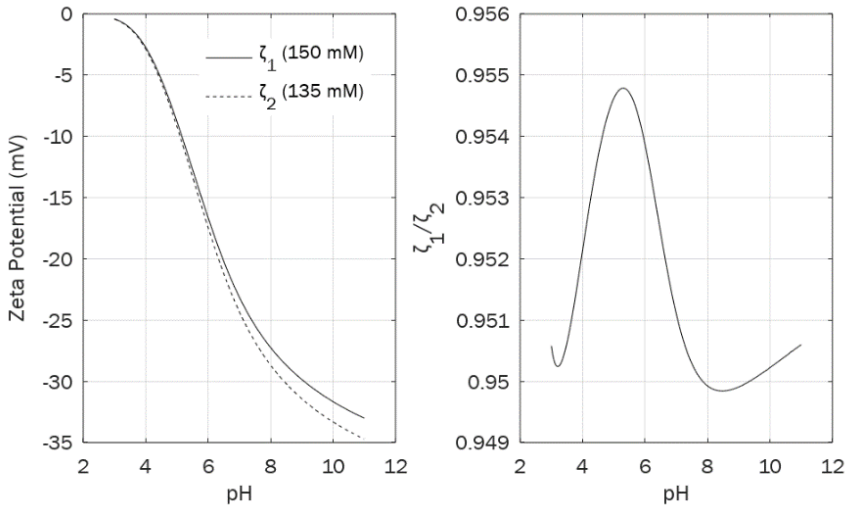

Figure S13. Theoretical zeta potentials vs. pH for 150 mM and 135 mM NaCl on our silica microcapillaries using the theory of Scales and Healy.[67] The difference in zeta potential between the two solutions is estimated to be approximately 5%.

To calculate the traversal time for a range of possible conductivity and zeta potential ratios in our conditions, we numerically integrated the inverse of the above interface velocity (eq 16) over the length of the capillary. We also calculated the theoretical traversal time for conductivity and zeta potential ratios of one (i.e., Helmholtz-Smoluchoswki velocity equivalent) to estimate the percent error of our current monitoring calculations (Figure S14). Although pressure backflow is induced by nonuniformities in both the electric field and zeta potentials, the error introduced in displacement time calculations is entirely due to the zeta potential differences (i.e., not due to the conductivity or electric field differences). That is, if $\zeta_1 = \zeta_2$, then eq 16 shows that there is no error introduced (i.e., a constant interface velocity), regardless of the value of σ_1/σ_2. In our conditions, with a 10% difference in concentration and zeta potentials differing by approximately 5%, our assumption of using the

Smoluchowski equation to calculate zeta potentials from traversal time is predicted to introduce a minimal ≈2.5% error (see data tip in Figure S14).

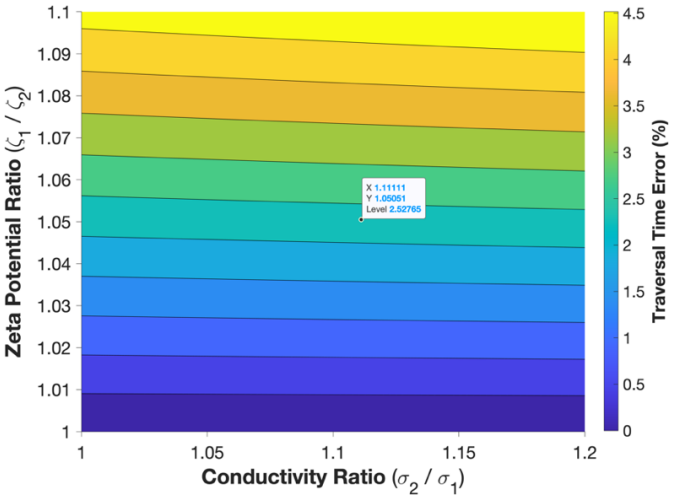

Figure S14. Percent error of the traversal time (calculated by integrating the inverse of Eq 16 from Tang et al.[63] over the capillary length) for varying conductivity and zeta potential ratios, relative to that of a channel with uniform conductivity and zeta potential which follows the Helmholtz-Smoluchowski equation.

Appendix B. Supporting Information for "Electrokinetic Transport of Cationic Surfactant Induces Stagnant Regimes in Capillary Adsorption and Desorption"

1. Capillary–Reservoir Assembly.

The outer reservoir dimensions were rectangular (H: 12 mm, S: 25.4 mm) with elliptical inner cavities designed to hold up to 2 mL of fluid (H: 10.5 mm, R1 = 7.5 mm, R2 = 10.5 mm, bottom fillet = 4 mm, x-SA = 247.4 mm^2, V = 2422.3 mm^3). The reservoir inlet holes (L: 2 mm, R: 0.18 mm) were centered on the faces adjacent to the small reservoir edge (R1 axis). The O-ring groove (H: 0.5 mm, R: 1.25 mm) was located at the inlet to the right reservoir and was designed to hold a custom PDMS O-ring (0.8 mm x 2 mm diameter). The PDMS O-ring was punched from a 0.8-mm sheet of PDMS using a 2-mm diameter hole punch from Pelco. After placing the PDMS cylinder into the groove located at the right reservoir inlet, a sacrificial capillary was used to create a passage through the center of the PDMS cylinder. This capillary was replaced with a new capillary for experiments. To compress and seal the O-ring, four screws with nuts were passed through holes connecting the two reservoirs and were tightened with an appropriate torque to not break the capillary. The four screw holes (D: 3.1mm) are equally spaced 8.8 mm from the inlet hole.

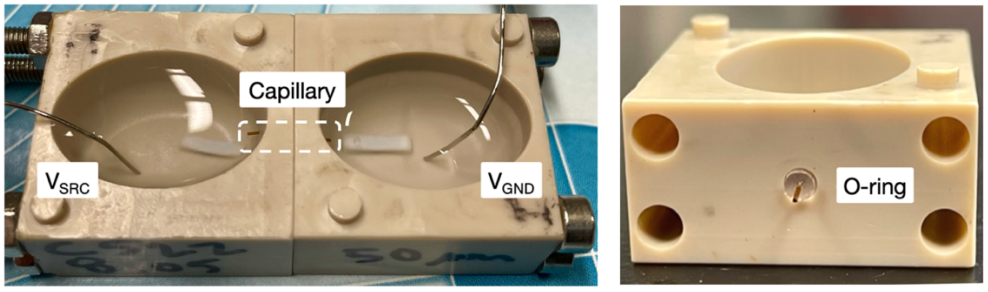

Figure S1. Image of capillary–reservoir device. The 8-mm capillary bridges two PEEK reservoirs containing buffer solution (1.5 mL), stir bars, and electrodes to drive EOF and monitor current. The internal O-ring is made by piercing the capillary through a PDMS cylinder, which is then aligned and compressed into the groove on the right reservoir inlet.

2. Determining the Time of Zero-Charge

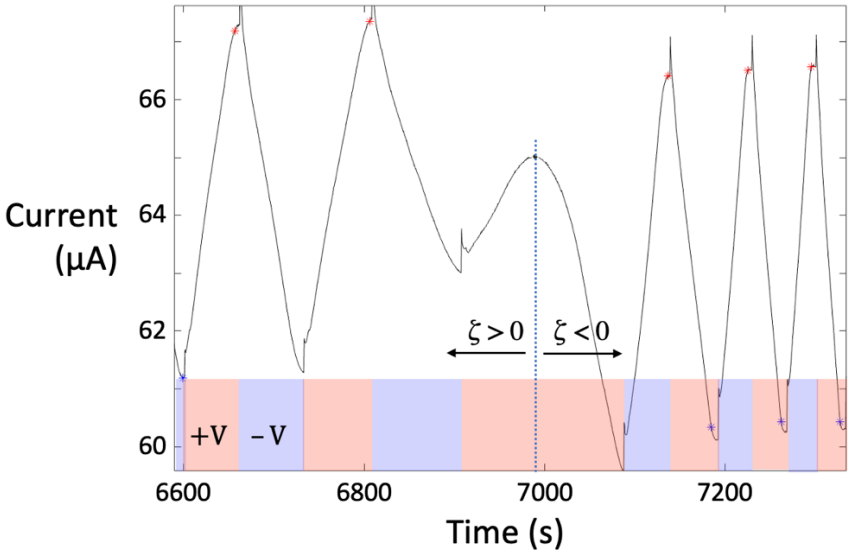

Figure S2. Extracted current and traversal endpoints during CTAB desorption using AZA. The dashed line shows the approximate time (±10 s) when zeta potential changes signs.

3. Equilibrium Mobility & Zeta Potential in CTAB–PBS Solutions

3.1. EP Mobility Measurements

Electrophoretic mobilities were determined using NG-ELS (Next Generation Electrophoretic Light Scattering, Enlighten Scientific LLC, Hillsborough, NC).[109] NG-ELS has been demonstrated to measure electrophoretic mobilities of particles in aqueous media up to 6 molar ionic strength.[110] It incorporates numerous improvements over the current generation of commercial instruments, such as the Malvern Zetasizer Nano ZS, that fail to reliably measure electrophoretic mobilities of aqueous systems at physiological ionic strengths or higher. The functional design and operation of the instrument are based upon the original phase analysis light scattering (PALS) apparatus[111] that employed a crossed-beam optical configuration in contrast to the more common reference beam configuration used in commercial ELS instruments. The electrode assembly used for the NG-ELS equipment was a variation of that described by Uzgiris.[10] Disposable polystyrene semi-micro cuvettes (4 mm path length) were used as the sample holders. Two identical parallel plate platinized platinum[112] electrodes, 4 mm apart, were used to provide the driving voltage across the sample. The volume of the sample required for measurement was approximately 0.25 mL. Samples were measured without further dilution. The sample temperature was measured with a miniature NTC-type thermistor that was placed in direct contact with the sample. It was positioned at the mid-point between the electrodes and approximately 1 mm above the intersection point of the two laser beams. Temperature control was achieved by placing the sample cuvette in an aluminum block that acted as a heat transfer device between it and cooled water circulated through channels within the block. The required temperature of the water was dependent on the amount of Joule heating of the sample and, therefore, the

conductivity of the sample and the magnitude of the voltage applied across the electrodes. Complex impedance analysis of the electrode waveform was used to quantify electrode polarization and Joule heating. Mobility measurements were made at 20.0 ± 0.4 °C using sinusoidal electrode signal waveforms with a nominal amplitude of 4.0 to 8.0 V at frequencies of 64 and 128 Hz. The scattered light data were used to calculate two electrophoretic mobilities via PALS and laser Doppler electrophoresis (LDE) analysis methods.[110] For each sample, 3 independent measurements were made for 150 seconds at each electrode signal frequency, yielding a total of six measurements per sample from which a mean mobility value was calculated.

3.2. Equilibrium Zeta Potential Measurements.

A volume of CTAB was added from a solution of around a 100-fold higher concentration of CTAB (same BGE) than that of the reservoir after addition. To equilibrate the capillary with a given CTAB solution, a 1 mL pipette was used to flush the capillary twenty times verified using current monitoring. Then, AZA–DC (2min–3min) was applied (±30 kV/m, 15 min) with a ~4 mm head difference (1 mL) between reservoirs. Finally, equal volumes of 0.9X/1X [CTAB]-PBS were placed in the reservoirs and AZA–DC (2min–3min) was applied until a stable zeta potential value was measured for at least 15 min.

3.3. Extracted cmc and csac values of CTAB in 0.1X and 1X PBS

The critical micelle concentration (cmc) of CTAB was reported to be approximately 0.9 mM in DI water and 0.15 mM in 50 mM ionic strength solution.[97] The critical surface aggregation concentration (csac), or the onset of aggregation observed by AFM, was reported by Liu and Ducker to occur at around one-third to one-half the cmc.[81] In Figure S3a, we show that the EP mobility of CTAB roughly increases with concentration from

approximately 30-150 µM in 0.1X PBS and 1X PBS, then above 150 µM the slope changed signs. Similar analysis of the inflection point in mobility vs. concentration was used by Cieśla to extract the cmc;[91] by this method, the cmc was around 0.15 mM in both PBS conditions. In Figure 3b, we show the average equilibrium wall zeta potential of a capillary exposed to different concentrations of CTAB in 0.1X PBS and 1X PBS until stable using AZA–DC. The equilibrium zeta potential increased significantly with concentration from around 10-100 µM, then approached a steady state above 100 µM. The saturation in zeta potential indicates the csac is around 100 µM in these conditions.

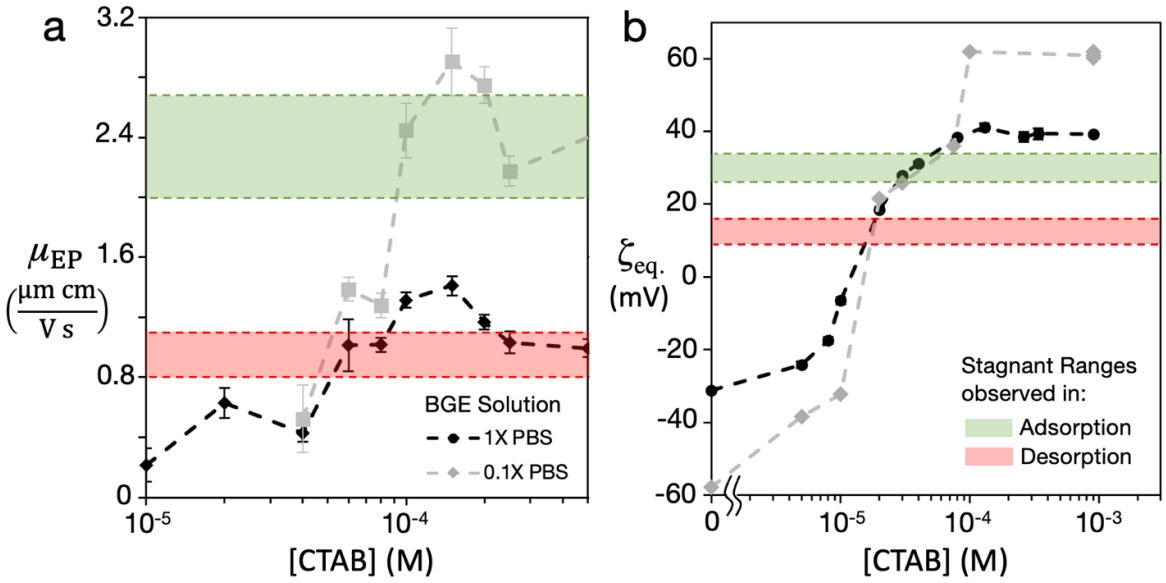

Figure S3. The effect of CTAB and/or PBS concentration on a) the average EP mobility measured using an Enlighten Scientific NG-ELS instrument or b) the average zeta potential of a 39.5 µm capillary measured using AZA–DC.

4. Comparison of CTAB Desorption Kinetics

In an EOF-based study, Wang and Lucy measured a linear decay in EOF velocity from reversed to normal direction (*i.e.,* positive to negative zeta potential), as the EOF velocity approached the bare capillary value in 70 min.[26] The stagnant regime may have been obscured due to a slight pressure difference in their conditions, which would cause a higher transport of CTA^+ than in pure EOF/EP conditions. In a similar study, using a 37% higher electric field strength and a 37% shorter capillary, Melanson et al. observed a two-fold higher initial EOF magnitude and a more stable reversed EOF, which may be due to the stagnant regime (i.e., the EP mobility) in their conditions.[13] In a study employing a much higher flow rate using pressure, Theodoly et al. show a rapid decay in zeta potential to approach the bare glass value in approximately 13 min.[27] In a capillary (39.5 μm x 8 mm) coated with 0.26 mM CTAB and exposed to 0.1X PBS (15 mM NaCl, 1.33 mM disodium phosphate, 0.67 mM monosodium phosphate, pH 7.3) under AZA–DC, we observed multiphasic decay behavior that approached the final equilibrium in around 20 min. Our solution conditions were comparable to the Lucy studies, however, we applied a 1.9-fold lower electric field strength (±30 kV/m) that alternated polarity according to AZA–DC (2 min–3 min), and we used a 34-fold shorter capillary length (8 mm).

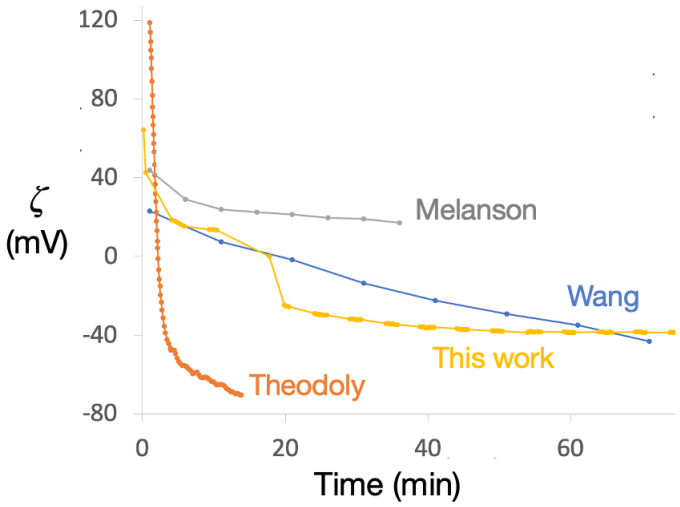

Figure S4. Compared zeta potential kinetics (from EOF mobility or streaming potential) of CTAB desorption from microchannel surfaces in an applied pressure or electric field.

Table S1. Comparison of CTAB desorption: transport and solution properties (Figure S4).

Authors	Pressure or Electric Field	Max Fluid Velocity (cm/s)	Diameter / X-Section (mm)	Length (cm)	Solution
Theodoly[27]	40 kPa (PDF)	98	0.125 x 15	0.06	1 mM KCl pH 5.5
Melanson[13]	–55.6 kV/m (EOF/EP)	0.00133	0.05	27	10 mM phosphate pH 7.2
Wang[26]	–40.5 kV/m (EOF/EP)	0.00137	0.05	37	20 mM phosphate pH 7
This work	±30 kV/m (2m-3m AZA–DC)	0.00151	0.0395	0.008	2 mM phosphate 15 mM NaCl pH 7.3

5. Extracted Net CTA^+ Transport Kinetics and Fitted EP Mobilities

Table S2. Zeta potential range of stagnant regime and bare/coated capillary (Figures 2-3).

Diameter (μm)	Length (mm)	Bare: Average ζ ±2×SEM (mV)	Ads: Stagnant ζ Range (mV)	Coated: Average ζ ±2×SEM (mV)	Des: Stagnant ζ Range (mV)
39.5	8	-29.1 (±1.3)	+25–xx[1]	39.7 (±1.1)	+13–16
39.5	16	-24.6 (±2.0)	+30–32	37.8 (±4.3)	+12–16
39.5	24	-28.3 (±8.6)	+29–32	40.7 (±2.2)	+13–16
9.8	8	-31.3 (±5.1)	+29–31[1]	38.4 (±3.4)	+13–16
4.6	8	-30.6 (±1.8)	+28–34	37.6 (±2.6)	+11–16
1.2	8	-22.7 (±2.5)	+28–34	34.3 (±8.2)	+11–16

[1]Break-out point of stagnant range was not observed.

5.1. Conversion of Zeta–Time Responses to Net CTA^+ Transport

The net CTA^+ transport volume over surface area was calculated using the sum of the time-integrated EOF transport (trapezoidal rule applied to zeta potential–time) and EP transport (fitted EP mobility values in Table S3) per voltage cycle in the following equation,

$$\text{Net CTA}^+ \text{ Volume/SA} = \frac{r}{2L}\sum_{i=2}^{n}\left(\left|\frac{\epsilon E}{2\eta}\left(\zeta_i + \zeta_{i-1}\right) + \mu_{\text{EP}}E\right|\right) \times (t_i - t_{i-1}),$$

where E is the electric field, ϵ is the permittivity, μ is the viscosity, μ_{EP} is the EP mobility, and L is the capillary length. The EP mobility was determined by linearizing the stagnant regime (Table S3) in the zeta potential vs. net CTA^+ volume/SA curves (Figure S5).

5.2. Discussion of Net Transport Plots

We converted the zeta potential–time responses to zeta potential vs. net CTA^+ transport volume divided by capillary surface area to elucidate the effects of the EP mobility and confinement in small channels. The net CTA^+ transport-volume-over-surface-area plots were obtained by multiplying the net CTA^+ velocity (EOF + EP) by the capillary cross-sectional

area to obtain a volumetric flow rate, and then integrating over time and dividing by the capillary surface area. The stagnant regime is effectively eliminated through this integral transformation to a transport axis, as there is a minimal contribution to the overall transport during this period. The EP mobility was determined iteratively for each experiment by applying a line of best-fit to the observed zeta potential ranges of the stagnant regimes. The final net volume curves were largely linearized and collapsed, with similar normalized kinetics for the different diameters; this collapse and the qualitative agreement between simulation and experiment confirm that the adsorption–desorption kinetics in CE conditions are strongly influenced by the EP mobility of the adsorbing surfactant and the surface-area-to-volume ratio of the channel.

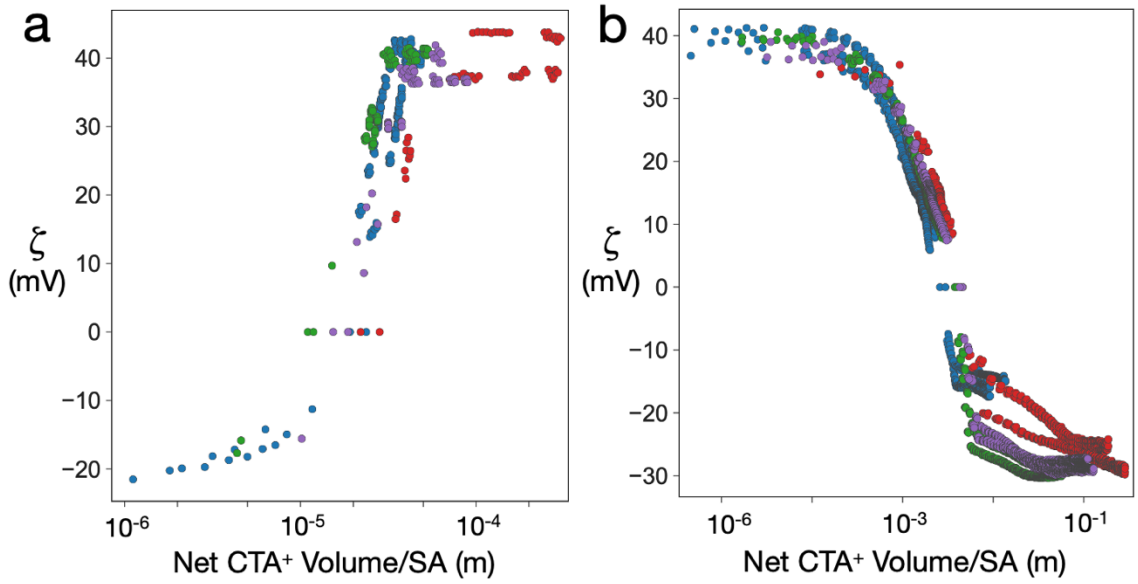

Figure S5. Transformed data from Figure 3 with the x-axis converted to net CTA^+ transport volume normalized by surface area.

Table S3. Fitted EP mobilities obtained by linearizing the stagnant range (Figure S5).

Diam (μm)	Capillary	Ads: Fitted μ_{EP} (10^{-8} m^2/Vs) & Equivalent ζ (mV)	Ads: R^2	Des: Fitted μ_{EP} ($\times 10^{-8}$ m^2/Vs)	Des: R^2
1.2	C405_1	2.50	0.982	0.98	0.970
	C405_2	2.44	0.980	0.97	0.966
4.6	C449	2.37	0.990	1.12	0.964
	C451	2.29	0.998	1.09	0.961
9.8	C446_2	2.38	0.997	1.11	0.962
	C454	2.34	0.996	1.13	0.965
39.5	C500_3	2.08	0.999	1.13	0.978
	C519	2.06	0.994	1.11	0.944

6. Simulated CTAB Dynamics for Varying Types of Transport

The adsorption and desorption of CTAB to a microcapillary surface was simulated using COMSOL Multiphysics v6.0. We use the Nernst-Planck equation (with electroneutrality enforced) to model the electromigration, diffusion, and advection of the background electrolyte species and reactive CTA^+ species, which are treated as ions. For simplicity, we model the 0.9X/1X PBS reservoirs as Na^+ and Cl^- ions at 150 mM and 135 mM ionic strength respectively; the relatively dilute bromide anions in 0.26 mM CTAB are assumed negligible. The fluid flow is solved using the transient Stokes and mass conservation equations, with an electroosmotic slip condition $u_z = -\frac{\varepsilon E_z \zeta}{\eta}$ enforced at the capillary walls.

The electric potential distribution and resulting electric field are determined by coupling current conservation (i.e., a divergence-free current density) to the Nernst-Planck equations, which dictate the local conductivity. A potential difference of $V = E_{\mathrm{nominal}} L_{\mathrm{capillary}}$ is imposed between the electrodes at the far reservoir boundaries across from the capillary inlet, along with a normal-stress-free condition for the fluid flow. For AC simulations, the polarity of the applied potential difference is varied periodically using a square wave. The adsorption simulations use a CTA^+ diffusion coefficient of 0.565×10^{-9} m^2/s corresponding to an EP mobility equivalent to $\zeta = +31.58$ mV, which is where we most prominently observe the adsorption stagnant regime; the desorption simulations use a diffusion coefficient of 0.283×10^{-9} m^2/s corresponding to a mobility equivalent of $\zeta = +15.79$ mV. For simulations mimicking a head-induced pressure-driven flow between the reservoirs, a velocity equating to either a 5- or 30-mV zeta potential (approximately 106 and 636 μm/s) is imposed, calculated from the Hagen-Poiseuille equation.

CTAB adsorption and desorption processes are modeled through a first-order reaction, with a reaction rate $R = k_{\mathrm{ads}} c_{\mathrm{CTA,DL}} - k_{\mathrm{des}} c_{\mathrm{CTA,s}}$. In this equation, $c_{\mathrm{CTA,DL}}$ is the local volumetric concentration of CTA^+ in the diffuse layer, determined by multiplication of the local bulk concentration by the Boltzmann factor, $\exp\left(-\frac{F\zeta}{RT}\right)$; $c_{\mathrm{CTA,s}}$ is the surface concentration of CTA^+ bound to the reacting surface, determined from the equation $\frac{\mathrm{d}c_{\mathrm{CTA,s}}}{\mathrm{d}t} = R$, with an opposite flux boundary condition $(-R)$ imposed for the bulk CTA^+ at the surface. Values of $k_{\mathrm{ads}} = 4.4 \times 10^{-7}$ m/s and $k_{\mathrm{des}} = 4.02 \times 10^{-3}$ s^{-1} were chosen, as these generally gave similar overall time scales to our experiments. The zeta potential, which couples the surface reactions to the electrokinetic transport, is determined by the local surface concentration, $c_{\mathrm{CTA,s}}$. As we lack surface-concentration-vs.-zeta isotherm data for our

specific conditions and only aim to obtain qualitative results, we simply model this relationship as linear (i.e., at a surface concentration of 0, the zeta potential is specified as the -30 mV bare silica value we measured experimentally, and the zeta potential grows linearly with $c_{\mathrm{CTA,s}}$ until it reaches the +40 mV value observed for a fully-coated surface, where $c_{\mathrm{CTA,s}} = c_{\mathrm{CTA,s_{max}}}$). We impose a maximum surface concentration (corresponding to chemical equilibrium with our bulk CTAB coating concentration of 0.26 mM) of 2.26 mg/m^2 (estimated from the work of Theodoly *et al.*[27]). Electrostatic attraction and repulsion are accounted for through the aforementioned Boltzmann factor, such that the effective concentration of CTA^+ that participates in the surface reaction is greater than that in the bulk solution when the surface has a negative zeta potential, and the concentration is lower than that in the bulk once the zeta potential passes above 0 mV. The resulting zeta potential values shown in plots are length-averaged - though during the reaction, the local surface concentration and zeta potential distributions are nonuniform to some extent until the reaction reaches completion.

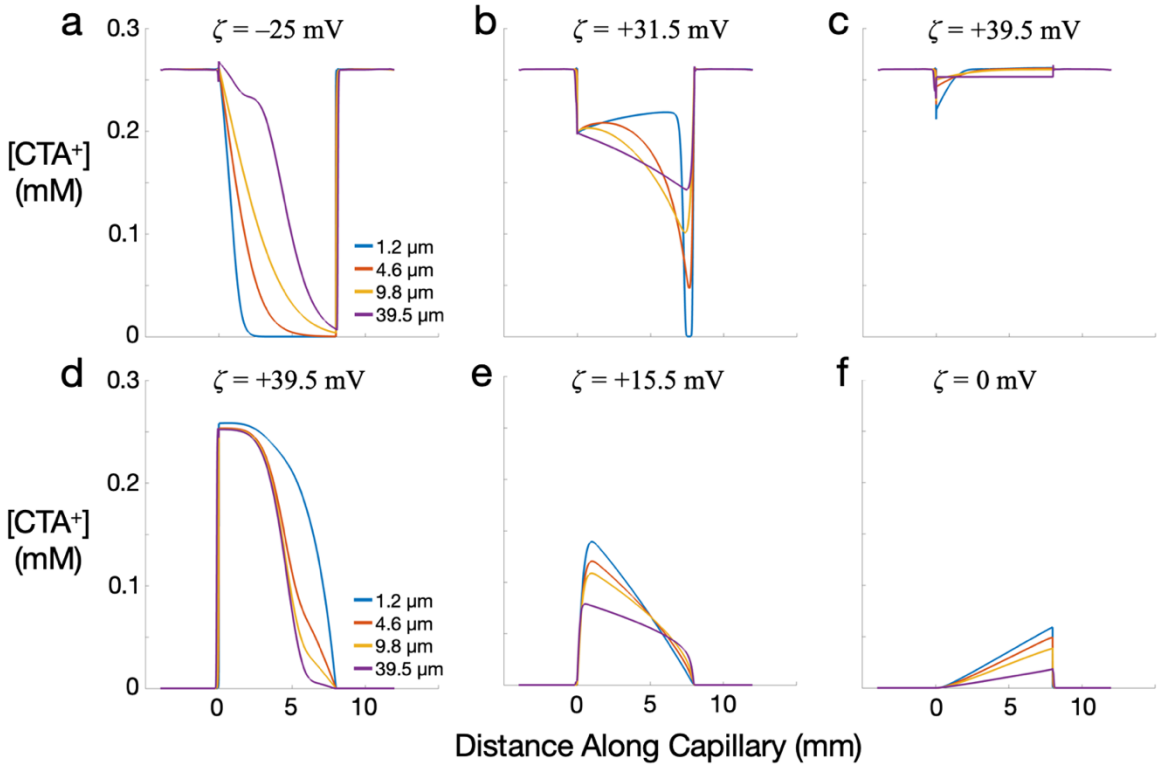

Figure S6. Simulated CTA^+ concentration along the longitudinal centerline of 8-mm capillaries (varying diameter) in a DC electric field during (a-c) 0.26 mM CTAB adsorption and (d-f) desorption in 0.9X/1X PBS. The simulated region from 0-8 mm is inside the capillary, whereas that outside this range is in the reservoirs.

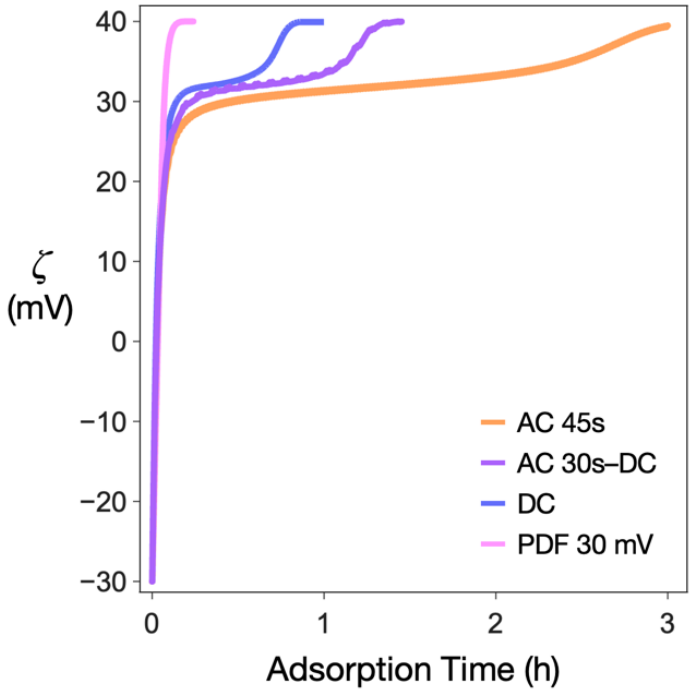

Figure S7. Simulated zeta potential kinetics for different transport processes during adsorption of 0.26 mM CTAB in 0.9X/1X PBS in a 4.6 µm × 8 mm capillary.